People's Democratic Republic of Algeria

Ministry of Higher Education and Scientific Research

Echahid Echeikh Larbi Tebessi University

Faculty of Sciences and Technology

Department of Mechanical Engineering

Doctoral Thesis

Presented for attainment of the LMD Doctoral degree

In: **Mechanical Engineering**

Specially**: Energetic**

By: **BEKKAI Riyadh**

Entitled

Aerodynamic optimization of micro horizontal axis wind turbine via response surface method

Presented and publicly defended, **17/06/2025**, in front of the jury composed of:

BELAZIZIA Abdennacer	**Prof.**	**President**	**U.Tebessa**
MDOUKI Ramzi	**Prof.**	**Supervisor**	**U.Tebessa**
LAOUAR Roudouane	**MCA**	**Co-supervisor**	**U.Tebessa**
BORDJA Lyes	**Prof.**	**Examiner**	**U. Oum elbouagui**
FILALI Abdelkader	**MCA**	**Examiner**	**ENP Constantine**
YOUNES Ramdane	**MCA**	**Examiner**	**U.Tebessa**

2024-2025

Abstract

This study focuses on the redesign and optimization of the three-dimensional geometry of a micro horizontal-axis wind turbine (HAWT) blade using Response Surface Methodology (RSM). The geometric variation of two key design parameters, chord length and twist angle, is mathematically modeled using a fourth-degree and second-degree polynomial, respectively. The optimization framework is based on eight input parameters that define the initial blade configuration.

To evaluate aerodynamic performance and structural integrity, a comprehensive comparative analysis is conducted between the initial and optimized blade designs using Computational Fluid Dynamics (CFD) and Blade Element Momentum (BEM) methods. The CFD simulations utilize the Reynolds-Averaged Navier-Stokes (RANS) equations with the k-ω SST turbulence model to capture complex flow phenomena and predict aerodynamic efficiency. The optimization process is implemented using a Multi-Objective Genetic Algorithm (MOGA) coupled with a non-parametric regression (NPR) metamodel, enabling the automated selection of the most efficient blade design.

Performance assessments of the turbine rotor are carried out using the open-source software QBlade, with results compared against CFD predictions across various Tip Speed Ratio (TSR) values. The optimized blade demonstrates significant improvements, yielding a 15% and 12.53% increase in power coefficient for CFD and QBlade analyses, respectively, at a design TSR of 3. Compared to the baseline blade, the optimized design exhibits superior aerodynamic characteristics, including enhanced lift generation, reduced flow separation, and improved efficiency across all TSR values.

Furthermore, a detailed three-dimensional flow analysis, incorporating pressure distribution and limiting streamlines on both blade surfaces, confirms the optimization objectives. The results highlight a notable reduction in flow separation zones and a subsequent increase in rotor torque. Additionally, structural safety considerations reveal a 37% improvement in starting operability at lower wind speeds, contributing to enhanced overall performance and operational reliability.

Acknowledgments

I would like to express my sincere gratitude to Almighty God, who enlightened my path to success and granted me the strength to accomplish this work.

This thesis is the fruit of dedication, but it would not have been possible without the invaluable support of many individuals. I extend my heartfelt thanks to all who contributed, directly or indirectly, to the completion of this study.

Special thanks are due to my mentor, Professor Mdouki Ramzi, for his scientific and moral guidance, and to my co-supervisor, Dr. Roudouane Laouar, for his continuous support and valuable advice.

I am also sincerely grateful to Dr. Abdelkader Filali for his positive spirit and insightful guidance, and to Professor Bordja Lyes, whose supervision during my Master's studies laid a solid foundation for my research path.

I deeply appreciate all the professors of the Mechanical Engineering Department for their knowledge and encouragement, and I warmly thank Dr. Alaeddine Mekahlia and Professor Younes Ramdane for their unwavering support and kindness.

My gratitude extends to Professor Belazizia Nacer, head of the examination committee, for his constructive feedback, and to the staff of the L'Environnement Laboratory, especially Pr-Loufi Messoud and Dr-Zoubir Aoulmi, for their essential support.

I also acknowledge the external research support from Germany, particularly the KASSEL Laboratory under the leadership of Prof. Dr.-Ing. Olaf Wünsch, whose contributions significantly enriched this work.

Finally, I am deeply thankful to all my friends and companions throughout this journey, especially to Chihabddine Abaidia, a true knowledge enthusiast, whose faithful presence and early support since the very beginning of this research have been invaluable.

Dedication

I wholeheartedly dedicate this thesis:

To the cherished memory of my beloved father, Mouhamed Lakhder, whose guidance and values continue to illuminate my path. Though you are no longer by my side, your spirit lives on within me, inspiring every step I take. May the Almighty, in His infinite mercy, grant you eternal rest in His paradise.

To the cherished memory of my esteemed mother, Zarroug Saïda, whose unwavering strength, boundless affection, and endless sacrifices have been my constant support. Though you have departed this world, your prayers, love, and values remain deeply rooted in my heart, guiding me still. May the Almighty, in His boundless mercy, grant you eternal peace and a place in His highest paradise.

To my dear brothers and sisters, whose examples of perseverance, generosity, and steadfastness have been a continual source of motivation. I remain forever grateful for your presence and encouragement.

To my beloved elder sister, Samra, and my esteemed friend, Mekahlia Alaeddine, who believed in me and supported me when belief itself was a rare gift. Your faith and encouragement have left an indelible mark on my journey.

To all the members of my family, both young and old, who have enriched my life with their love and kindness. May this work serve as a humble expression of my deepest gratitude and affection.

To my dear friends, whose companionship, loyalty, and encouragement have been invaluable throughout the years.

And to all those who, in ways both great and small, have inspired, supported, and accompanied me on this path — I dedicate this achievement to you.

Table of content

Abstract I
Dedication III
Table of content IV
Liste of figures VIII
Liste of tables X
Nomenclature XI
I. general Introduction 1
I.1 introduction 1
I.2 Wind Turbine 2
I.2.1 Horizontal Axis Wind Turbine (HAWT) 3
I.2.2 Vertical Axis Wind Turbine (VAWT) 3
I.3 Micro HAWT 4
I.4 History of Wind Energy 5
I.5 Modern Wind Turbine Design 5
I.5.1 Rotor 7
I.5.2 Drive Train 7
I.5.3 Generator 8
I.5.4 Nacelle 8
I.5.5 Tower and Foundation 8
I.5.6 Electrical and Control Systems 8
I.6 The current problem 9
I.7 Objective of the Study 9
I.8 Thesis organization 10
II. Chapter II: Review of Previous Studies 11
Introduction 12
II.1 Design and Analysis of HAWT Rotors Using CFD and BEM Methods 12
II.2 Classification of Optimization Processes 13
II.2.1 Optimizing Through Iterative Processes 13

II.2.2 Optimizing Individual Input Parameters via Response Surface Methodology (RSM) 15
II.2.3 Combined parameter optimization using the Response Surface Method 15
II.3 Optimal Design Discovery: Comparing Deep Learning and Surrogate Modeling 16
II.4 General remarks 17
II.5 Research Objectives 17
III. Chapter III: Aerodynamics and Advanced Design of Micro HAWTs: Insights from Qblade Analysis 19
Introduction 20
III.1 Mechanism of Wind Power Capture by Blade section 20
III.2 Airfoils and Fundamental Aerodynamic Principles 22
III.2.1 Airfoil Terminology 22
III.2.2 Lift, Drag, and Non-Dimensional Parameters in Wind Turbine Blades Profile 23
III.2.3 Airfoil selection 25
III.3 Aerodynamic theories of Wind Turbines 25
III.3.1 Actuator Disc Model 26
III.3.2 Wake Rotation 31
III.3.3 Blade Element Theory (BET) 32
III.3.4 Blade Element Momentum (BEM) Theory 34
III.4 HAWT Design and Analysis with Qblade 35
III.4.1 Qblade V 0.96 Interface 35
III.4.2 Overview of Qblade Tools 36
III.4.3 360° Extrapolation module 38
III.5 Turbine Definition and Simulation submodule 41
III.6 Advanced BEM Theory in Qblade with Corrections 41
III.6.1 Prandtl tip- and root loss 42
III.6.2 New tip- and root losses after Shen 43
III.6.3 3D correction after Snel 44
III.6.4 Reynolds number drag correction 44

III.6.5 Foil interpolation 44
Conclusion 45
IV. Chapiter IV: Parametric Analysis of Geometry Design for High-Efficiency HAWT 46
Introduction 47
IV.1 Flowchart for the Design and Analysis of micro HAWT Utilizing Qblade Software 47
IV.2 Choosing the best Airfoil profile 48
IV.3 Qblade model validation 51
IV.4 Blades number and tip Speed Ratio effect 53
IV.5 Hub -to-Tip ratio effect 54
IV.6 Reynolds number effect 56
IV.7 Power turbine analysis over operating range 57
IV.8 Blade Geometry using Curve Fitting 59
IV.8.1 Chord Distribution 60
IV.8.2 Twist Angle Distribution 62
IV.8.3 Curves fitting modelling analysis using Qblade: 63
Conclusion 65
V. Chapter V: CFD analysis and optimization of wind turbine rotor . 66
Introduction 67
V.1 Numerical Solver 67
V.2 Shear Stress Transport (SST) $k-\omega$ Model 68
V.3 CFD analysis of initial turbine rotor 69
V.4 Domain Geometry 70
V.5 Computational grid 70
V.6 Boundary Conditions 72
V.7 Y+ distribution and numerical model 72
V.8 Numerical approach validation 73
V.9 Numerical study of optimized turbine rotor 74
V.9.1 Goal-Driven Optimization 75
Conclusion 80

VI. Chapter 6 RUSALT AND DISCUSSIONS 81
Introduction 82
VI.1 Optimizing Response Surfaces using the MOGA algorithm 82
VI.2 Blade Optimization Targets 84
VI.3 Pressure Distribution 86
VI.4 Flow visualization 87
VI.5 Static Torque Comparison 90
VI.6 Influence of the new optimized rotor geometry on blade velocity distribution 91
VI.7 3D Flow Visualization of the Optimized Blade Design ... 93
VI.8 Comparison results between Qblade and CFD 94
VI.8.1 Introduction 94
VI.8.2 Comparison the torque and power between CFD and Qblade 95
VI.8.3 Comparison the thrust force between CFD and Qblade 95
VI.8.4 Torque coefficient compression 96
VI.8.5 Power coefficient compression 97
VI.8.6 Thrust force coefficient compression 99
VI.8.7 Structural Safety Analysis of the Optimized Rotor 100
Conclusion 101
Key Results 102
Recommendations 103

Liste of figures

Figure I-1 World onshore wind map at a height of 80 m [15] 2
Figure I-2: Wind power converts to electrical power [16] 2
Figure I-3: Horizontal axis wind turbine [17] 3
Figure I-4: Vertical axis wind turbine categories [18] 4
Figure I-5: Micro wind turbine installation [19] 4
Figure I-6: Mill wind turbine [21] 5
Figure I-7: Major components of a horizontal axis wind turbine [18] 6
Figure I-8: Detailed view of wind turbine components [18] 7
Figure III-1: Lift coefficient variation VS angle of attack. 21
Figure III-2: Wind turbine blade divided into a series number of sections. 32
Figure III-3: Velocities on blade element [53] 33
Figure III-4: Forces on blade element [53] 33
Figure IV-1: Flowchart for the Design and Analysis of micro HAWT. 47
Figure IV-2: The different shapes of the SG604x airfoils family. 48
Figure IV-3 : The performance of SG 604x family at Reynolds number a) Re=20000, b) Re=40000, c) Re=55000 51
Figure IV-4: 3D views comparison between (a) Experimental rotor, (b) Simulated rotor 51
Figure IV-5: Validation of the numerical approach with experimental data 53
Figure IV-6: Effect of both tip speed ratio and blade number on the micro HAWT performance 54
Figure IV-7: 3D view of HAWT from hub tip ratio 0.08 to 0.2 55
Figure IV-8: Effect Hub tip ratio on the turbine performance. 56
Figure IV-9: Effect Reynolds number on the turbine performance. 56
Figure IV-10: Effect Reynolds number and blade airfoil types on output power at: a) Re=20000, b) Re=40000, c) Re=55000 59
Figure IV-11: distribution of both: a) chord length, b) twist angle 60
Figure IV-12: Chord length distribution with different fit curve types 62
Figure IV-13: Twist Angle Distribution with different fit curve types 63
Figure IV-14: Three-Dimensional Rotor Visualization Across All Models Using Qblade" 64
Figure V-1: 3D initial blade formed with both chord and twist distribution 69
Figure V-2: Illustration of the fluid domain with blade 70
Figure V-3: discretization of the fluid domain with a fifteen -layers inflation 71
Figure V-4: discretization of the blade domain using polyhedral mesh with boundary condition 72
Figure V-5: y+ distribution around the blades 73
Figure V-6: Validation with the literature review at the wind speed of V=6 m/s 74

Figure V-7: Twist angle distribution with fitting curve..... 75
Figure V-8: Chord length distribution with fitting curve 76
Figure V-9: goodness-of-fit of the response surface using non-parametric regression and the response surface of (a1), (b1) on the torque value. 78
Figure V-10: Local sensitivity of the design parameters for the torque 79
Figure V-11: Design Exploration Algorithm 80
Figure VI-1: Comparison between (a) Optimal and (b) Original Response surface maps showing the interaction of chord parameters. 83
Figure VI-2: Comparison between (a) Optimal and (b) Original Response surface maps showing the interaction between chord and twist parameters. 84
Figure VI-3: Comparison between a) Optimal Response surface maps b) Original Response surface maps. 84
Figure VI-4: Pressure distribution comparison between the initial and optimal blade at TSR=3. 86
Figure VI-5: Comparison the velocity streamlines between the initial and optimal blade at design TSR. 88
Figure VI-6: limiting streamlines with static pressure contour of optimal and initial rotor at different tip speed ratio..... 90
Figure VI-7: Static torque at different wind speed for both rotors..... 91
Figure VI-8: Blade velocity distribution on the initial rotor(left)and the optimized rotor(right). 93
Figure VI-9: 3D flow visualization on the optimal blade at design TSR..... 94
Figure VI-10: Comparison(a) the torque and(b) power between CFD and Qblade. 95
Figure VI-11: Comparison the thrust force Using CFD and Qblade Approaches. 96
Figure VI-12: Comparison Cm between BEM and CFD. 97
Figure VI-13: Comparison Cp between BEM and CFD..... 98
Figure VI-14: Comparison Ct between BEM and CFD..... 99
Figure VI-15: Comparison Structural Safety Analysis of the Optimized Rotor between BEM and CFD. 100

Liste of tables

Tableau IV-1: Geometric properties of SG604x airfoils family. 49
Tableau IV-2 Aaerodynamic performance of the SG604x airfoil family at Re=40000. 49
Tableau IV-3 : Illustrates the experimental rotor factors 52
Tableau IV-4 :Evaluation of turbine performance using various curve fitting techniques 65
Tableau V-1: Mesh - Independency 71
Tableau V-2: Constraints used in the optimization process 76
Tableau VI-1: Optimum input parameters. 85
Tableau VI-2: Optimum distribution for both chord and twist. 85
Tableau VI-3: performance benefits of all TSR values. 98
Tableau VI-4: Comparison between CFD and Qblade results. 99

NOMENCLATURE

Symbol	Definition
A	Projected Area of Wind Turbine Rotor [m^2].
a	Axial Induction Factor
a'	Tangential Induction Factor
B	Number of Wind Turbine Blades
C_D	Drag Coefficient
C_L	Lift Coefficient
C_P	Coefficient of Power
C_T	Coefficient of Thrust
C_t	Tangential Force Coefficient
c	Chord Length [m]
C_n	Normal Force Coefficient
F	Brandt Correction Factor
F_{hub}	Hub Correction Factor
F_{tip}	Tip Correction Factor
C_t	Tangential Force Coefficient
Htr	Hub Tip Ratio
L/D	Lift/Drag Ratio
C_L/C_D	Glide Ratio
ω	Rotational Speed [Rpm]
m	Mass Flow Rate [kg/s]
P	Output Power [W]
p	Pressure [Pa]
Q	Torque [N.m]
R^2	Coefficient of Correlation
Re	Reynolds Number
r	Local Blade Radius[m]
T	Thrust Force [N]
V	Wind Speed [m/s]

Greek Letters

α_D	Design Angle of attack [°]
β	Twist angle [°]
ε	Turbulent dissipation [m^2/s^3]
ϕ	Flow angle [°]
λ_0	Global tip speed ratio
λ_r	Local tip speed ratio
μ	Dynamic viscosity [Pa.s]
μ_t	Turbulent viscosity [Pa.s]
ν	Kinematic viscosity [m^2/s]
Ω	Angular speed [rad/s]
ω	Specific turbulent dissipation rate[s^{-1}]
ρ	Density [kg/m^3]
σ	Blade solidity
τ_{ij}	Viscous stress tensor [Pa]
θ	Local pitch angle [°]
θ_p	Pitch angle [°]

Abbreviations

2 D	Two dimensional
3 D	Three dimensional
AoA	Angle of Attack [°]
IEA	International Energy Agency
BEM	Blade Element Momentum
BET	Blade Element Theory
CFD	Computational Fluid Dynamics
HAWT	Horizontal Axis Wind Turbine
LE	Leading Edge
NREL	National Renewable Energy Laboratory
OPT	Optimum blade shape
IEC	International Electrotechnical Commission
RSM	Response Surface Method
CCD	Centre Composite Design
DoE	Design of Experiment

TSR	Tip Speed Ratio
VAWT	Vertical Axis Wind Turbine
MOGA	Multi-Objective -Genetic Algorithm
MRF	Moving Reference Frame Model
IB	Induction Blade
HATT	Horizontal Axis Tidal Turbine
DR-HAWT	Dual Rotor Horizontal Axis Wind Turbine
DR-HATT	Dual Rotor Horizontal Axis Tidal Turbine

I. GENERAL INTRODUCTION

I.1 INTRODUCTION

Despite significant political and social efforts to expand renewable energy and mitigate the adverse effects of global warming [1], the global energy infrastructure remains heavily dependent on fossil fuels. Among renewable energy sources, wind energy stands out for its vast potential and widespread availability, both onshore and offshore. Therefore, the effective design of wind turbines is crucial to fully harnessing this abundant resource and optimizing energy production. However, conventional wind energy systems remain incapable to fully exploit this type of energy.

Micro horizontal-axis wind turbines (HAWTs) have emerged as a promising solution for deploying wind energy in urban and remote areas where large-scale turbines are impractical. These small turbines are particularly well-suited for small residential and commercial buildings and contribute significantly to the decentralization of energy production which enhances local energy application.

According to projections of the International Energy Agency (IEA) [2], global energy demand is expected to increase by approximately 25% by 2040, underscoring the importance of exploring and utilizing regions with low to moderate wind speeds. Currently, wind energy development is predominantly focused on high wind speed areas [3]. Figure I-1 illustrates this focus, showing that large-scale turbines are primarily installed in high-speed wind regions where the energy potential is maximized. In contrast, low-speed areas remain largely underexploited, despite their vast availability. This disparity in wind energy exploitation highlights the need for innovative solutions. In fact, the micro HAWTs represent the promising tool in order to effectively harness wind energy in low-speed regions and expand the scope deployment of renewable energy.

Although the definition of low and moderate wind speeds is relative and lacks a standard definition, the International Electrotechnical Commission (IEC) considers average wind speeds below 7.5 m/s to be low [4].

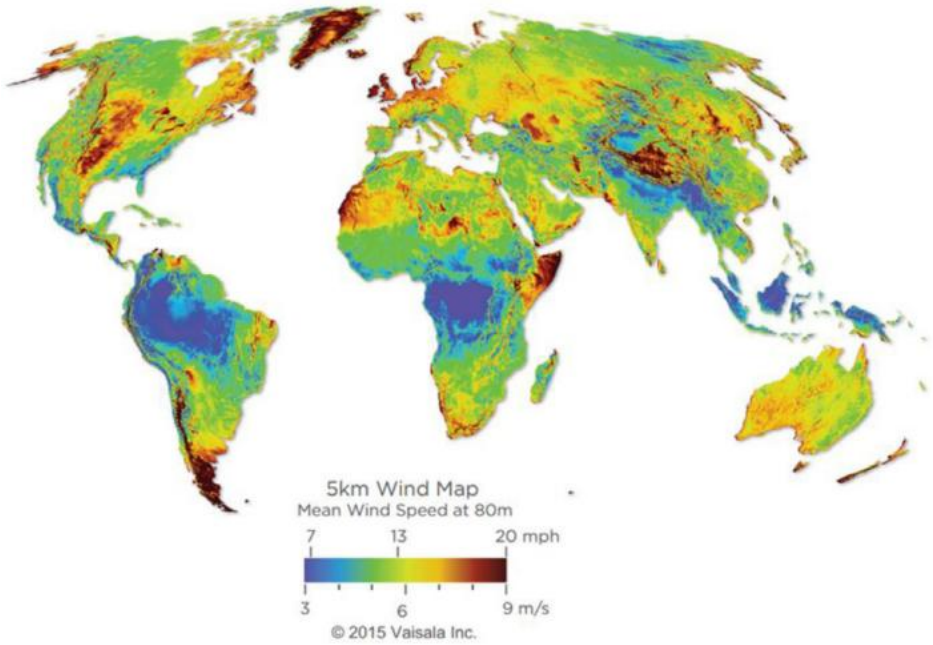


Figure I-1 World onshore wind map at a height of 80 m [5]

I.2 WIND TURBINE

A wind turbine system operates by converting the moving air kinetic energy to shaft mechanical work, which is subsequently transformed to electrical energy through an electrical generator, as depicted in Figure I-2. Wind turbines are engineered in diverse forms and dimensions, each one is tailored to the specific environmental conditions of their intended locations. Among the famous classifications based on the axis disposition, two types are found in the wind turbine field; horizontal and vertical Axis wind Turbines; HAWT and VAWT. As the choice of turbine is influenced by the energy potential of the site a comprehensive understanding of these types is critical and this, in turn, determines the turbine's power output capacity and overall structural design.

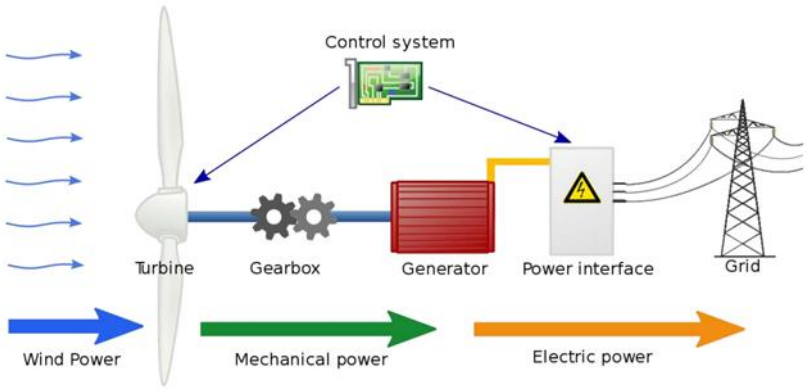


Figure I-2: Wind power converts to electrical power [6]

I.2.1 Horizontal Axis Wind Turbine (HAWT)

Horizontal Axis Wind Turbines (HAWTs) are the most prevalent type used commercially and domestically. They characterize by an axis of rotation parallel to the wind direction, which defines their "horizontal axis" designation. HAWTs operate on the principle of lift generated from the pressure difference between the blade sides which produces driven torque. The three-bladed design, shown in Figure I-3, is the most common configuration. They are highly efficient in converting wind energy into mechanical power. Their performance has been proven reliable through extensive applications. Additionally, HAWTs are cost-effective with respect to both installation and maintenance.



(a) Commercial wind turbine (b) Small domestic scale wind turbine

Figure I-3: Horizontal axis wind turbine [7]

A notable issue with horizontal axis wind turbines is the noise which they generate in both mechanical and aerodynamic components. Mechanical noise arises from internal components such as the gearbox and generator within the nacelle. In contrast, aerodynamic noise usually dominates and presents greater challenges in terms of noise reduction and control.

I.2.2 Vertical Axis Wind Turbine (VAWT)

Vertical axis wind turbines (VAWTs) differ from horizontal axis models in that their rotational axis is perpendicular to the wind direction. They are categorized into two main types: Savonius and Darrieus, which utilize drag and lift principles, respectively. Despite their generally lower efficiency compared to horizontal axis wind turbines (HAWTs), VAWTs are gaining traction in urban areas due to their quieter operation and simpler design. VAWTs do not require a

yaw mechanism for wind alignment and feature ground-level gearboxes and generators, which simplifies maintenance and reduces overall costs. Figure I-4 illustrates the different VAWT types.



Figure I-4: Vertical axis wind turbine categories [8]

I.3 MICRO HAWT

Micro wind turbines are compact systems designed to generate electricity for small-scale applications such as individual homes, cabins, boats, and remote monitoring stations. Typically grated at under 1 kW, these turbines are well-suited for areas with limited space and lower wind speeds. They are lightweight, easy to install, and require minimal infrastructure. By leveraging advanced blade design techniques, micro wind turbines achieve high efficiency and performance in various environments. Their swept areas usually range from 1 to 5 square meters, making them an eco-friendly and cost-effective solution for off-grid and supplementary power needs, figure I-5 illustrates the micro HAWT installation.



Figure I-5: Micro wind turbine installation [9]

I.4 HISTORY OF WIND ENERGY

Wind energy has been utilized since ancient times for tasks such as pumping water and grinding grain. The first recorded use of wind for mechanical power dates back to around 200 BC. European mills, used for agricultural and water extraction purposes, exemplify early wind energy applications (Figure I-6). Today, wind energy holds the potential to power entire nations and supports a sustainable, pollution-free environment, especially for regions with limited electricity access.

In recent decades, wind turbine technology has advanced significantly, increasing their power output by up to 100 times compared to earlier models. The shift from individual turbines to large wind farms, driven by improvements in materials and aerodynamics, has made wind energy more cost-effective. The global wind energy market has grown exponentially since the 1980s, with a fifty-fold increase in capacity from 1990 to 2007, and projections suggest further growth by tenfold by 2030 and twentyfold by 2050[10]. Advancements in materials, such as nano carbon tube composites, are essential for developing larger, more efficient rotor blades, as illustrated in Figure I-7.



Figure I-6: Mill wind turbine [11]

I.5 MODERN WIND TURBINE DESIGN

In modern wind energy technology, the horizontal-axis wind turbine (HAWT) is the most prevalent design. In this setup, the rotor's axis is oriented horizontally, parallel to the ground. The key components of a HAWT, as illustrated in Figure I-7, include several essential elements, such as:

- The rotor: blades and hub
- Drive train Components: Shafts, Gearbox, Brake System, and Generator
- Nacelle: housing and yaw system
- Tower and foundation
- Electrical and control system

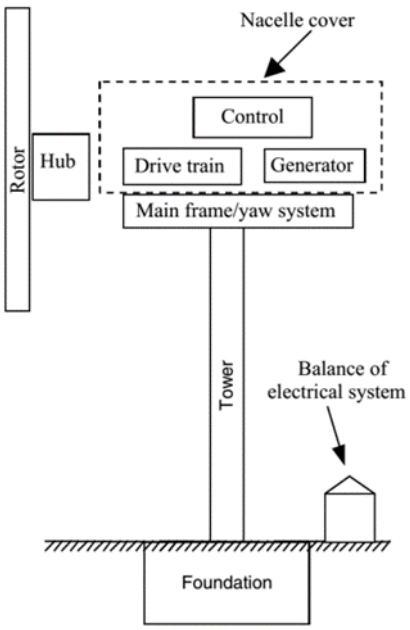


Figure I-7: Major components of a horizontal axis wind turbine [8]

- The primary considerations in the design and construction of wind turbines include:
- Number of blades (commonly two or three)
- Rotor orientation: upwind or downwind of the tower.
- Blade material, construction method, and aerodynamic profile
- Hub design: rigid, teetering, or hinged
- Power control through aerodynamic methods (stall control) or variable-pitch blades (pitch control)
- Fixed or variable rotor speed
- Orientation through self-aligning action (free yaw) or direct control (active yaw)
- Synchronous or induction generator (squirrel cage or doubly fed)
- Gearbox or direct drive generator.

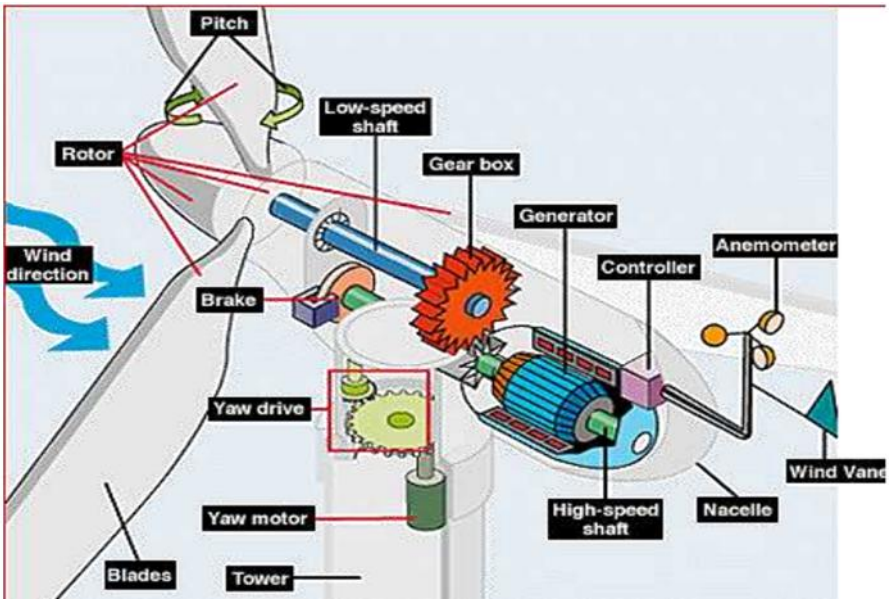


Figure I-8: Detailed view of wind turbine components [8]

I.5.1 Rotor

The rotor, consisting of the hub and blades, is a fundamental component of wind turbines, playing a pivotal role in enhancing both performance and cost-effectiveness. Modern turbine designs predominantly feature three blades, with some manufacturers integrating pitch control mechanisms to optimize the blade angle, as shown in Figure (I-8). In certain mid-sized turbines, especially those found in Denmark, fixed pitch designs are still employed [12]. The blades are typically made from advanced composite materials, including fiberglass-reinforced plastic, epoxy, and wood laminates.

I.5.2 Drive Train

The drive train includes the wind turbine's key rotating components, such as the low-speed and high-speed shafts, gearbox, and generator, as shown in Figure (I-8). Bearings and couplings are also essential parts of this system. The gearbox is critical for transferring mechanical power from the low-speed shaft connected to the rotor to the high-speed shaft, which operates at a suitable rpm to drive the generator. Due to the wind's variability, the drive train is subject to dynamic structural loads, resulting in fluctuating forces on its components.

I.5.3 Generator

Induction generators are the most commonly used in wind turbines due to their advantageous properties. These generators operate at speeds slightly exceeding the synchronous speed; for instance, a four-pole generator runs at approximately 1800 revolutions per minute (rpm) in a 60 Hz grid. Their widespread adoption is attributed to their durability, cost-efficiency, and seamless compatibility with the electrical

I.5.4 Nacelle

The nacelle functions as a protective enclosure housing the essential components of a wind turbine, including the yaw system. This enclosure is designed to safeguard the turbine's internal mechanisms from harsh environmental conditions. As depicted in Figure I-8, the yaw system comprises a motor and a gear drive that work together to adjust the turbine's orientation, ensuring it aligns with the wind direction. The wind direction is detected by an external sensor, typically a wind vane, shown in the figure. Additionally, the brake assembly, also illustrated in Figure I-8, is crucial for maintaining the position of nacelle, providing stability and control and making it a preferred choice in wind energy systems [12].

I.5.5 Tower and Foundation

Wind turbine towers are predominantly built using materials such as steel tubes, trusses, or concrete. The design of these towers typically maintains a ratio of rotor diameter to tower height between 1:1 and 1:1.5. This height ratio is further influenced by the geographic and meteorological conditions at the installation site. Furthermore, the structural integrity and rigidity of the tower are crucial, as the tower must accommodate and mitigate vibrations caused by rotor-induced unsteady wind forces.

I.5.6 Electrical and Control Systems

The electrical and control systems encompass a range of components essential for their operation, as detailed by [12]. These components include:

- **Sensors:** These devices measure various parameters such as speed, position, flow rate, temperature, current, and voltage.

- **Controllers:** These consist of both mechanical mechanisms and electrical circuits responsible for regulating system functions.
- **Power Amplifiers:** This category includes switches, electrical amplifiers, hydraulic pumps, and valves, which are crucial for amplifying power and managing system energy.
- **Actuators:** These components, including motors, pistons, magnets, and solenoids, convert control signals into physical actions.
- **Intelligence:** This refers to computational elements such as computers and microprocessors that provide the processing power necessary for system control and decision-making.

I.6 THE CURRENT PROBLEM

The research efforts in this study were devoted to process the limitations and shortcomings of current models belong in wind turbine area. One of the major shortcomings in the current blade design is the separation phenomenon occurred on both sides of the turbine blades. This undesirable boundary layer detachment leads to a decrease in efficiency under different aerodynamic conditions. Additionally, the turbine's starting capacity reveals as an important aspect which can lead to a substantial increase in operational hours and overall energy output. These two aspects, boundary layer separation and turbine's starting capacity, are considered in this work.

I.7 OBJECTIVE OF THE STUDY

The objective of this study is to apply an optimization methodology to improve the aerodynamic blade geometry of micro HAWT rotor in order to:

1) Delay flow separation zones developed on both blade sides and increase consequently lift production in all operating conditions.
2) Improve the torque produced on the rotor and therefore enhance starting capacity of the turbine which boosts significantly the energy output.

This adjustment allows for greater efficiency and maximizes the generation potential of the system.

I.8 THESIS ORGANIZATION

This work is divided into six chapters:

Chapter 1 provides an overview of wind energy and turbine fundamentals.

Chapter 2 gives the state of the art concerning wind turbine optimization and defines the research objectives and scope.

Chapter 3 explores the fundamental theories for the design and analysis of micro (HAWTs), focusing on Blade Element Momentum (BEM) theory. It also discusses the incorporation of advanced Qblade software tools.

Chapter 4 gives the methodology to identify the optimal geometric factors of a micro HAWT to ensure maximum wind energy absorption using Qblade software.

Chapter 5 presents the CFD tool to study numerically the wind turbine rotor and demonstrates the use of Response Surface Methodology (RSM) through integrated tools for design optimization.

Chapter 6 provides the results and discussion based on comparison between the initial and optimized rotor designs using CFD and Qblade software.

II. Chapter II: Review of Previous Studies

INTRODUCTION

This chapter reviews prior research on advanced optimization techniques applied across various fluid-based energy systems, including wind and marine turbines. It focuses particularly on horizontal-axis wind turbines (HAWTs) due to their prevalence and relevance to this thesis. It explores tools and methods such as Blade Element Momentum (BEM) theory and Computational Fluid Dynamics (CFD), used for rotor design and analysis. The chapter highlights optimization strategies aimed at enhancing turbine performance and blade profiles in diverse systems.

For HAWTs, the goal is to maximize the power coefficient (Cp) to improve efficiency through precise geometric definition of input variables, while two-dimensional studies of airfoil sections focus on increasing the lift-to-drag ratio (CL/Cd). These techniques are categorized based on their effectiveness and application, providing insights into innovations for high-efficiency wind energy systems relevant to this thesis, including the use of surrogate models, which recent studies have shown to outperform deep learning methods in optimization tasks in terms of both time and computational cost, making them a more directed and efficient optimization choice.

II.1 DESIGN AND ANALYSIS OF HAWT ROTORS USING CFD AND BEM METHODS

The blade element momentum (BEM) approach, originally developed for aircraft propeller design [13], has been widely adopted for the analysis and design of wind turbine blades. This method combines momentum theory and blade element theory to predict wind turbine performance, as demonstrated by various researchers [14]-[19].

In addition to these theoretical models, computational fluid dynamics (CFD) has emerged as a critical tool for evaluating wind turbine performance. With appropriate turbulence models, CFD provides detailed insights into aerodynamic behavior. For instance, the authors in [20] employed the k–ω SST turbulence model to assess the aerodynamic performance of an NREL wind turbine, achieving results that aligned well with experimental data at low speeds. Similarly, a 3D CFD model was developed in [21] to analyze the performance of a micro wind turbine, and evaluate the validity of the inverse design BEM (1D BEM) model. Using

experimental data from the NREL Phase IV project, a comparison between the SST and transitional SST turbulence models revealed a discrepancy of less than 6% between simulated and experimental outcomes.

Efforts to enhance wind turbine performance have also focused on the blade root region. A mathematical model was proposed to optimize lift and drag coefficients for different airfoil profiles [22]. A comparative study between CFD and the inverse BEM (IBEM) approach showed strong agreement when the SST turbulence model was applied. Further investigation into small-scale HAWT blades with mixed airfoil configurations (SG 6040 at the root and SG 6043 at the tip) was conducted using CFD and QBlade software, demonstrating promising performance outcomes [23].

More recently, a novel induction blade (IB) design based on BEM theory was introduced [24]. The aerodynamic characteristics of this blade were assessed through CFD simulations using the SST turbulence model. The IB design exhibited a significant improvement, achieving 65% more torque compared to a conventional blade designed solely using BEM theory. This highlights the potential of integrating advanced modeling techniques to optimize wind turbine blade performance.

II.2 CLASSIFICATION OF OPTIMIZATION PROCESSES

Optimization relies on identifying the most influential geometric parameters and selecting the optimal combination to achieve an efficient design. However, the more systematic and directed the method is, the faster and more efficient the optimization becomes.

The process can be categorized into three main approaches:

- Iterative optimization
- Individual parameter optimization using the Response Surface Method
- Combined parameter optimization using the Response Surface Method

II.2.1 Optimizing Through Iterative Processes

Optimization techniques have been employed to improve horizontal-axis wind turbine blades by integrating Genetic Algorithms with Blade Element Momentum (BEM) theory [25]. This method enhances power output by

optimizing critical design parameters such as chord length, twist, and blade profiles, which are defined using NACA airfoils and Bézier curves. Aerodynamic loads are calculated using XFOIL, and the optimization is performed across a high-performance computing cluster utilizing OpenMPI.

A method to design large wind turbine airfoils by optimizing lift coefficients and minimizing chord lengths was proposed in [26] to enhance aerodynamic performance while reducing costs. This approach refines a previously optimized airfoil family using a shape perturbation function, with optimization conducted at a Reynolds number of 16 million. The optimized airfoils exhibit high power coefficients over a broad range of attack angles and maintain performance under surface roughness conditions.

In [27], a Multi-Objective Genetic Algorithm was applied to optimize the USP07-45XX airfoil family for a 20-kW wind turbine. The design focused on achieving high lift-to-drag ratios and resistance to leading-edge roughness. Utilizing the NREL's HARP Opt code, the turbine demonstrated strong performance metrics, including a cut-in speed of 2 m/s and a rated speed of 9 m/s, while maintaining robust annual energy production under soiling conditions.

Further, the Riso_61_18 airfoil was enhanced by optimizing its cavity shape using geometric parameters and a genetic algorithm [28]. This study aimed to maximize the lift-to-drag ratio at specific angles of attack. Experimental results indicated significant improvements in aerodynamic efficiency, with optimized airfoils outperforming standard designs across varying conditions.

A mixed-variable optimization framework for active twist rotor designs was introduced in [29]. This approach combines surrogate-based methods and the Efficient Global Optimization algorithm to improve dynamic twist and vibration control while adhering to design constraints. The framework enabled comprehensive comparisons between mixed and continuous design variables.

In [30], the blade tip planform of a model-scale active twist rotor was optimized. The designs reduced rotor power and improved blade response, achieving up to a 5% performance increase while minimizing vibration control losses. Conversely, designs optimized for maximum twist response enhanced vibration control by 50% with minimal performance trade-offs. A combined optimization approach delivered balanced results, enhancing both performance and vibration control.

II.2.2 Optimizing Individual Input Parameters via Response Surface Methodology (RSM)

The Response Surface Methodology (RSM), introduced in 1951 [31], is a powerful optimization technique that explores the relationships between multiple design variables and response variables. It has been widely applied in wind turbine design to enhance airfoil performance. For instance, an advanced optimization approach integrating RSM with uniform experimental design was developed in [32] to maximize aerodynamic efficiency. By employing B-spline curves to reduce design variables, various airfoil shapes were generated and evaluated, leading to significant performance improvements.

In [33], airfoil optimization for small horizontal-axis wind turbines (HAWTs) was advanced using computational fluid dynamics (CFD) coupled with RSM. The method focused on maximizing thrust and maintaining stability under varying conditions, refined further by the Biobjective Mesh Adaptive Direct Search (BIMADS) algorithm.

Similarly, counter-rotating tidal turbine designs were optimized in [34] using Blade Element Momentum (BEM) theory and validated with CFD, achieving improved performance across all Tip Speed Ratio (TSR) values. In [35], Response Surface Methodology (RSM) was utilized for exhaust air recovery wind turbine optimization, enhancing energy generation while preserving cooling tower efficiency. The study revealed that rotor position, diffuser angle, and separator modifications significantly influence power coefficients.

Moreover, critical design parameters for Darrieus vertical-axis wind turbines (VAWTs) were explored in [36] using CFD and Double Multi-Streamtube (DMST) models. The analysis identified blade number, helical angle, and J-shaped blades as key factors for optimizing power output, achieving a notable 10% performance enhancement.

II.2.3 Combined parameter optimization using the Response Surface Method

Previous research using the Response Surface Methodology (RSM) in micro-scale blade design has primarily focused on optimizing airfoil shapes and setting angles. However, more advanced approaches emphasize identifying critical aerodynamic parameters and optimizing their interactions to enhance blade performance.

Recent studies have applied RSM to optimize input parameter interactions for maximizing efficiency. For instance, a large-scale horizontal-axis wind turbine blade design was developed in [37] using RSM and Blade Element Momentum (BEM) methods, employing specialized software to analyze and optimize the distribution of chord length and twist angle. This approach yielded an 8.7% increase in maximum efficiency compared to the baseline design.

Similarly, [38] enhanced the performance of dual-rotor ducted wind turbines by employing Central Composite Design (CCD) and RSM to optimize factors such as wind speed, turbine spacing ratio, and arrangement type. The study demonstrated high accuracy and reliability of the optimization approach, achieving a maximum power coefficient of approximately 55% under optimal conditions.

Computational Fluid Dynamics (CFD) tools are widely used in conjunction with RSM to refine design optimization. For example, in [39], the geometry of a wind tunnel contraction was optimized to improve flow uniformity by integrating CFD tools with advanced sampling techniques. This approach led to a 38.68% reduction in boundary layer thickness and a 28.43% decrease in momentum thickness compared to traditional designs.

In another application, [40] employed RSM and CFD to optimize a micro radial compressor for turbochargers. By focusing on parameterizing blade geometry, including the beta distribution and splitter blade configuration, the multi-stage optimization process achieved improvement in isentropic efficiency.

In [41], RSM was applied to improve the performance of inertial particle separators by optimizing design parameters, achieving a 3.8% improvement in dust separation efficiency and overall performance.

Recent advancements in RSM include expanding the design space and refining surrogate models to achieve higher accuracy in constructing response surfaces. For instance, [42] investigated the effects of parameters such as tip-speed ratio, mounting angle, and stiffness on vertical-axis wind turbine performance. Using the Kriging model and genetic algorithms, they identified the most impactful parameters, achieving a 1.25% increase in torque after refinement and design space expansion.

II.3 Optimal Design Discovery: Comparing Deep Learning and Surrogate Modeling

Despite the high accuracy of deep learning approaches, their reliance on extensive training data increases computational costs and undermines the goal of optimization. This limitation can be mitigated by employing robust surrogate models, which offer efficient and accurate alternatives for optimal design. Several

studies have highlighted the advantages of surrogate modeling. In [43], an improved Gaussian Process Regression (GPR) model was introduced, incorporating an Adaptive Kernel Construction (AKC) algorithm, which demonstrated exceptional predictive accuracy and robustness. Furthermore, [44] enhanced aerodynamic design by integrating Proper Orthogonal Decomposition (POD) with the AKC-GPR surrogate model, optimizing the UAV-BWB vehicle's configuration and achieving a 14% increase in the lift-to-drag ratio. Additionally, [45] applied a Reduced-Order Model (ROM) to accelerate 3D hypersonic flow predictions, achieving a 35.28% reduction in the mean absolute percentage error (MAPE) compared to baseline models. These advancements underscore the potential of surrogate models as efficient and reliable alternatives to deep learning for design optimization.

II.4 GENERAL REMARKS

This study presents an optimization-based investigation to enhance the performance of a micro wind turbine using the RSM methodology, integrating CFD Analyzer and QBlade software. A surrogate model incorporating non-parametric regression (NPR) and the MOGA method was employed to refine the response. Key input parameters were strategically selected to optimize chord length and twist angle distribution along the blade, modeled through polynomial functions with eight parameters based on the initial blade geometry.

Building on previous research, [46] incorporated experimental data to validate the numerical approach, utilizing a high-accuracy polyhedral mesh and the SG 6043 aerodynamic profile. Additionally, torque analysis across various speeds demonstrated improved start-up performance at lower wind speeds compared to the initial rotor design.

II.5 RESEARCH OBJECTIVES

A review of previous studies reveals a significant scientific gap that this research aims to address through the following objectives:

Development of a Surrogate Model: Establishing a coupled framework between Non-Parametric Regression (NPR) and a Multi-Objective Genetic Algorithm (MOGA), where the initial blade geometry is defined using fitted parametric curves for chord length and twist angle. The coefficients of these fitted functions are then used to construct a Design of Experiments (DOE) matrix through Central Composite Design (CCD), allowing for the generation of high-

quality design points and enabling a more accurate and efficient optimization process.

Performance Enhancement Using Response Surface Methodology (RSM): Applying RSM to optimize the performance of small-scale turbines by analyzing the combined effects of chord length and twist angle distributions using Computational Fluid Dynamics (CFD) simulations.

Optimization Impact on Startup Performance: Investigating the influence of the proposed optimization strategy on improving the turbine's starting capability.

Performance Evaluation Under Varying Operating Conditions: Assessing the impact of the optimized design across different operational scenarios to ensure adaptability and efficiency.

Comparative Validation: Enhancing the reliability of performance assessments by comparing results obtained from QBlade and CFD software.

Structural Integrity Analysis: Evaluating the structural robustness of the optimized rotor under operational conditions to ensure durability and stability.

III. Chapter III: Aerodynamics and Advanced Design of Micro HAWTs: Insights from QBlade Analysis

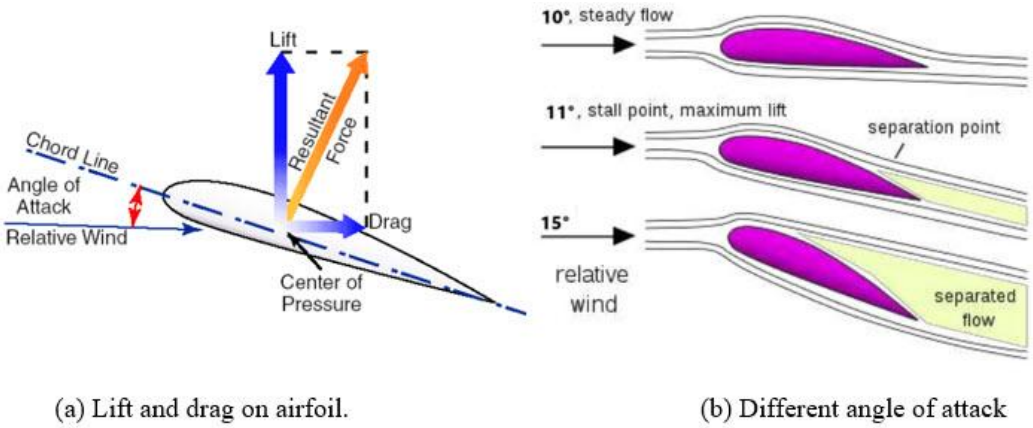
INTRODUCTION

Micro horizontal-axis wind turbines (HAWTs) are compact systems designed to efficiently harness wind energy for personal applications. Key aerodynamic factors, such as blade shape, angle of attack, and wind flow dynamics, are crucial for best power output and ensuring smooth operation. Performance is influenced by tip and hub losses, which reduce effective lift and overall efficiency. Furthermore, the well radial distribution obtained for the chord length and twist angle of the micro HAWTs is essential for maximizing performance. QBlade is an advanced open-source software based on blade element and momentum methodology which facilitates the design and analysis task performed in this chapter by enabling precise 3D blade modeling and evaluating aerodynamic characteristics.

In this work, a comparative study was conducted between employing Prandtl's and Shen's tip and root loss corrections and operating without any corrections, in conjunction with experimental results to evaluate the performance and strengthen the selection of the most appropriate correction approach for this section.

III.1 MECHANISM OF WIND POWER CAPTURE BY BLADE SECTION

Wind turbine blades, much like airplane wings, generate lift due to their aerodynamic shape. The curvature of the blade creates a low-pressure region on the convex side, while higher-pressure air pushes against the flatter side of the airfoil. This pressure difference produces a lift force that is perpendicular to the direction of airflow, as illustrated in Figure III-1a. The magnitude of the lift force increases as the blade is positioned at a greater angle to the wind, known as the angle of attack. However, if the angle of attack becomes too large, the blade can experience "stall," resulting in a significant decrease in lift. Therefore, there is an optimal angle of attack that maximizes lift, as shown in Figure III-1b. Furthermore, the lift coefficient can be evaluated across various flow conditions over the SG6043 airfoil profile at a Reynolds number of 40000. This analysis encompasses a comprehensive range of aerodynamic scenarios, highlighting the airfoil's performance characteristics under distinct flow regimes Figure III-2.



(a) Lift and drag on airfoil. (b) Different angle of attack

Figure III-1: Lift coefficient variation VS angle of attack [8]

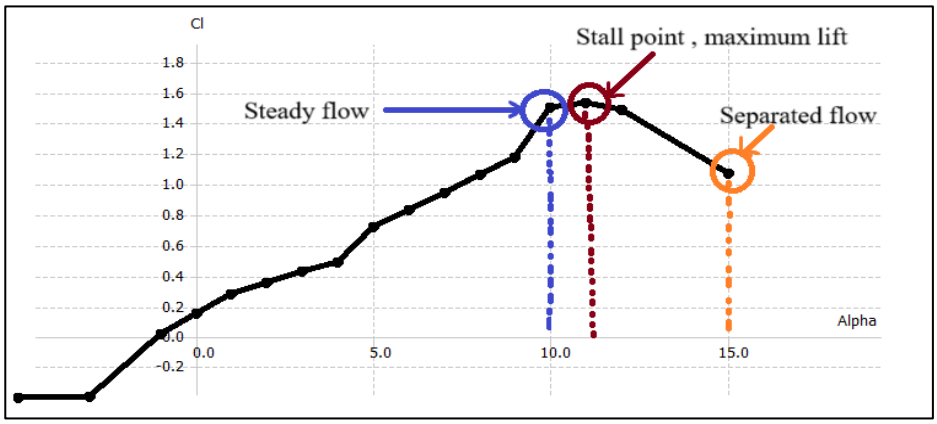


Figure III-2: Lift coefficient variation VS angle of attack.

Wind turbine blades not only generate lift but also experience a retarding force known as drag. Drag acts parallel to the wind flow and increases with the angle of attack. When the airfoil shape is optimal, the lift force is much greater than the drag force. However, at very high angles of attack, especially when the blade stalls, drag increases significantly. Therefore, the blade reaches its maximum lift-to-drag ratio at an angle slightly less than the angle that produces maximum lift, identifying the ideal operating point between these two angles.

Although drag acts downwind and seems irrelevant to turbine performance since it is parallel to the turbine axis and does not directly slow the rotor, this force, known as thrust, does not inherently affect the rotor's speed. While this holds true when the rotor is stationary (e.g., just before startup), the blade's movement through the air changes the perceived wind angle. This alteration in relative wind direction due to the blade's motion affects the overall aerodynamic forces acting on the blade, influencing turbine performance.

The relative wind velocity encountered by the blade is higher and comes from a different angle than the actual wind velocity. As a result, the lift and drag forces based on the relative wind speed differ in both magnitude and direction from those based on the true wind speed. This means that the lift force contributes

to the rotor's thrust, as shown in Figure III-3. Consequently, to maintain an optimal angle of attack, the blade must be adjusted to a position further from the true wind angle.

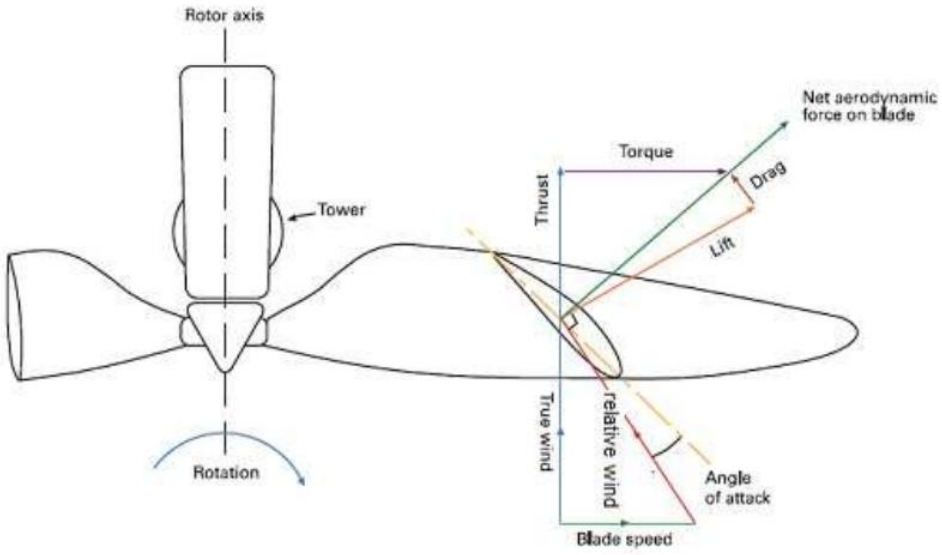


Figure III-3: Velocities and forces on turbine blade [8]

III.2 AIRFOILS AND FUNDAMENTAL AERODYNAMIC PRINCIPLES

Airfoils, with their specific geometric shapes, generate mechanical forces through their interaction with surrounding fluids. Wind turbine blades, designed as airfoils, convert this interaction into mechanical power. Both width and length of blade are optimized for aerodynamic performance, rotor power, airfoil properties, and structural strength. Understanding wind turbine power generation requires a foundational grasp of these aerodynamic concepts.

III.2.1 Airfoil Terminology

Key terms define airfoil geometry, as illustrated in Figure III.4. The mean camber line represents points equidistant between the airfoil's upper and lower surfaces, extending from the leading to the trailing edge. The chord line is the straight line joining these edges, with its length termed the chord (c). Camber refers to the perpendicular distance between the mean camber line and the chord line, while thickness is the perpendicular distance between the upper and lower surfaces. The angle of attack (α) is the angle between the relative wind (U) and the chord

line [8]. The figure does not depict the airfoil's span, which is its length perpendicular to the cross-section. Key geometric parameters influencing an airfoil's aerodynamic performance include the leading-edge radius, mean camber line, maximum thickness, thickness distribution, and trailing edge angle (between the chord line and the trailing edge line).

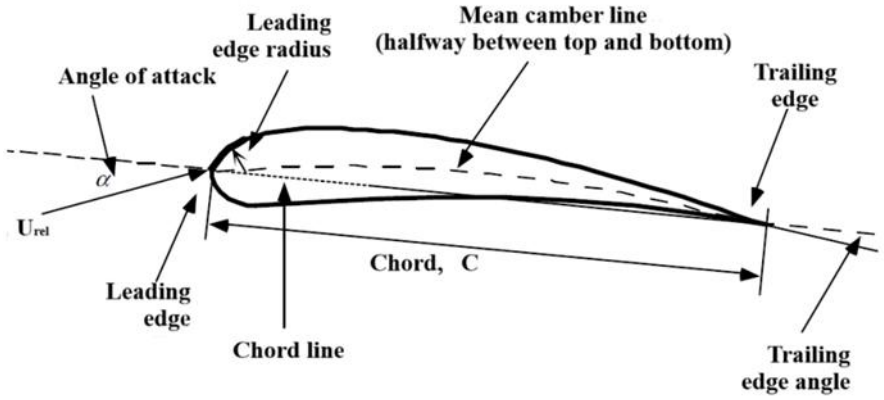


Figure III-4: Airfoil Nomenclature [8]

III.2.2 Lift, Drag, and Non-Dimensional Parameters in Wind Turbine Blades Profile

Airflow around an airfoil generates various force distributions along its surface. The velocity of the air increases over the convex side, leading to a lower average pressure on the 'suction' side compared to the concave or 'pressure' side. Concurrently, viscous friction between the air and the airfoil surface decelerates the airflow near the surface to some degree.

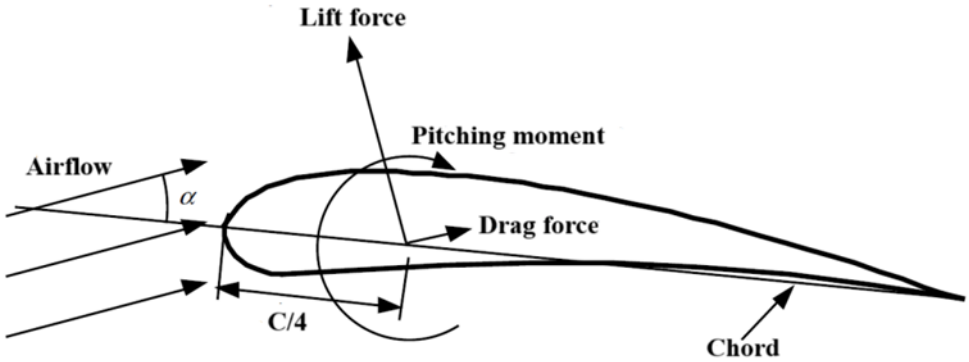


Figure III-5: Forces and moments on an airfoil section [8]

As illustrated in Figure (III-5), the combined effect of all pressure and friction forces can be simplified into two distinct forces and a moment. These act along the chord line at a point located one-fourth of the chord length from the leading edge, also known as the 'quarter chord' position [47].

Lift Force: This force acts perpendicular to the direction of the incoming airflow and arises from the pressure differential between the upper and lower surfaces of the airfoil.

Drag Force: Drag force is the aerodynamic resistance acting parallel to the incoming airflow, arising from two main factors: viscous friction at the airfoil's surface and pressure differences between the surfaces facing toward and away from the flow.

Pitching Moment: This moment acts around an axis perpendicular to the airfoil cross-section, from the flow.

Both theoretical analysis and experimental research have revealed that numerous fluid flow problems can be effectively described using non-dimensional parameters. Among these, the Reynolds number stands out as the most significant for defining the characteristics of fluid flow conditions, and it is defined as follows:

$$\mathrm{Re} = \frac{\rho U c}{\mu} \quad \textbf{(III.1)}$$

Where:

ρ: The fluid density

U: The wind speed

c: The airfoil chord

μ: The fluid dynamic viscosity

Additional non-dimensional force and moment coefficients, which are functions of the Reynolds number, can be defined for both two-dimensional and three-dimensional objects based on empirical data obtained from wind tunnel tests. For three-dimensional airfoils, the finite span introduces complexities as the force and moment coefficients are significantly influenced by the flow around the airfoil limits, often referred to as end effects. In contrast, two-dimensional airfoil data assumes an infinite span, thereby eliminating any end effects from consideration.

In rotor design, the application of two-dimensional coefficients is standard practice. These coefficients are determined from wind tunnel tests conducted over a range of angles of attack and Reynolds numbers. The resulting data provide essential insights for aerodynamic performance predictions. Specifically, the two-dimensional lift coefficient, a crucial parameter in these analyses, is defined as:

$$C_L = \frac{L}{\frac{1}{2}\rho U^2 A} \quad \textbf{(III.2)}$$

The two- dimensional drag coefficient is defined as:

$$C_d = \frac{D}{\frac{1}{2}\rho U^2 A} \quad \textbf{(III.3)}$$

The pitching moment coefficient is:

$$C_m = -\frac{M}{\frac{1}{2}\rho U^2 Ac} \quad \textbf{(III.4)}$$

Where:
L: Lift Force
D: Drag Force
M: Pitching Moment
A: Airfoil Area = Chord × Span

III.2.3 Airfoil selection

Micro wind turbines, designed for low wind speed environments, benefit significantly from the aerodynamic properties of the SG (Selig-Gough) family of airfoils [48]. The SG6043 airfoil, notable for its balanced performance, has a maximum thickness of 10% at 32.1% chord length and a maximum camber of 5.1% at 53.3% chord length. These features ensure low drag and sufficient structural integrity, making it ideal for various low-wind-speed scenarios. The SG6043 exhibits a high lift-to-drag ratio, crucial for efficient energy conversion in small-scale turbines, and has favorable stall characteristics to prevent sudden lift loss. Figure (III-6) illustrates the SG6043 airfoil shape, highlighting its streamlined profile designed for optimal performance in micro wind turbine applications.

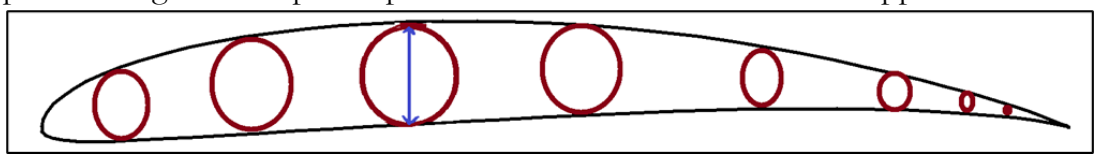


Figure III-6: SG6043 airfoil sheep with max thickness

III.3 AERODYNAMIC THEORIES OF WIND TURBINES

Wind turbines are designed to capture kinetic energy from the wind. Physics dictates that any moving fluid has kinetic energy, however, only part of this wind energy can be harnessed by the turbine.in axial direction the velocity decreases and in radial direction, the airflow is separated in two zones;

The first zone near the rotor is qualified affected flow and the second far the rotor is characterized by unaffected flow, a boundary surface between the two zones can be defined. This boundary, extending from upstream to downstream and creates a divergent stream tube, as shown in Figure III-7.

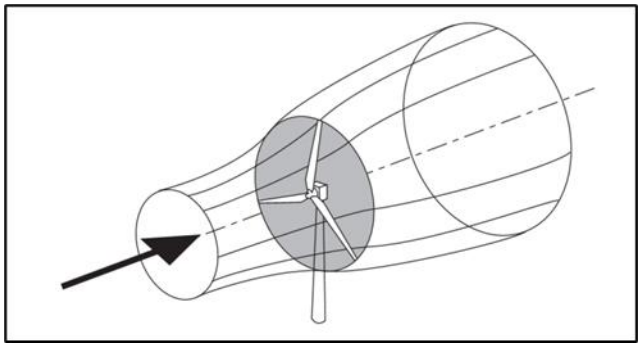


Figure III-7: Wind energy extraction stream tube [49]

wind turbine, with assumptions such as inviscid, incompressible, steady flow, and uniform velocity through any cross section along the stream tube axis. Glauert later introduced the Blade Element Momentum (BEM) methodology, combining both momentum and blade element theories to predict rotor performance [49].

III.3.1 Actuator Disc Model

The actuator disc model, also known as the actuator disc theory, is the most basic analytical tool for understanding the aerodynamic behavior of a wind turbine. Based on linear momentum theory, this model is extensively employed to predict the performance of propellers. As depicted in Figure III-8, the control volume within this one-dimensional framework consists of a surface stream tube with two cross sections. Airflow is presumed to pass through the ends of the stream tube. In this representation, the turbine is modeled as a circular disc positioned at the middle of the stream tube in axial direction. This model is specifically used to evaluate the overall efficiency of wind turbines. It is important to note that this analysis is applicable to any type of wind turbine. The analysis is based on the following assumptions:

- The model is assumed as 1D
- The fluid flow is homogeneous, incompressible, and in a steady state
- There is no frictional drag
- The number of blades is infinite
- The wake is non-rotating
- The static pressure both far upstream and far downstream of the rotor matches the undisturbed ambient static pressure

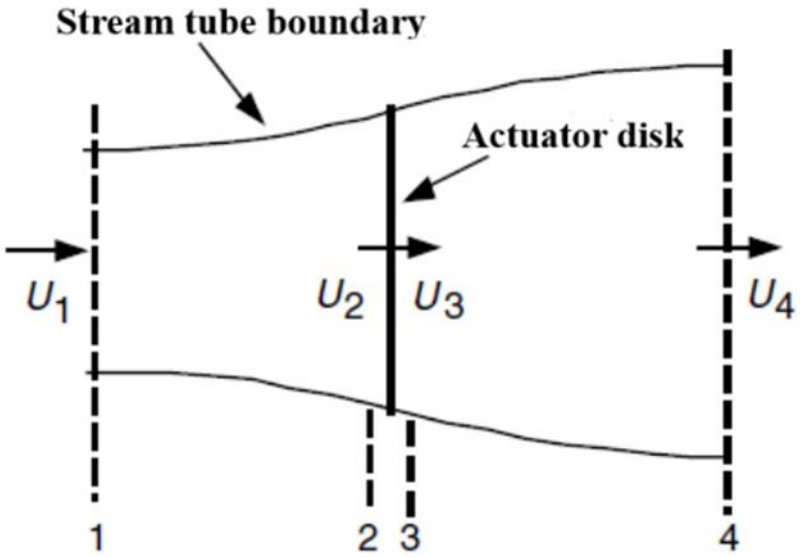


Figure III-8: Actuator disc stream-tube [49]

Before reaching the disc, the stream-tube has a smaller cross-sectional area compared to the disc itself, whereas beyond the disc, the area becomes larger. This expansion is necessary to maintain a constant mass flow rate throughout the stream-tube. The amount of air passing through a specific cross-section of the stream-tube per unit time can be expressed as ρUA, where ρ represents air density, U is the flow velocity, and A is the cross-sectional area. Thus, the mass flow rate must be consistent at all points along the stream-tube, and so:

$$m_1 = m_2 = m_3 = m_4 \quad \textbf{(III.5)}$$

$$\rho_1 U_1 A_1 = \rho_2 U_2 A_2 = \rho_3 U_3 A_3 = \rho_4 U_4 A_4 \quad \textbf{(III.6)}$$

Where: U represents the wind velocity

Due to the existence of the rotor in the control volume the total energy differs between the upstream and downstream sections. Bernoulli equation is utilized to derive the relevant equations. According to Bernoulli principle, the total energy within a fluid flow-comprising kinetic energy, static pressure energy, and gravitational potential energy-remains unchanged as long as no external work is performed on the fluid [47].

Neglecting any losses, Bernoulli equation is written in the upstream portion of the stream tube as follow:

$$P_1 + \frac{1}{2}\rho U_1^2 = P_2 + \frac{1}{2}\rho U_2^2 \quad \textbf{(III.7)}$$

The downstream portion of the stream tube is described as follows:

$$P_3 + \frac{1}{2}\rho U_3^2 = P_4 + \frac{1}{2}\rho U_4^2 \quad \textbf{(III.8)}$$

Utilizing the conservation of linear momentum within the control volume, we can calculate the net force acting on the turbine. This force is equal in

magnitude but opposite in direction to the thrust, T. Thrust represents the rate at which momentum changes in the airflow and its expression is obtained as follows:

To determine the pressure differential across the actuator disc, we have:

$$P_2 = P_1 + \frac{1}{2}\rho U_1^2 - \frac{1}{2}\rho U_2^2 \quad \textbf{(III.9)}$$

$$P_3 = P_4 + \frac{1}{2}\rho U_4^2 - \frac{1}{2}\rho U_3^2 \quad \textbf{(III.10)}$$

Assuming that ($P_1 = P_4$) and ($U_2 = U_3$), the thrust can be represented as the net difference in forces exerted on either side of the actuator disc:

$$T = A_2(P_2 - P_3) \quad \textbf{(III.11)}$$

The pressure difference between the front and rear of the turbine can be calculated and is expressed as:

$$P_2 - P_3 = \frac{1}{2}\,\rho(U_1^2 - U_4^2) \quad \textbf{(III.12)}$$

Substituting equation (III.11) into equation (III.10) yields:

$$T = \frac{1}{2}\,\rho A_2(U_1^2 - U_4^2) \quad \textbf{(III.13)}$$

Or

$$T = U_1(\rho UA)_1 - U_4(\rho UA)_4 \quad \textbf{(III.14)}$$

Continuity equation gives:

$$T = m(U_1 - U_4) = \frac{1}{2}\rho A_2(U_1^2 - U_4^2) \quad \textbf{(III.15)}$$

$$\rho A_2 U_2(U_1 - U_4) = \frac{1}{2}\rho A_2(U_1 - U_4)(U_1 + U_4) \quad \textbf{(III.16)}$$

$$U_2 = \frac{1}{2}(U_1 + U_4) \quad \textbf{(III.17)}$$

The actuator disk generates a velocity within the stream tube, characterized by the axial induction factor (a), which quantifies the relative reduction in wind speed from the free-stream to the turbine plane. This is represented as:

$$a = \frac{U_1 - U_2}{U_1} \quad \textbf{(III.18)}$$

$$U_2 = U_1(1 - a) \quad \textbf{(III.19)}$$

From equation (III.17) and (III.19),

The wind speed at the wake station is:

$$\frac{1}{2}(U_1 + U_4) = U_1(1 - a) \quad \textbf{(III.20)}$$

$$U_4 = U_1(1 - 2a) \quad \textbf{(III.21)}$$

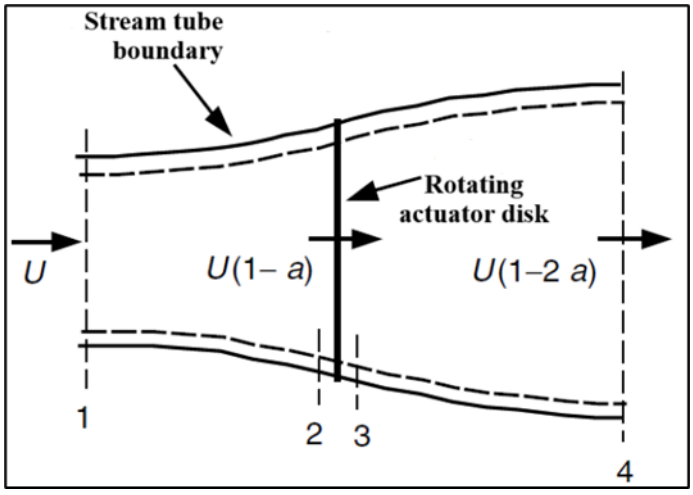


Figure III-9: Wind speeds at different stations of the stream tube [49]

The term a U_1 denotes the induced velocity at the turbine. The wind velocity consists of both the free-stream velocity and the induced velocity. As the induction factor increases, the speed in the wake decreases substantially. When the induction factor nears its maximum value of 0.5, the wind speed downstream of the disc drops to zero. For the actuator disc theory to be valid, the wake speed must remain above zero. Consequently, the turbine power output is determined by the product of thrust and the velocity at the disc.

$$P = \frac{1}{2}\rho A_2(U_1^2 - U_4^2)U_2$$

$$P = \frac{1}{2}\rho A_2 U_2(U_1 - U_4)(U_1 + U_4) \quad \textbf{(III.22)}$$

By substituting equation (III.19) and (III.21) into (III.22):

$$P = \frac{1}{2}\rho A_2 U_1^3 4\alpha(1-a)^2$$

$$P = \frac{1}{2}\rho A U^3 4\alpha(1-a)^2 \quad \textbf{(III.23)}$$

Where:

A: The turbine swept area

U: The free stream velocity

The power coefficient is a dimensionless parameter used to assess the efficiency of a turbine. It is calculated by dividing the power extracted via turbine by the power available in the wind. This coefficient can be defined as:

$$C_\rho = \frac{Turbine\ Power\ Output}{Power\ in\ the\ wind}$$

$$C_\rho = \frac{P}{\frac{1}{2}pAU^3} \quad \textbf{(III.24)}$$

The power coefficient is expressed in term of induction factor a as:

$$C_\rho = 4a(1-a)^2 \quad \textbf{(III.25)}$$

Using the condition:

$$\frac{dC_\rho}{da} = 0 \qquad \textbf{(III.26)}$$

The maximum power coefficient corresponds to induction factor value of 0.33 and is equal to:

$$C_{Pmax} = \frac{16}{27} = 0{,}5926 \qquad \textbf{(III.27)}$$

According to equation (III.26), the highest power coefficient obtainable by an ideal turbine, known as the Betz limit after German aerodynamicist Albert Betz, is 59%. To achieve this power coefficient, the axial induction factor (a) must be set to 1/3, implying that the wind velocity downstream must be reduced to one-third of the upstream velocity. Additionally, the coefficient of thrust is also expressed as a dimensionless value.

$$C_T = \frac{Thrust\ Force}{Dynamic\ Force}$$

$$C_T = \frac{T}{\frac{1}{2}pAU^2} \qquad \textbf{(III.28)}$$

Figure (III-10) depicts the variation of power coefficient, thrust coefficient and dimensionless downstream wind speed of an ideal turbine with respect to axial induction factor. It demonstrates that the theoretical maximum efficiency of an ideal turbine is around 59%, achievable only if the axial induction factor is less than 0.4. In practical scenarios, however, the efficiency of a well-designed turbine is often below this theoretical limit. Additionally, while the thrust coefficient can sometimes exceed the ideal maximum, real-case factors such as blade drag and tip losses contribute to decreased efficiency and are not considered in the ideal model.

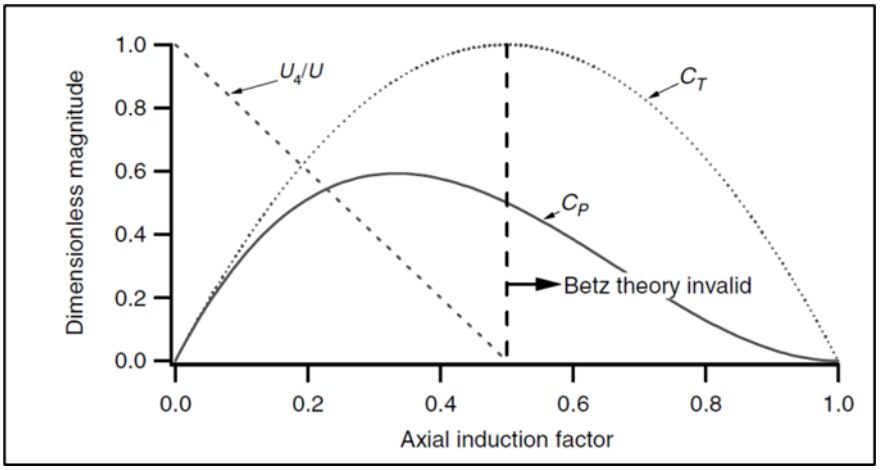


Figure III-10: The variation in Cp and CT with axial induction factor [8].

III.3.2 Wake Rotation

Linear momentum theory suggests no rotational flow in the turbine wake, but the actual flow rotates downstream. The air torque on the turbine causes counter-rotation, adding tangential velocity to the axial flow. This rotational flow reduces energy extraction efficiency, leading to kinetic energy losses. Turbines with low rotational speed and high torque suffer significant losses, while those with high rotational speed and low torque face minimal losses [50].

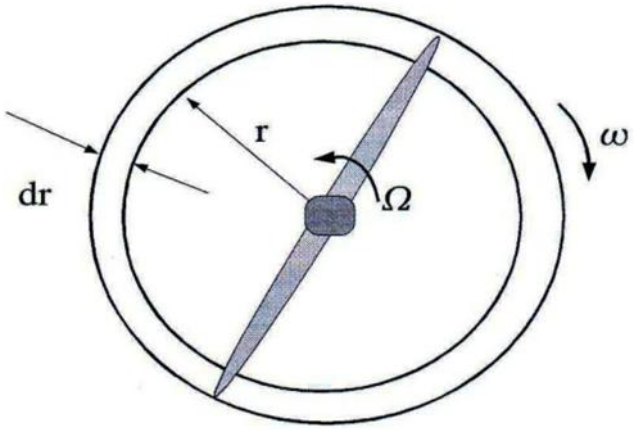


Figure III-11: Blade Element length dr at radius r [50]

The tangential velocity varies across radial positions, affecting the axial induced velocity. To analyze these changes, an annular ring of the rotor disk with radius r and width dr is considered, as shown in Figure III-11. The angular velocity of the air relative to the blades increases from Ω (turbine blade's angular velocity) to $\Omega + \omega$ where ω (air flow's angular velocity in the wake).

The torque exerted on the ring corresponds to the rate of change of angular momentum of the air flowing through it. Thus:

Torque = mass flow rate x changes of tangential velocity x radius

$$\delta Q = \rho \delta A U_\infty (1-a) 2\Omega a' r^2 \quad \textbf{(III.29)}$$

Angular induction factor is defined as:

$$a' = \frac{\omega}{2\Omega} \quad \textbf{(III.30)}$$

The induced velocity at the rotor includes both axial components, Ua and $r\,\Omega a'$ Consequently, the thrust can be described as [51].

$$dT = 4a'(1+a')\frac{1}{2}\rho\Omega^2\, r^2 2\pi\, r dr \quad \textbf{(III.31)}$$

Based on linear momentum theory, the rotor's thrust can be expressed in terms of the axial induction factor as follows:

$$dT = 4a(1-a)\frac{1}{2}\rho\, U^2 2\pi\, r dr \quad \textbf{(III.32)}$$

By setting equations (III.30) and (III.31) equal to each other, we obtain:

$$\frac{a(1-a)}{a'(1+a')} = \frac{\Omega^2 r^2}{U^2}\lambda_r^2 \quad \textbf{(III.33)}$$

The tip speed ratio is the ratio of the speed of the blade tips to the free-stream wind speed and is represented as:

$$\lambda = \frac{\Omega R}{U_\infty} = \sqrt{a(1-a)/a'(1+a')} \quad \textbf{(III.33)}$$

III.3.3 Blade Element Theory (BET)

Blade Element Theory (BET) is utilized to predict the forces on a turbine blade by analyzing the lift and drag forces generated along the blade span. This theory involves dividing the blade into several sections along its span. Each section functions independently, behaving as a 2D airfoil. Aerodynamic forces on each airfoil section are calculated based on the local flow conditions. The overall forces and moments acting on the turbine blade are then obtained by summing the forces from all sections. BET relies on several assumptions: there is no aerodynamic interaction between the blade elements, meaning no radial flow, and the forces on the blades are determined solely by the lift and drag characteristics of the airfoil shape. Figure III-12 shows the wind turbine blade divided into multiple sections.

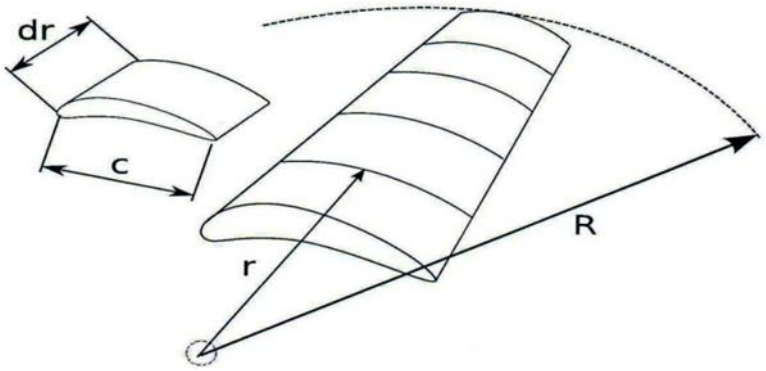


Figure III-2: Wind turbine blade divided into a series number of sections [8]

To calculate the relative wind velocity at a specific section of the blade, both the axial and tangential components of velocity are combined. This resultant velocity is then used to determine the lift and drag forces for each section of the blade. Figure III-13 depicts a wind turbine section with N blades, a tip radius R and a chord length c. Assuming the blades rotate with an angular velocity Ω, let U_∞ represent the wind speed, and ϕ be the angle between the relative wind velocity and the plane of rotation.

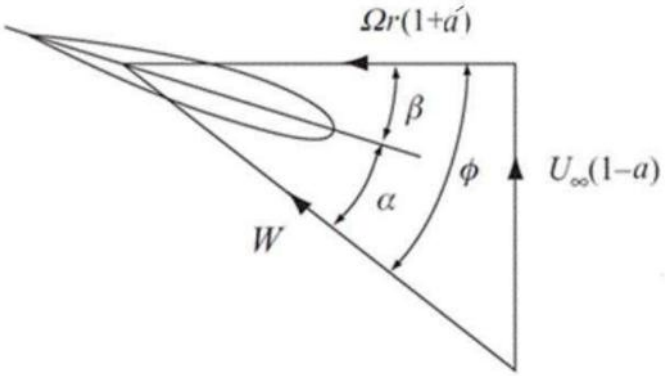


Figure III-3: Velocities on blade element [52]

According to the diagram in Figure III-13, the components of velocity vector is depicted as:

$$U_A = U_\infty(1-a) \quad \textbf{(III.34)}$$

$$U_T = \Omega r(1+a') \quad \textbf{(III.35)}$$

Where:

U_A: Axial velocity of the wind

U_T: Tangential velocity of the wind

The relative wind velocity can subsequently be expressed as:

$$w = \sqrt{[U_\infty(1-a)]^2 + [\Omega r(1+a')]^2} \quad \textbf{(III.36)}$$

The angle at which the relative wind velocity aligns with the plane of rotation is described by:

$$\phi = tan^{-1}\left[\frac{U_\infty(1-a)}{\Omega r(1+a')}\right] = tan^{-1}\left[\frac{1-a}{(1+a')\lambda_r}\right] \quad \textbf{(III.37)}$$

The angle of attack, defined as the angle between the chord line and the relative wind velocity, is expressed as:

$$\alpha = \phi - \beta \quad \textbf{(III.38)}$$

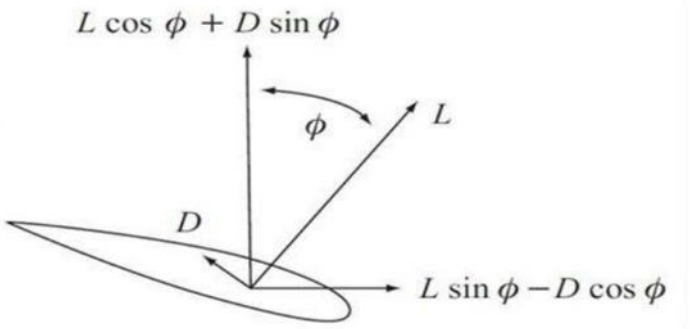


Figure III-4: Forces on blade element [52]

Lift is the force directed perpendicular to the relative wind velocity, whereas drag is the force aligned parallel to it. Both of these forces acting on the airfoil are

calculated using the relative wind velocity. The formulas for lift and drag forces are:

$$\delta L = \frac{1}{2} C_L \, \rho \, A w^2 c \, \delta r \quad \textbf{(III.39)}$$

$$\delta D = \frac{1}{2} C_D \, \rho \, A w^2 c \, \delta r \quad \textbf{(III.40)}$$

The lift and drag forces on the airfoil, illustrated in Figure III-14, are divided into two components. One component is aligned with the plane of rotation, and the other is perpendicular to it. The component in the plane of rotation contributes to the turbine torque, while the perpendicular component produces thrust. The formulas for these forces, both in the plane of rotation and perpendicular to it, are as follows:

$$\delta F_A = \delta L \cos \phi + \delta D \sin \phi \quad \textbf{(III.41)}$$

$$\delta F_T = \delta L \sin \phi - \delta D \cos \phi \quad \textbf{(III.42)}$$

III.3.4 Blade Element Momentum (BEM) Theory

Blade element momentum (BEM) method integrates principles from both blade element theory and momentum theory. It based on an iterative approach for calculating the induced velocities and aerodynamic forces acting on wind turbine blades. Although BEM theory is extensively utilized, it simplifies several aspects to enhance usability. The combination of equations (III.39) and (III.40) into equation (III.41) yields the total thrust exerted by the turbine, as outlined by Ali (2014).

$$\delta T = \frac{1}{2} \rho \, W^2 \, B \, c \, (C_L \cos \phi + C_D \sin \phi) \, dr \quad \textbf{(III.43)}$$

Similar to thrust, the overall torque can be determined by integrating equations (III.39) and (III.40) into equation (III.42). This combined equation provides the total torque value.

$$dQ = 4\pi \rho \, r^3 \, U a' (1 - a) F dr \quad \textbf{(III.44)}$$

If we view thrust as the rate at which linear momentum changes for the flow passing through an annular section at a radius r with a width dr and considering a tip loss factor F, then thrust can be represented as follows:

$$dT = 4\pi \, \rho \, r \, U^2 \alpha (1 - a) F dr \quad \textbf{(III.45)}$$

To determine the values of the induction factors a' and a, an iterative process involving equations (III.45) and (III.43) must be employed. The right-hand side of the equation (III.45) is computed using the current values of the flow induction factors. Equations (III.43) and (III.37) are then applied to both the torque and thrust equations to solve for the axial a and tangential a' velocities. This process yields:

$$\frac{a}{1-a} = \frac{\sigma(C_L + C_D \tan\phi)}{4F \tan\phi \sin\phi} \quad \textbf{(III.46)}$$

$$\frac{a'}{1+a'} = \frac{\sigma(C_L + C_D \tan\phi)}{4F \tan\phi \sin\phi} \quad \textbf{(III.47)}$$

Blade solidity σ is defined as the ratio of the total blade area to the rotor disc area and is expressed as:

$$\sigma = \frac{Bc}{2\pi r} \quad \textbf{(III.48)}$$

It is essential to recognize that Blade Element Momentum (BEM) theory is valid only when the blades have a consistent circulation, indicated by a uniform a. When circulation a is non-uniform, radial interactions and momentum exchanges take place between the flows in adjacent annular ring elements.

III.4 HAWT Design and Analysis with QBlade

This section highlights the fundamental concepts and effective tools for designing and analyzing the performance of micro horizontal-axis wind turbines (HAWTs) using Qblade software.

III.4.1 Qblade V 0.96 Interface



Figure III-15: Main Interface of Qblade

Qblade has an intuitive interface designed to perform aerodynamic analysis for both horizontal and vertical axis wind turbines. As shown in Figure III-15, the main interface provides seamless navigation and easy access to functionalities like airfoil and rotor design, performance simulations, and data visualization tools.

Clearly labeled menus and toolbars enhance workflow efficiency, supporting both novice and experienced users in conducting rigorous aerodynamic studies.

III.4.2 Overview of Qblade Tools

Qblade offers a robust set of tools for aerodynamic analysis of wind turbine blades, generally, and airfoils, particularly, supporting both academic research and practical engineering applications.

III.4.2.1 Data Import and Export tool

Qblade allows smooth import and export of data, such as airfoil coordinates, polar data, and rotor geometries. For instance, Figure III-16 shows the SG 6043 airfoil shape imported into Qblade. This feature enhances Qblade integration with other design and analysis tools and facilitates the overall design process.

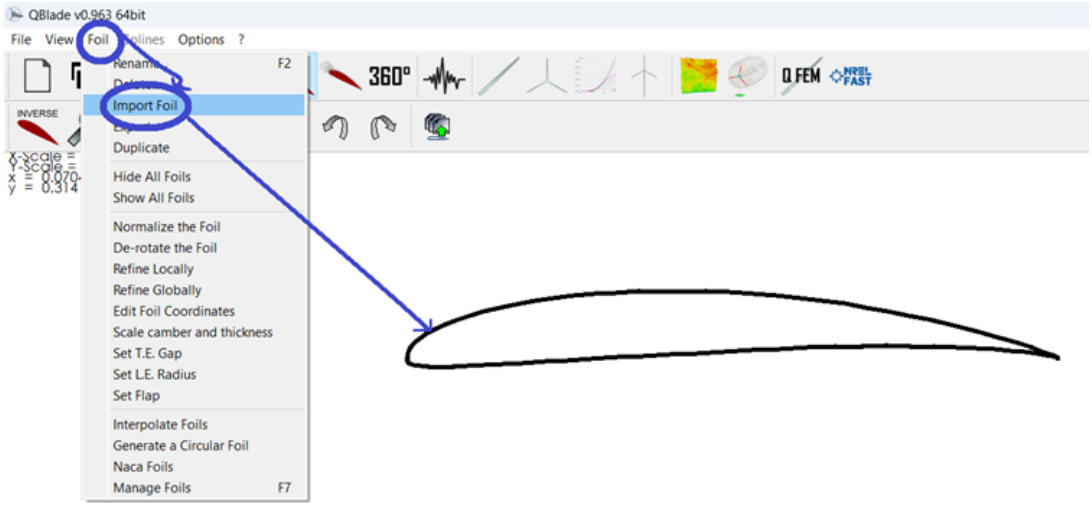


Figure III-16: Import SG6043 airfoil using foil option

III.4.2.2 Overview of XFOIL module

XFOIL, developed by Mark Drela in 1986, is a prominent tool for analyzing subsonic airfoils and generating profile polars. It combines high-order panel methods with viscous/inviscid interaction techniques. Evolving from a command-line tool to a sophisticated cross-platform application with a graphical interface, XFOIL core algorithms have remained consistent. The XFOIL 6.94 User Guide remains applicable across all versions [51].

III.4.2.2.1 XFOIL Direct Analysis Module

The XFOIL Direct Analysis module performs airfoil flow simulations to generate polar, as illustrated in Figure III-17. Initiated through the Polar menu, simulations typically converge over an angle of attack (AoA) range from -5° to +25°. This module also supports the import of polar data, including experimental results, requiring that the airfoil be named identically to the imported data for accurate linkage.

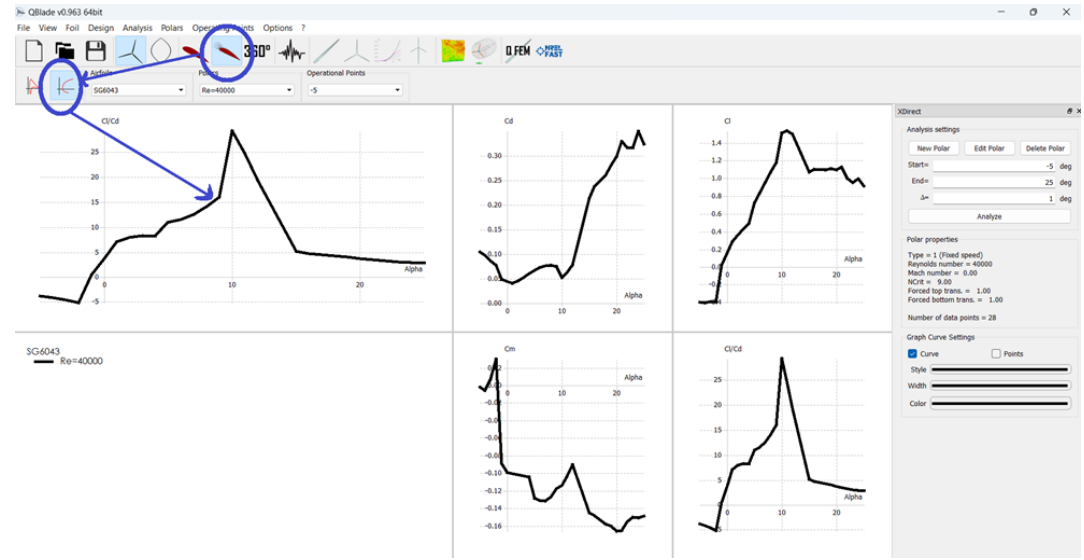


Figure III-17: XFOIL interface

III.4.2.2.2 Key Features of XFOIL Relevant to Qblade

XFOIL provides critical features for Qblade, including:

- Viscous and Inviscid Analysis: Evaluates airfoil performance in various flow conditions.
- Transition and Separation Modeling: Simulates forced and free transitions, and trailing edge separation.
- Lift and Drag Predictions: Accurate predictions, including post-stall behavior.
- Design and Redesign Tools: Facilitates airfoil design through surface velocity distribution and interactive parameters.
- Airfoil Blending and Import: Supports blending of airfoils and importing geometries for analysis.

Figure III-18 illustrates the pressure distribution on the blade surface, demonstrating XFOIL capability to visualize aerodynamic effects.

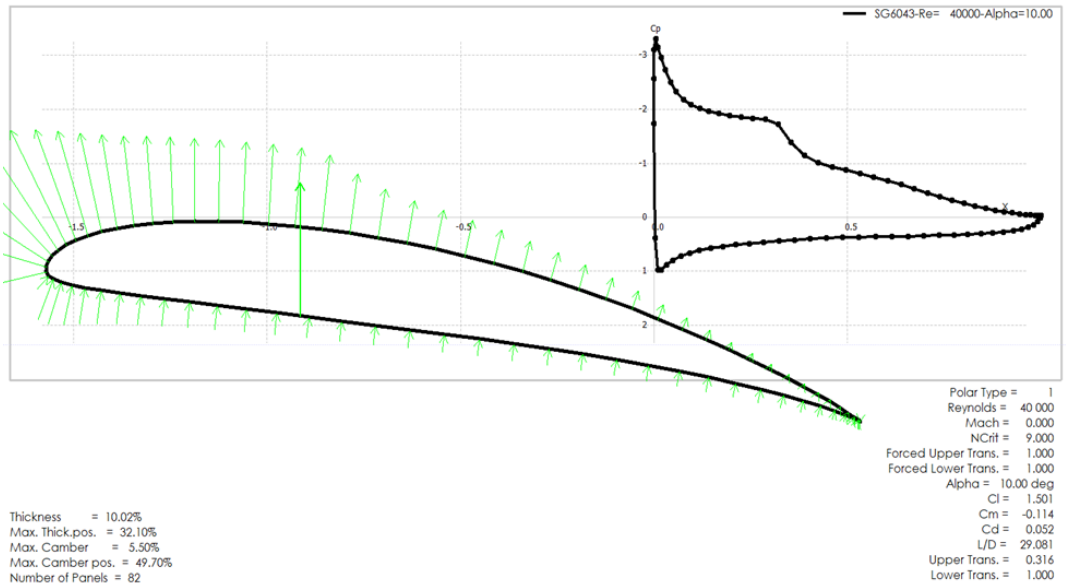


Figure III-18: Pressure Distribution on Airfoil Surface at design angle of attack

III.4.3 360° Extrapolation module

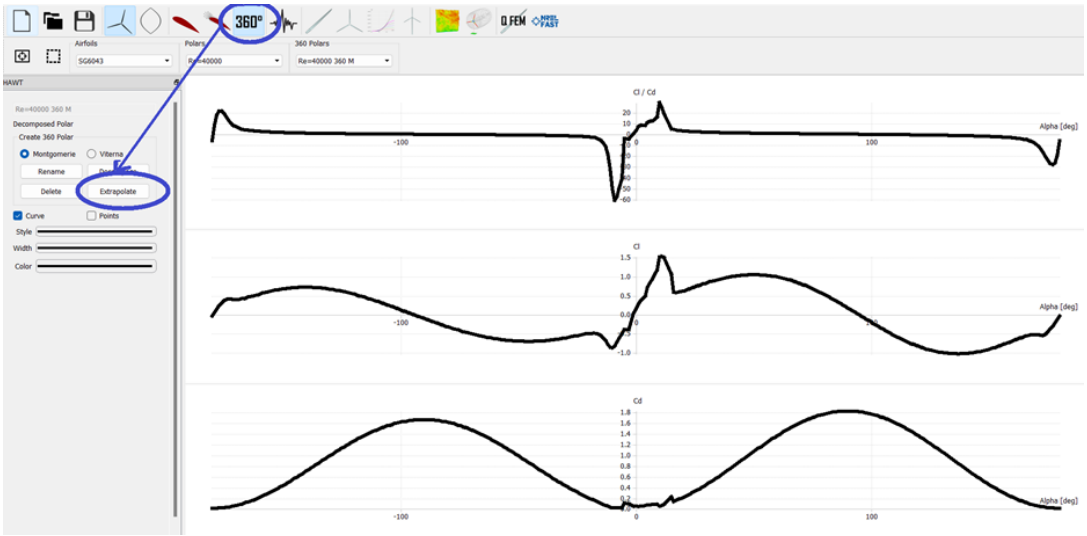


Figure III-19: Extended Polar Data for SG 6043 Airfoil at Re=40000

The 360° extrapolation module in Qblade significantly enhances aerodynamic data coverage by extending it across the full range of angles of attack (AoA) that wind turbine blades may encounter, which often exceed those typically addressed in aeronautical engineering. This module ensures precise performance modeling by employing advanced extrapolation techniques, such as Montgomery method and the Viterna-Corrigan post-stall model [53], to project lift and drag coefficients beyond standard experimental data. Consequently, it supports comprehensive analysis and accurate simulation of wind turbine behavior under various operating conditions, including extreme scenarios.

Figure III-19 illustrates the extended polar data for drag and lift coefficients of the SG 6043 airfoil, achieved through 360-degree extrapolation. This integration allows Qblade to provide more reliable and detailed performance predictions for wind turbines.

This tool complements the results of both XFOIL and 360 interpolations, providing a robust design and analysis methodology for a HAWT under various operating conditions. It utilizes a multi-submodule scheme to achieve comprehensive and accurate results.

III.4.3.1 Blade Design Submodule with Schmitz Optimization Method

The blade design module in Qblade allows users to model and optimize rotor blades by specifying various parameters such as position, chord length, twist angle, airfoil type, and 360° polar data. This module supports the creation of detailed blade geometries and the incorporation of advanced corrections for accurate performance simulations. Figure III-20 illustrates the optimized chord length and twist angle from root to tip, enhancing aerodynamic performance and energy absorption. Following the Schmitz method, both chord length $C(r)$ and twist angle $\beta(r)$ decrease from root to tip to improve efficiency and load distribution.

The relevant equations are:

$$c(r) = \frac{16\pi r}{BC_L} sin^2\left(\frac{1}{3} tan^{-1}\left(\frac{R}{\lambda_0 r}\right)\right) \quad \textbf{(III.49)}$$

$$a = \phi - \beta \quad \textbf{(III.50)}$$

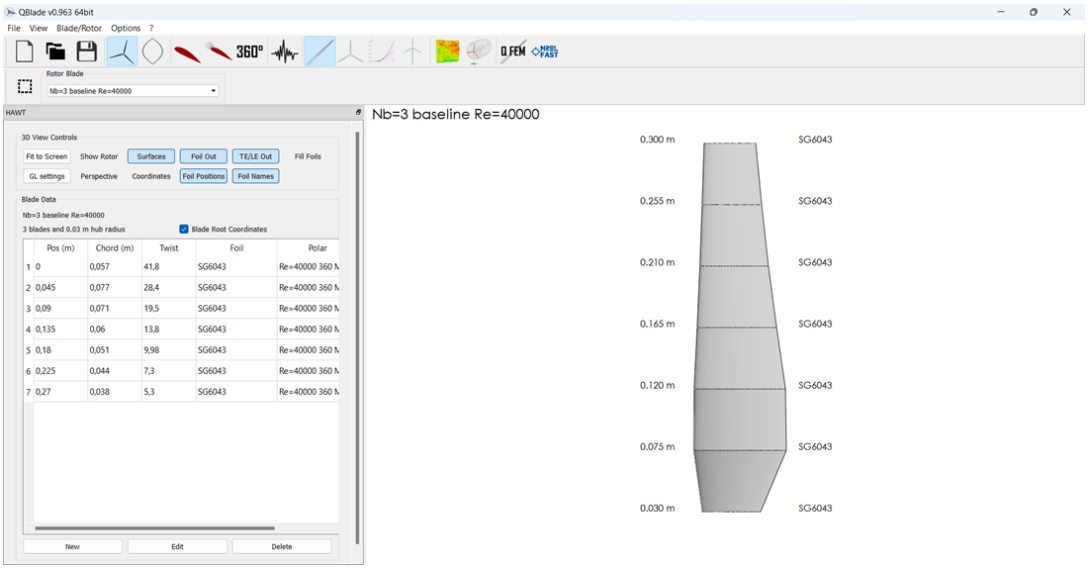


Figure III-20: shows the 3D view of blade with both chord and twist distributions.

III.4.3.2 Rotor Simulation Submodule

The rotor simulation submodule allows users to simulate rotor blades over various tip-speed ratios. A simulation can only be initiated if at least one rotor blade exists in the runtime database. Users need to choose the appropriate corrections to the BEM algorithm and set the simulation parameters. After defining the simulation, users can specify a range of TSR-values (tip-speed ratios) and the incremental steps. Figure III-21 shows the rotor simulation submodule.

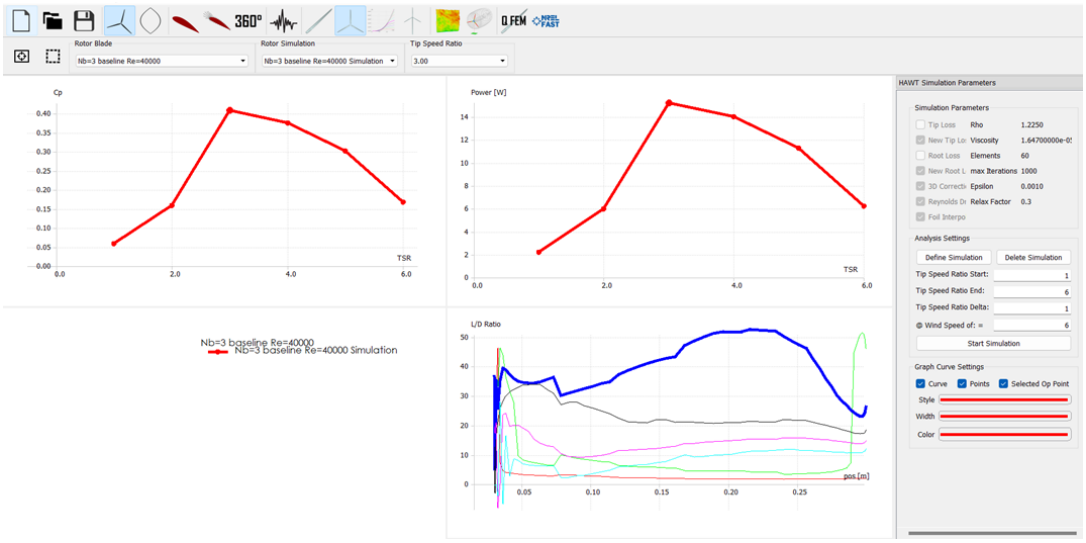


Figure III-21: The rotor simulation submodule at Re=40000

III.4.3.3 Multi-Parameter Simulation Submodule

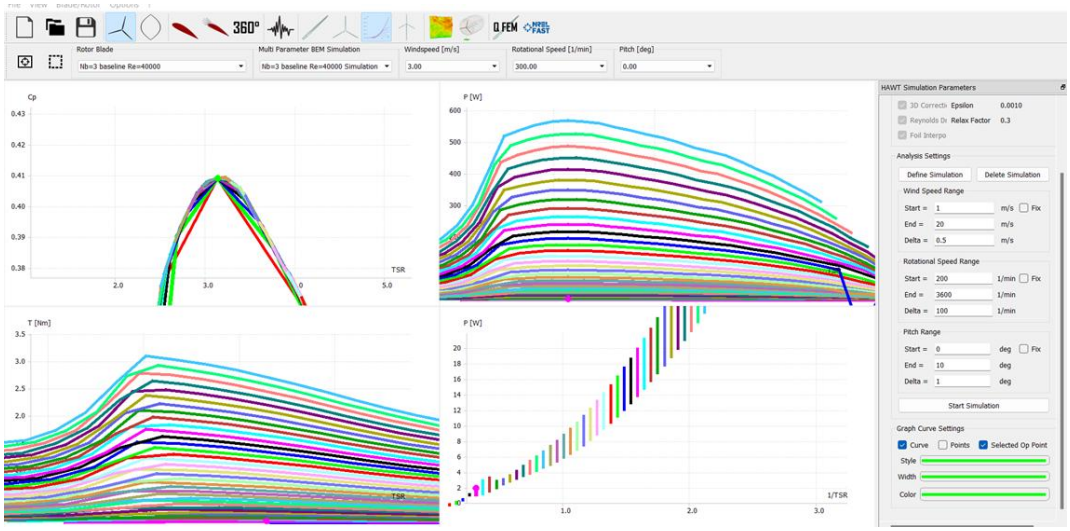


Figure III-22: The multi-parameter simulation submodule at Re=40000.

The multi-parameter simulation module allows users to conduct simulations across a range of wind speeds, rotational speeds, and pitch angles. To conserve memory, only the rotor graph curves are stored. Users can right-click on

a graph to set the chosen variables and update the curve series accordingly. Adjustments made to wind speed, rotational speed, or pitch angle via the toolbar will dynamically refresh the graphs. This module is crucial for developing control strategies for variable-speed and pitch-controlled wind turbine rotors. Figure III-22 illustrates the multi-parameter simulation submodule.

III.5 TURBINE DEFINITION AND SIMULATION SUBMODULE

In this submodule, users define and simulate wind turbines by specifying the turbine type—pitch or stall regulation—and transmission type—single-speed, 2-step, or variable. For pitch-regulated turbines, a nominal power output is set, with blades pitched to maintain this output at higher wind speeds. Stall-regulated turbines limit power only when a stall occurs, requiring an iterative design approach. Transmission options range from fixed single-speed to variable, where users set rotational speed bounds and a desired tip-speed ratio. Essential parameters include Vcut-in and Vcut-out wind speeds of the rotor blade, and fixed and variable losses. Figure III-23 shows the turbine definition and simulation submodule.

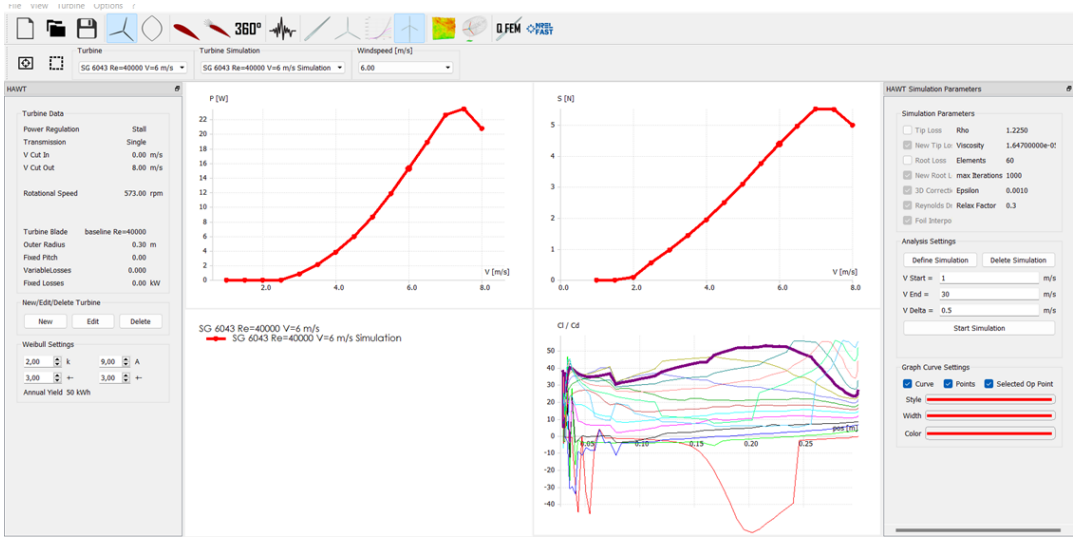


Figure III-23: The turbine definition and simulation submodule at Re=40000

III.6 ADVANCED BEM THEORY IN QBLADE WITH CORRECTIONS

Qblade utilizes Blade Element Momentum (BEM) theory for accurate rotor performance prediction. BEM theory combines blade element theory with

momentum theory to predict forces on each blade section, accounting for variations in wind speed and blade geometry. Qblade enhances this with advanced corrections such as tip loss, hub loss, and dynamic stall models, providing more precise and realistic simulations. Figure III-24 illustrates the all-correction types using in Qblade software. The current thesis encompasses all types of corrections; therefore, a specific and distinct approach must be formulated for each type of correction.

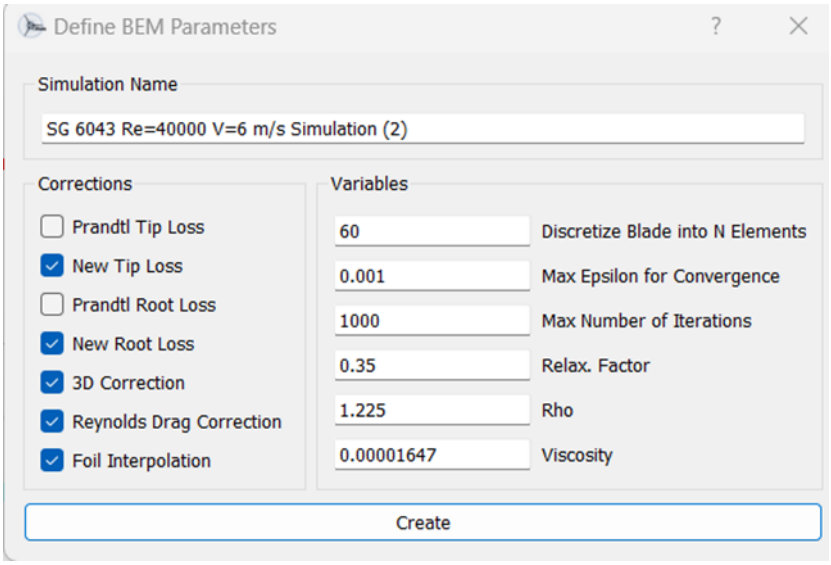


Figure III-24: Comprehensive correction features integrate into Qblade

III.6.1 Prandtl tip- and root loss

Tip losses at the blade extremity significantly affect overall performance, primarily due to pressure differentials between the airfoil upper and lower surfaces. This pressure difference causes air to flow from high to low-pressure areas, generating a vortex at the blade tip that dissipates into the wake, thereby reducing power output. In Blade Element Momentum (BEM) theory, various methods address these losses, with the Prandtl method being the most widely used [54]. It introduces a tip-loss correction factor that depends on variables such as wind angle, number of blades, and blade position. This factor clarifies the diminishing aerodynamic forces along the blade, except the tip region. Figure III-25 depicts the tip loss factor for a radial blade, ranging from 0 to 1. From the root to approximately 85% of the blade radius, the factor remains constant at 1, but it declines sharply near the tip. This decline corresponds to an increase in the induction factor, which reduces relative wind speed and angle of attack, ultimately leading to lower lift and drag forces.

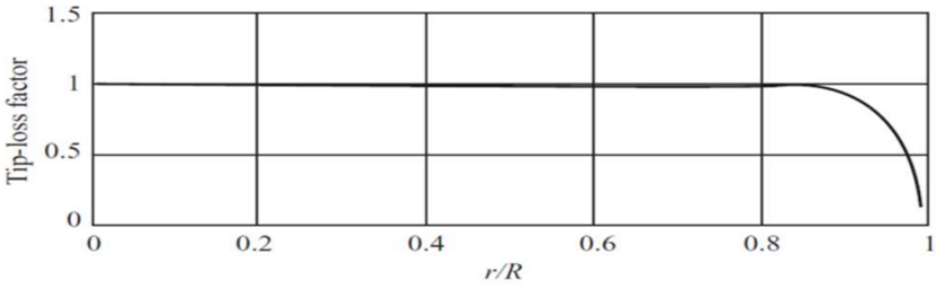


Figure III-25: Span variation of the tip loss factor of a wind turbine blade [8]

The tip loss correction factor, originally developed by Ludwig Prandtl, is commonly expressed as:

$$F_{tip} = \left(\frac{2}{\pi}\right) cos^{-1}\left[e^{\frac{B(R-r)}{2r\,sin\,\phi}}\right] \quad \textbf{(III.51)}$$

Concerning the hub loss correction, it is written as:

$$F_{hub} = \left(\frac{2}{\pi}\right) cos^{-1}\left[e^{\frac{B(1-\mu r)}{2\mu\,sin\,\phi}}\right] \quad \textbf{(III.52)}$$

the blade loss correction is formulated as:

$$F = F_{tip} \times F_{hub} \quad \textbf{(III.53)}$$

Where local radius;

$$\mu = \frac{r}{R}$$

The blade loss correction factor F ranges from 0 to 1, quantifying the reduction in aerodynamic forces experienced at a radius r along the blade due to tip and hub losses. This factor effectively accounts for the diminished performance resulting from the aerodynamic phenomena occurring at the blade extremities.

III.6.2 New tip- and root losses after Shen

Assuming constant wind velocity in the rotor plane inadequately captures real wind variations and vortex-induced energy losses at the blade root and tip. Additionally, rotor rotation and centrifugal effects distort velocity distribution and pressure gradients, leading to momentum balance errors when blades deviate from the rotor plane. Qblade addresses these issues with several correction algorithms, including Prandtl's and Shen's models, SNEL's 3D correction, and Reynolds number adjustments. However, Shen's models are incompatible with Prandtl's due to overlapping correction factors. This thesis focuses on applying Shen loss model at tip and root for flow correction. In 2005, Shen evaluated tip loss models by Prandtl [55], identifying inconsistencies near the blade tip where the tip loss factor F approaches zero, causing inaccuracies in axial velocity and angle of attack. He also noted that Prandtl model overestimates tip loads compared to experimental

data. To resolve these issues, Shen introduced a new tip loss model with a correction term for force coefficients C_n and C_t.

III.6.3 3D correction after Snel

Himmerlskamp had proved that an airfoil with rotating blades mounted on, had a higher lift coefficient in comparison to the stationary blade profile. Hence, centrifugal force makes the boundary layer thinner, delaying stall; while radial airflow generates a Coriolis force, that further postpones stall.

The so-called Himmelskamp effect implies that 2D airfoil data should be corrected by shifting the stall region toward higher angles of attack [56]. used a Viscous Inviscid Interaction Method to develop a semi-empirical correction for lift coefficients based on these effects, noting that drag coefficients remain unchanged.

III.6.4 Reynolds number drag correction

Qblade does not account for the effects of Reynolds number on lift and drag polars; these polars are computed for a fixed Reynolds number. However, during turbine simulations, the Reynolds number varies with each operational point, necessitating careful examination of deviations for each specific case. A correction method was proposed in [57], where the lift polar remains constant while the drag polar is adjusted by scaling the drag coefficient inversely with the Reynolds number. The correction formula is given by:

$$C_D = C_{D,Ref}\left(\frac{Re_{Ref}}{Re}\right)^{0,2} \quad \textbf{(III.54)}$$

Re_{Ref} denotes the Reynolds number for which the polar data was originally calculated. This correction method, though straightforward, may oversimplify the estimation of the drag coefficient, particularly for low Reynolds numbers where drag behavior can be intricate and complex.

III.6.5 Foil interpolation

Foil interpolation provides a straightforward solution to a discretization issue in blade modeling, rather than acting as a correction to the Blade Element Momentum (BEM) algorithm. Each blade section has a distinct airfoil that defines its geometry, and the geometry between sections is determined by linear interpolation of these airfoils. The problem arises because polar data is only

available for the airfoils at each section, not for the interpolated airfoils between sections.

Without foil interpolation, the BEM algorithm processes the blade as shown in Fig. III-26. In blade modeling, elements centered between sections 1 and 2 are assigned the polar data from foil 1. Importantly, the final airfoil at position Z is excluded from the simulation. A discontinuity occurs between the element just before section 2 and the one immediately after, as the airfoil data abruptly shifts from foil 1 to foil 2, impacting simulation results if interpolation is not applied.

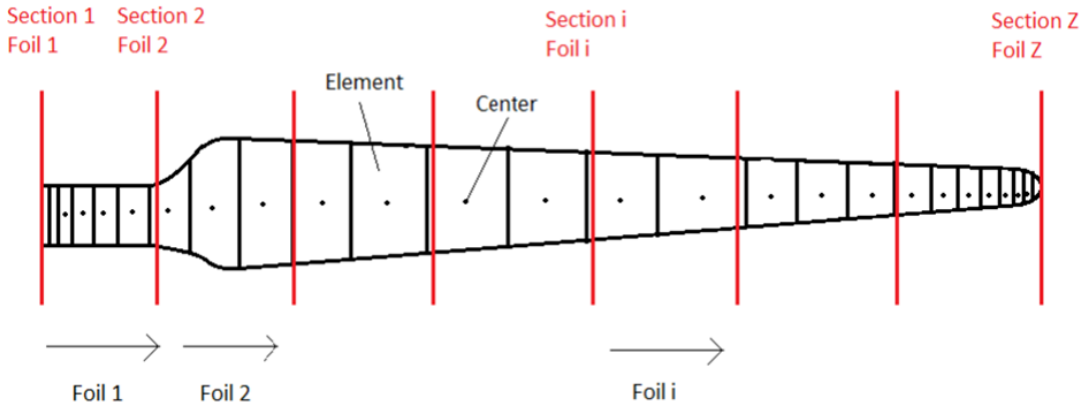


Figure III-26: Foil distribution along the blade without interpolation [58]

When foil interpolation is enabled, the polar data used for BEM computation of an element is a linear interpolation between the polar data of the bounding airfoils, providing a more accurate representation of the blade geometry. However, this linear interpolation is only an approximation and does not accurately represent the true polar of the intermediate airfoil, which is missing from the database. Accuracy can be improved by importing geometric data for these intermediate airfoils and creating new sections, or by using XFOIL's dynamic coordinate mixing function to generate and simulate intermediate airfoil geometries [58].

CONCLUSION

In this chapter of the thesis, we elucidate the fundamental aerodynamic principles to understand the physical phenomena associated with the operation of the micro-turbine. Additionally, we present a methodological framework based principally on BEM approach for designing and evaluating turbine performance used in the advanced open-source software Qblade. Subsequently, the selection of optimal geometric parameters will be explored in depth through a comprehensive parametric study in the following chapter.

IV. Chapiter IV: Parametric Analysis of Geometry Design for High-Efficiency HAWT

INTRODUCTION

This chapter systematically investigates the selection of critical geometric parameters for optimized design with high-efficiency rotor at various conditions. It offers a thorough analysis of several key factors, including profile type, design tip speed ratio (TSR-d), number of blades (NB), hub-to-tip ratio (Hrt), and Reynolds number (Re). Furthermore, the chapter employs Qblade software, utilizing its sophisticated tools to enable precise and rapid evaluation of all potential configurations addressed within this analysis. This chapter further explores the suitable mathematical functions for characterizing both chord length and twist angle distributions along the blade which lead to select the optimal turbine configuration. A variety of fitting functions will be examined to identify the most effective representation, which will be used subsequently in optimization process.

IV.1 FLOWCHART FOR THE DESIGN AND ANALYSIS OF MICRO HAWT UTILIZING QBLADE SOFTWARE

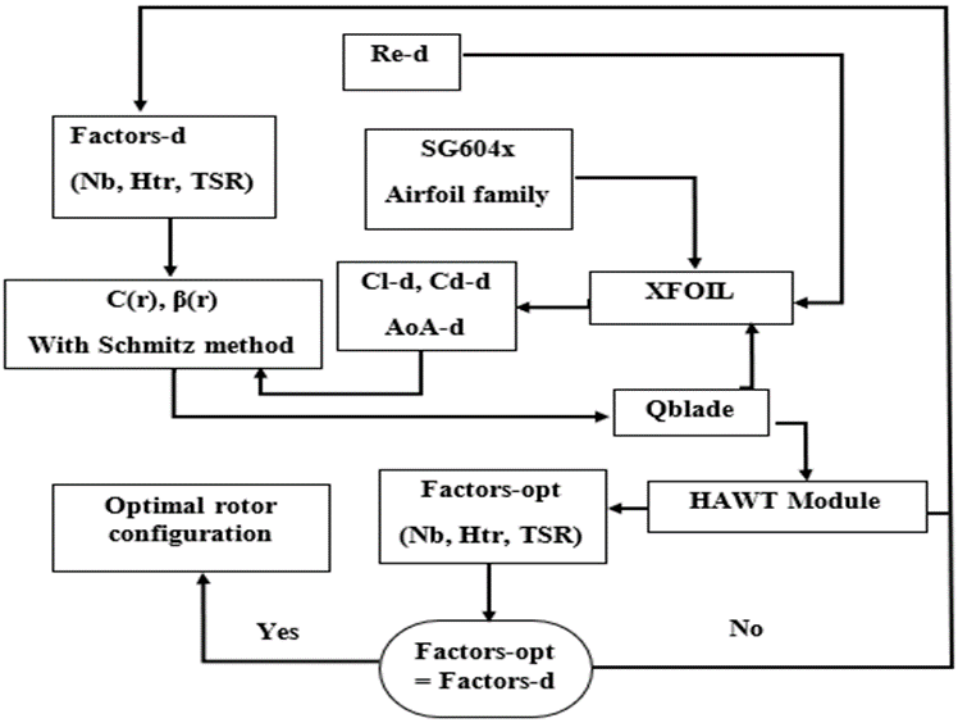


Figure IV-1: Flowchart for the Design and Analysis of micro HAWT.

This section presents the sequential methodology for designing and analyzing the performance of a micro horizontal axis wind turbine (HAWT), illustrated through a flowchart. Initially, the lift coefficient (Cl), drag coefficient (Cd), and angle of attack (AoA) are determined for design condition, with suitable Reynolds number and airfoil type using Xfoil software. Subsequently, the Schmitz method is employed to calculate the chord and twist distribution along the blade. Following this, a three-dimensional rotor blade is designed based on the established chord and twist profiles. The curve of power coefficient (Cp) in terms of the tip speed ratio (TSR) is then extracted to assess rotor performance and identify the optimal TSR. This parametric study is performed in order to identify the optimal geometric parameters leading to a best rotor at all operating conditions. Figure IV-1 illustrates the comprehensive steps undertaken to achieve the optimal design.

IV.2 CHOOSING THE BEST AIRFOIL PROFILE

This section focuses on the optimal selection of airfoils by evaluating the performance of the different types owning to SG604x family (SG6040, SG6041, SG6042, and SG6043 airfoils). The maximum chord length, (Cmax=0.1 m), was utilized to determine the Reynolds number for all studied cases. Three distinct Reynolds number values, $Re = 20000$, $Re = 40000$, and $Re = 55000$, were obtained, corresponding to velocities $V = 3\,m/s$, $V = 6\,m/s$, and, $V = 8\,m/s$, respectively. These values were calculated using the following relationship:

$$Re = \frac{\rho V C_{max}}{\mu} \qquad \textbf{(IV.1)}$$

where ρ represents the fluid density, V is the flow velocity, Cmax is the maximum chord length, and μ is the dynamic viscosity of the fluid

Figure IV 2 illustrates the different shapes of the SG604x airfoils family as modeled in the Qblade interface. The geometric characteristics of the SG604x airfoil sections reveal a constant maximum thickness across the profiles, with only minor differences in chordwise positioning between them. Seemingly, the SG6040 stands out, exhibiting a maximum thickness that surpasses the other airfoil configurations table IV-1.

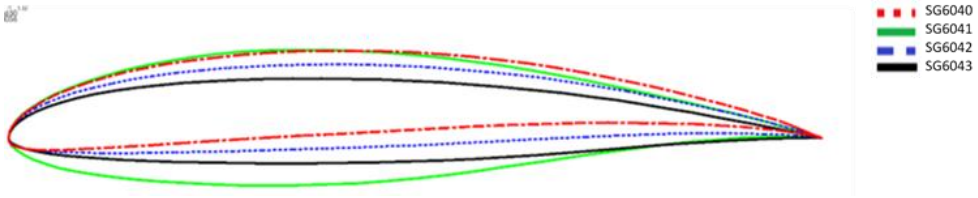


Figure IV-2: The different shapes of the SG604x airfoils family.

Tableau IV-1: Geometric properties of SG604x airfoils family.

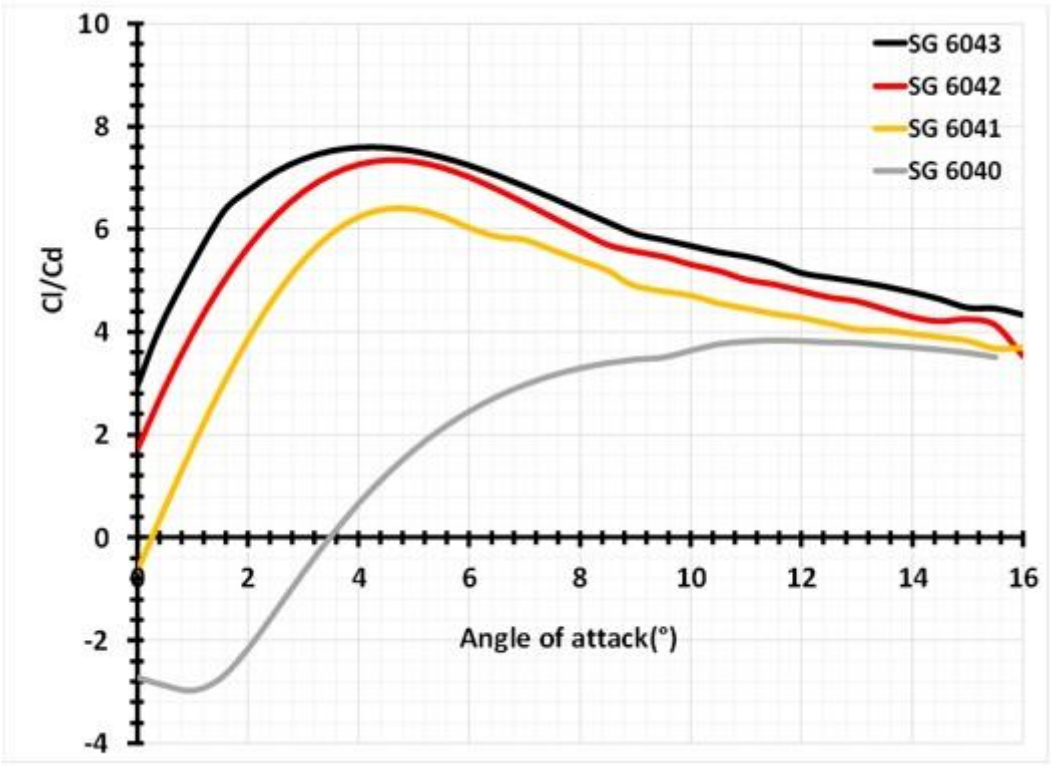
SG604x profile type	Max thickness %	Maximum thickness position%
SG6040	16	35.3
SG6041	10	34.9
SG6042	10	33.5
SG6043	10	32.1

Tableau IV-2 Aerodynamic performance of the SG604x airfoil family at Re=40000.

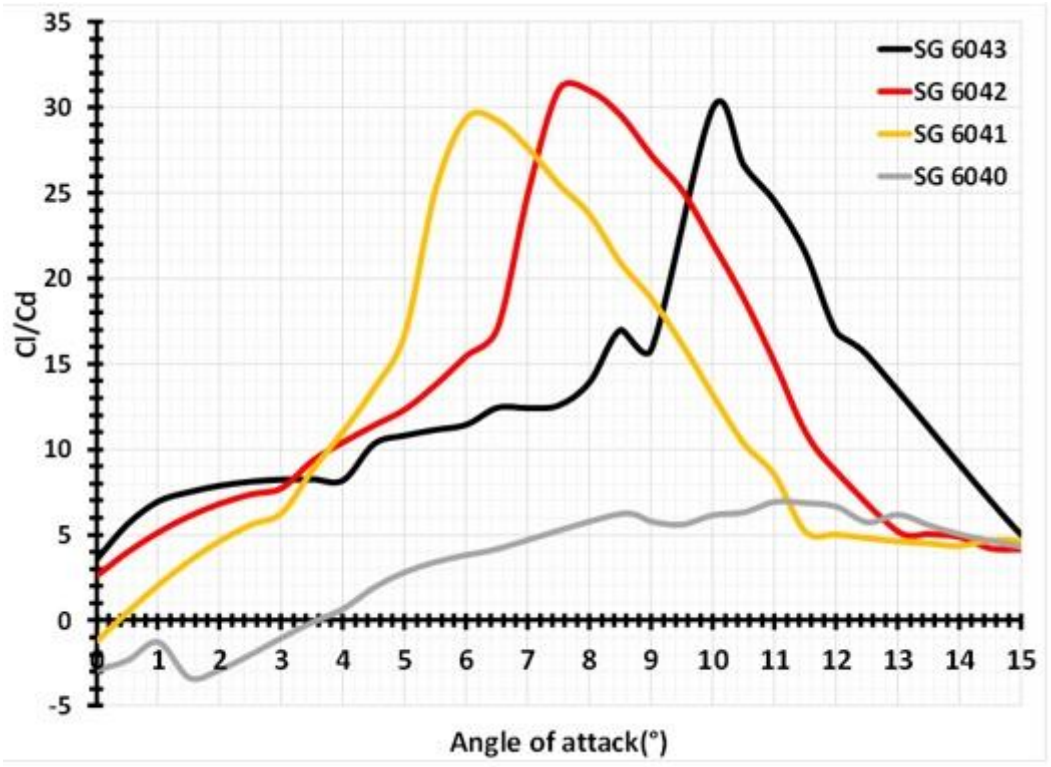
SG604x Types / Factors	SG 6040	SG 6041	SG 6042	SG 6043
Max C_l/C_d	7	30	31.5	30
Optimal AoA	11	6	8	10

The aerodynamic performance of the SG6043 airfoil demonstrates exceptional superiority under varying Reynolds numbers compared to other airfoils, as illustrated in Figures IV-3b and 3c. Specifically, when the Reynolds number deviates from the design value of Re = 40000, the SG6043 achieves the highest glide ratio (C_l/C_d), reaching a peak value of 62.2 at Re = 55000 and 7.8 at Re = 20000. Furthermore, at Re = 55000, a noticeable reduction in the optimal angle of attack is observed across all sections relative to Re = 40000. This behavior underscores the adaptability of the SG6043 airfoil to variations in operational conditions. The ability of the SG6043 to sustain its aerodynamic efficiency across different Reynolds numbers, coupled with its consistent performance at high angles of attack, positions it as a robust and reliable candidate under diverse operating scenarios, surpassing the stability and effectiveness of other tested airfoils.

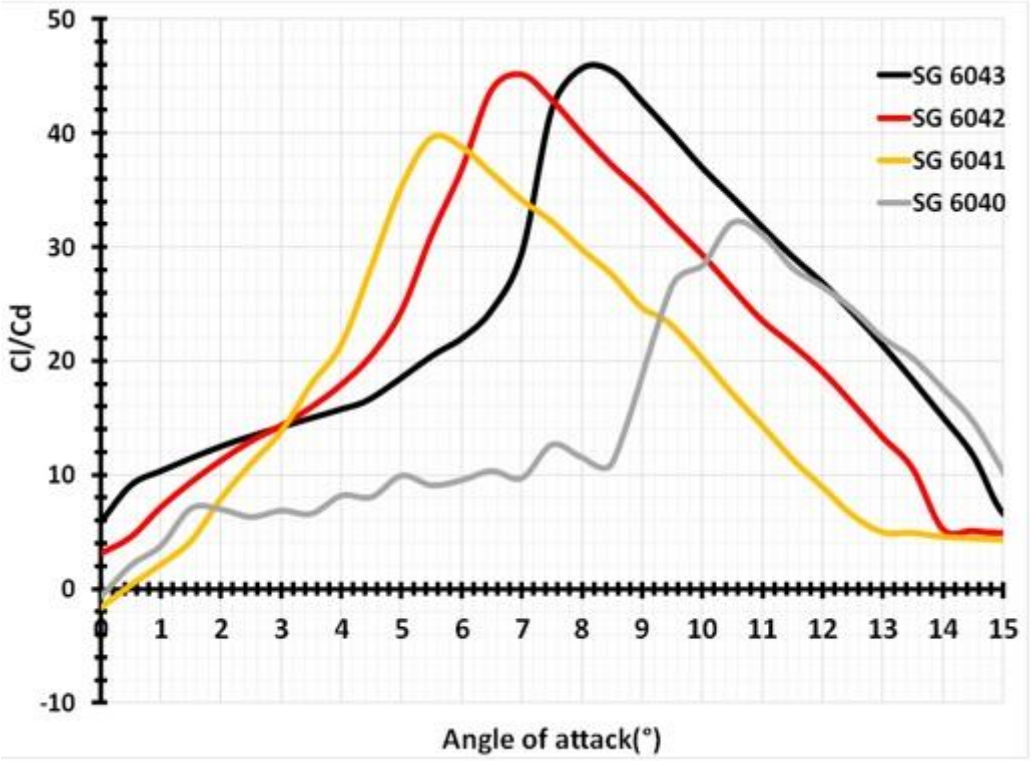
At Re = 40000, the glide ratios for all airfoils converge at their optimal angles of attack, exhibiting C_l/C_d values around 30, except the SG6040; it marks the lowest value of C_l/C_d. Notably, the SG6042 profile demonstrates an improvement in performance with approximately 5.5 % compared to the other two performant airfoils. The studied profiles SG6043, SG6042, SG6041, SG6040 achieves their optimal angles of attack at 10°,8°,6° and 11° respectively, under these conditions (see Tableau IV-2).


SG 6043
SG 6042
SG 6041
SG 6040
Cl/Cd
Angle of attack(°)
10
8
6
4
2
0
-2
-4
0
2
4
6
8
10
12
14
16

(a)


SG 6043
SG 6042
SG 6041
SG 6040
Cl/Cd
Angle of attack(°)
35
30
25
20
15
10
5
0
-5
0
1
2
3
4
5
6
7
8
9
10
11
12
13
14
15

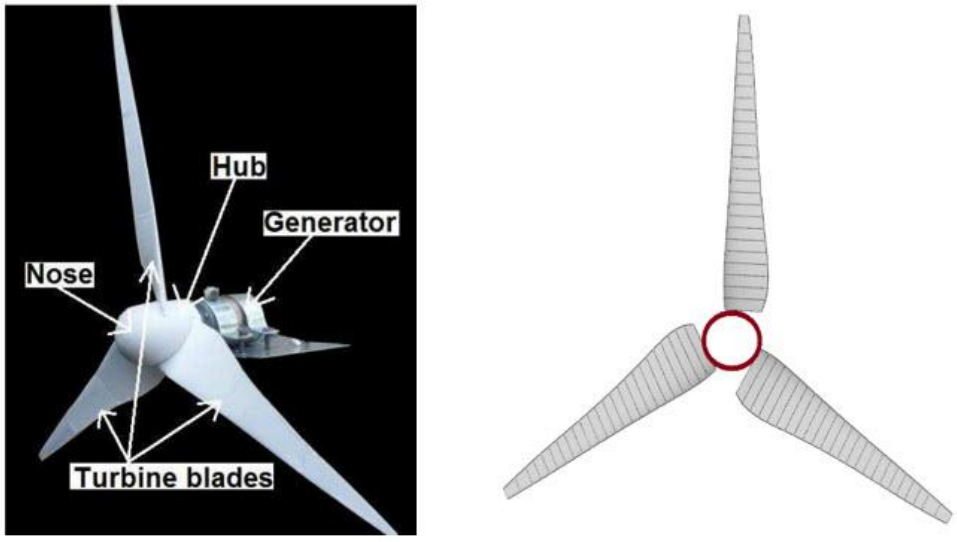
(b)



(c)

Figure IV-3 : The performance of SG 604x family at Reynolds number a) Re=20000, b) Re=40000, c) Re=55000

IV.3 QBLADE MODEL VALIDATION



(a) (b)

Figure IV-4: 3D views comparison between (a) Experimental rotor, (b) Simulated rotor

This section evaluates the accuracy of the numerical approach via Qblade software by comparing its results with experimental data [59] through three distinct

flow condition scenarios. Table IV-3 presents all geometric factors for the experimental setup used in this validation. Additionally, Figure IV-4 provides 3D rotor views for both experience and Qblade simulation.

Tableau IV-3 : Illustrates the experimental rotor factors

Factor	Value
Design TSR	5
Design wind speed	6 m/s
Hub tip ratio	10%
Number of blades	3
Type airfoil	Naca 4412
Blade radius	0.35 m
Reynolds number	100000

The implemented modifications include three-dimensional corrections, Reynolds drag corrections, and foil interpolation, applied in all case studies. Figure IV-5 demonstrates that the application of both new tip loss and root loss corrections significantly enhances the agreement between simulated results and experimental data, particularly within the focused range of tip speed ratios (TSR) from 4.2 to 7. In contrast, scenarios that do not incorporate these corrections show a less favorable alignment with experimental results. Moreover, peak performance consistently occurs at an optimal TSR of 5 across all examined cases. A comparative analysis indicates that the integration of new root and tip loss corrections yields more accurate and reliable results than alternative methods. Specifically, rotor performance at TSR values varied from 4.25 to 7 match experimental data in acceptable way, while at a TSR of 9, the results align most closely with the experience when employing the new corrections, as opposed to Prandtl corrections or scenarios lacking tip and root loss corrections. It is also noted that at both low and high TSRs, the results of numerical simulations with all corrections still do not fully align with experimental results, likely due to boundary layer separation phenomena that cannot be adequately captured by the Blade Element Momentum (BEM) method.

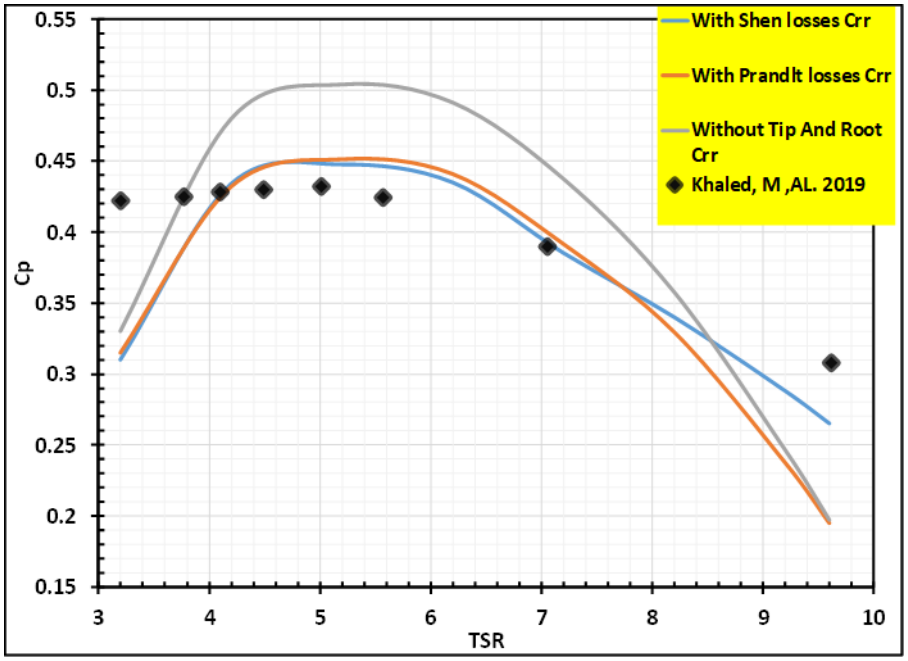


Figure IV-5: Validation of the numerical approach with experimental data

Overall, the case utilizing the new tip and root loss corrections demonstrates the highest fidelity to experimental results, rendering this method the most reliable for assessing performance under various conditions in this thesis.

IV.4 BLADES NUMBER AND TIP SPEED RATIO EFFECT

In this section, the optimal tip speed ratio (TSR) will be identified by analyzing turbine performance under varying operational conditions, following the selection of the SG6043 airfoil within TSR range from 1 to 5, utilizing the Schmitz method. This analysis incorporates various correction factors, including new tip and root losses, at wind velocity of V = 6 m/s and Reynolds number of Re = 40,000, with a tip-to-root ratio (r/R) of 10%. Additionally, an overview of performance variations will be provided by adjusting the number of turbine blades from 1 to 5, reflecting the operational efficiency of the turbine at minimal costs.

Based on the analysis presented in Figure IV-6, under both ranges TSR=3-5 and Nb =3-5 the configurations exhibit approximatly with comparable performance levels, Cp=0.407-0.42.

In other hand, the two configurations at TSR = 1 and 2 show relatively low performance, with power coefficient (Cp) values of 0.27 and 0.36, respectively, when compared to the performance of the three-blades configuration and other TSR values. Furthermore, an examination of the four-blades and five-blades configurations at TSR = 3 reveals performance enhancements of approximately 2.8% and 3.7%, respectively, compared to three bladed one. However, the marginal

performance gains associated with these additional blades are accompanied by increased costs. Therefore, the configuration of NB = 3 at TSR = 3 emerges as the most efficient option for achieving optimal turbine performance while ensuring cost-effectiveness.

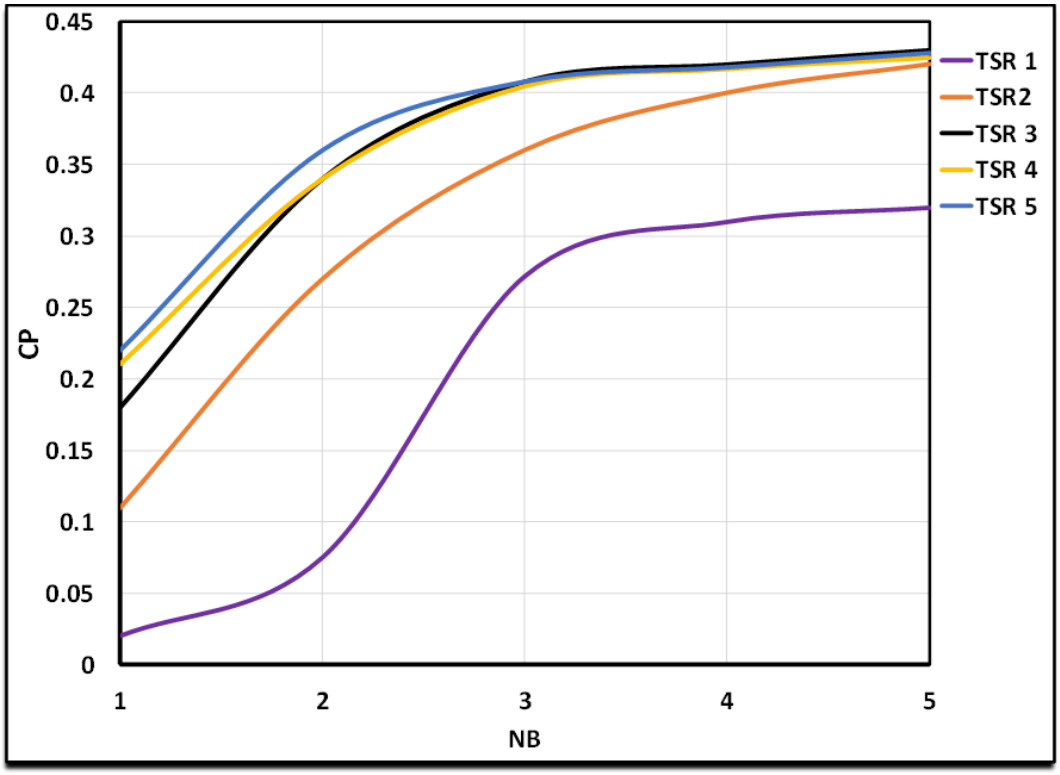


Figure IV-6: Effect of both tip speed ratio and blade number on the micro HAWT performance

This analysis provides a comprehensive examination of the optimal selection of blade number in conjunction with the appropriate tip speed ratio (TSR). It is determined that a TSR of 3 with three blades is suitable for implementation in all subsequent analyses within this chapter.

IV.5 HUB -TO-TIP RATIO EFFECT

Following the selection of a three-blade configuration NB = 3, a tip speed ratio TSR= 3 and a wind velocity V =6 m/s at Re=40000, the Qblade simulations were conducted under theses parameters. The incorporation of all corrections discussed in the previous section is considered in this study. This section emphasizes the establishment of a hub to tip ratio that ensures the solidity value remains below 1 in particular at the root region, serving as a critical constraint within the design process. This parameter is essential for maintaining structural integrity and performance throughout the operational range of the system.

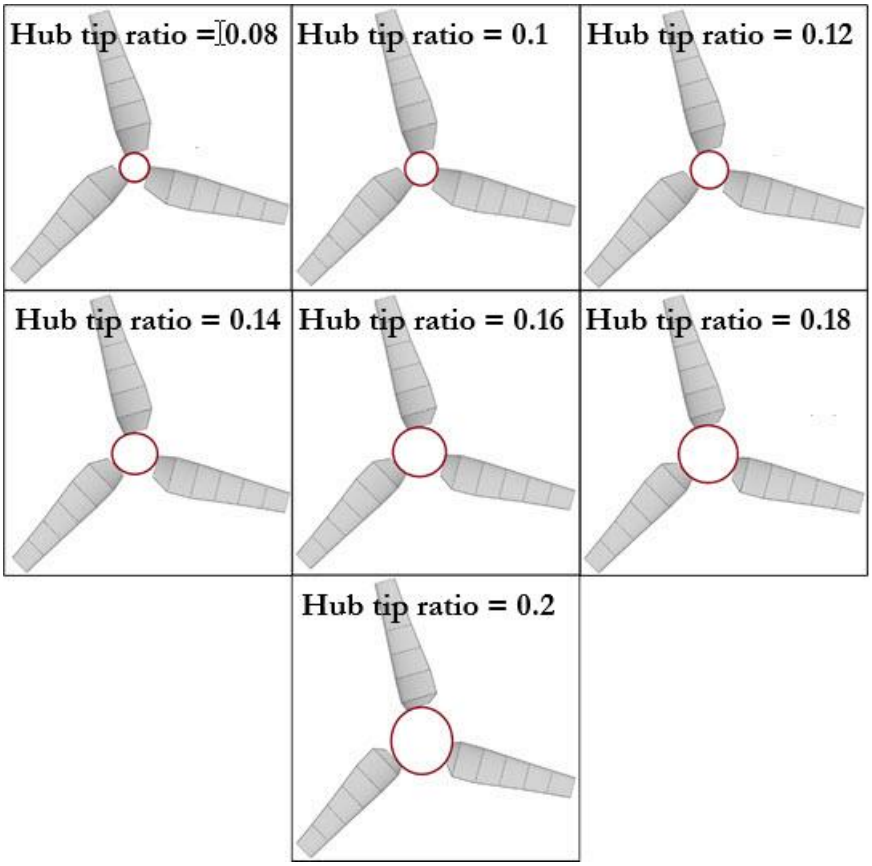


Figure IV-7: 3D view of HAWT from hub tip ratio 0.08 to 0.2

This part investigates the effect of varying the root-to-tip ratio Htr within the range of 8% to 20%. As illustrated in Figure IV-7,8 the optimal performance was achieved at Htr = 0.1, beyond this value, as and when the root-to-tip ratio increases the performance decreases. These results indicate the existence of a critical root-to-tip ratio that maximizes turbine efficiency. Furthermore, when the root-to-tip ratio falls below 8%, the constraint imposed by turbine solidity prevent any further reductions. Conversely, ratios exceeding 10% lead to an expansion of the root area, which can decrease the cross-sectional flow and subsequently result in diminished performance.

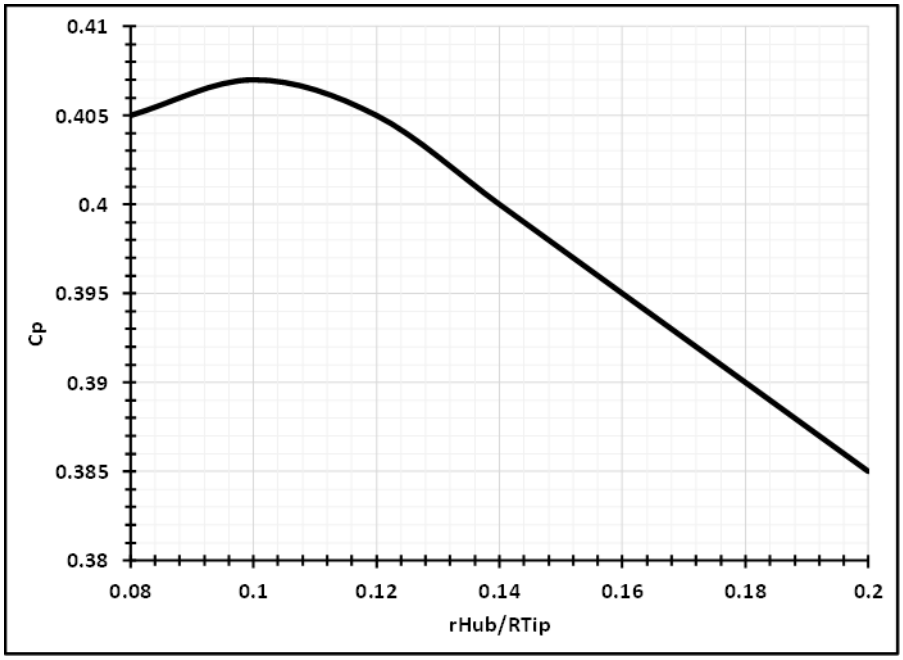


Figure IV-8: Effect Hub tip ratio on the turbine performance.

IV.6 REYNOLDS NUMBER EFFECT

This section examines the impact of Reynolds number on the performance of four rotor configurations utilizing SG604x profiles destined for small turbines.

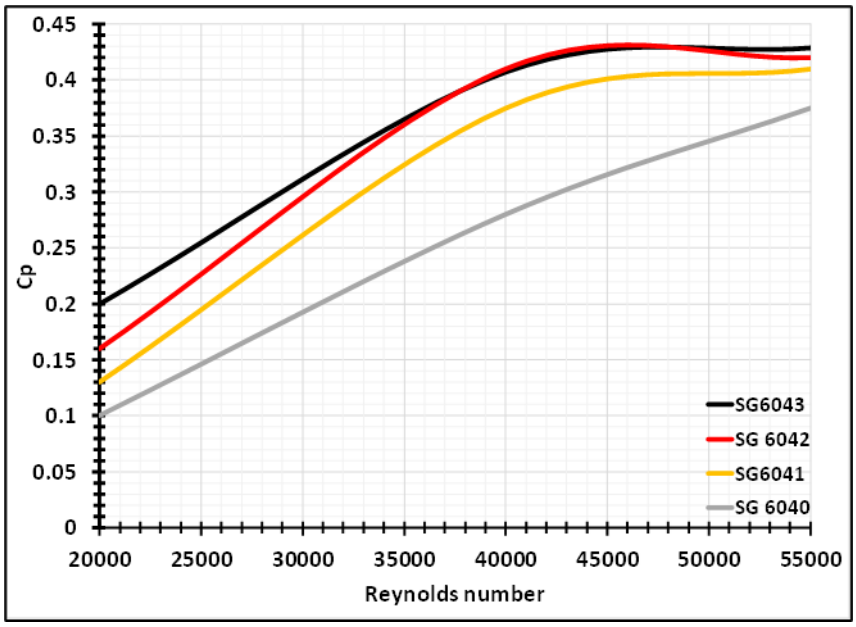


Figure IV-9: Effect Reynolds number on the turbine performance.

The performance of the turbines demonstrates a notable improvement as the Reynolds number increases from 20,000 to 55,000 across all tested

configurations. Among the examined rotors, the SG 6040 consistently exhibits inferior performance under all operating conditions, highlighting its limitations. In contrast, the SG 6042 rotor achieves a marginally higher performance compared to the SG 6043, with an observed 3.5% advantage at a Reynolds number of Re=40000. However, the SG 6043 rotor emerges as the most efficient configuration, showcasing superior performance under varying Reynolds numbers. This makes it a promising candidate for high-efficiency rotor design. Notably, these findings align well with the results obtained from two-dimensional XFoil analyses, further validating the aerodynamic behavior of the rotors Figure IV-9.

IV.7 POWER TURBINE ANALYSIS OVER OPERATING RANGE

The table below presents a comprehensive summary of the optimal geometric conditions and factors employed in this thesis, as identified through the precedent analysis. The designed rotor with the SG6043 airfoil exhibits high aerodynamic performance for all Reynolds number cases (see Table IV-4). To further evaluate the turbine output power and self-starting capability, the tip speed ratio (TSR) is fixed at 3 while varying the wind velocity. Consequently, the power curves for all turbine types are plotted. Initially, the cut-in speed is established at zero, which allows for precise monitoring of the actual starting values for each turbine. Additionally, power output is assessed within a wind speed less or equal 7 m/s, corresponding to the operational parameters typical of low-speed turbines.

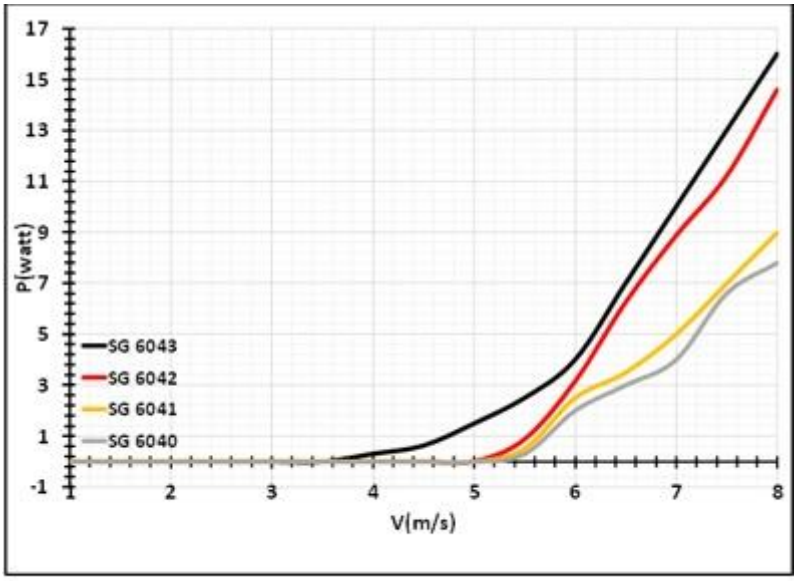
Table IV-4: Selection of design parameters for optimal performance

Parameters	Optimum Parameters
Airfoil	SG6043
Re	40000
NB	3
Htr	10%
TSR	3

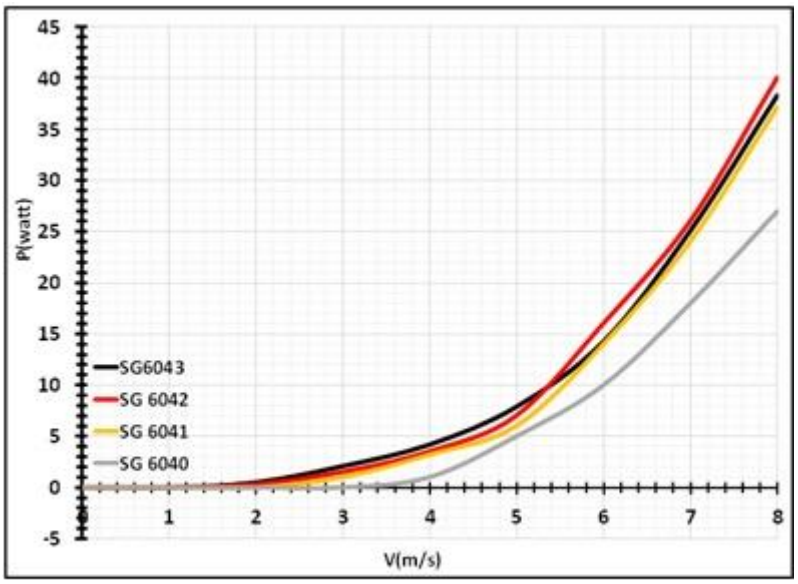
Figure IV-10 clearly demonstrates that the SG 6043 turbine model exhibits superior self-starting capability across all Reynolds numbers compared to other turbine designs. The data indicates that increasing the Reynolds number enhances the power output of all turbines. However, at a Reynolds number of 20000, there is a notable deterioration in performance for all rotors, accompanied by a delayed start-up phase.

The analysis further highlights the superiority of the SG 6043 airfoil section in terms of power output across all wind speeds when compared to other rotors.

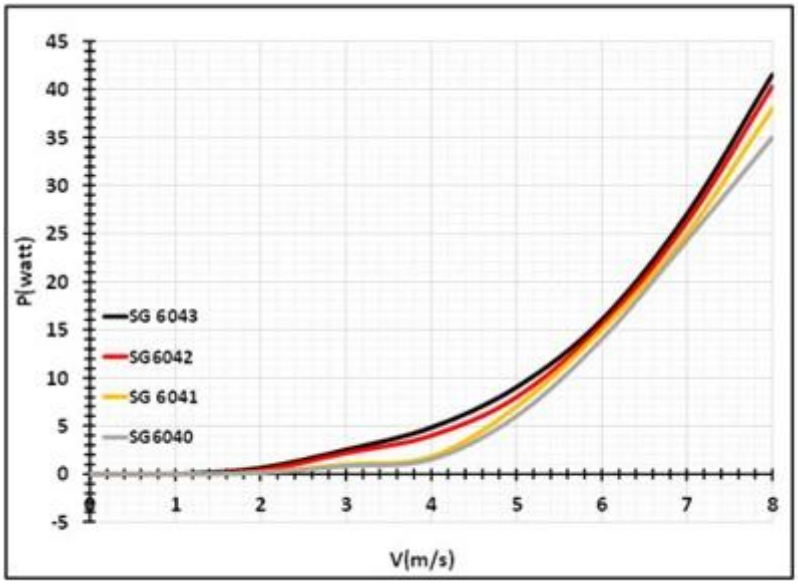
Interestingly, at a Reynolds number of 40000, the SG 6042 rotor outperforms the SG 6043 rotor within the wind speed range of 5 to 8 m/s. Despite this, the SG 6043 rotor maintains a higher starting capability. At wind speeds of 6 m/s and 8 m/s, the SG 6042 rotor shows incremental improvements of 2.5% and 4.1%, respectively, over the SG 6043 rotor.



(a)



(b)



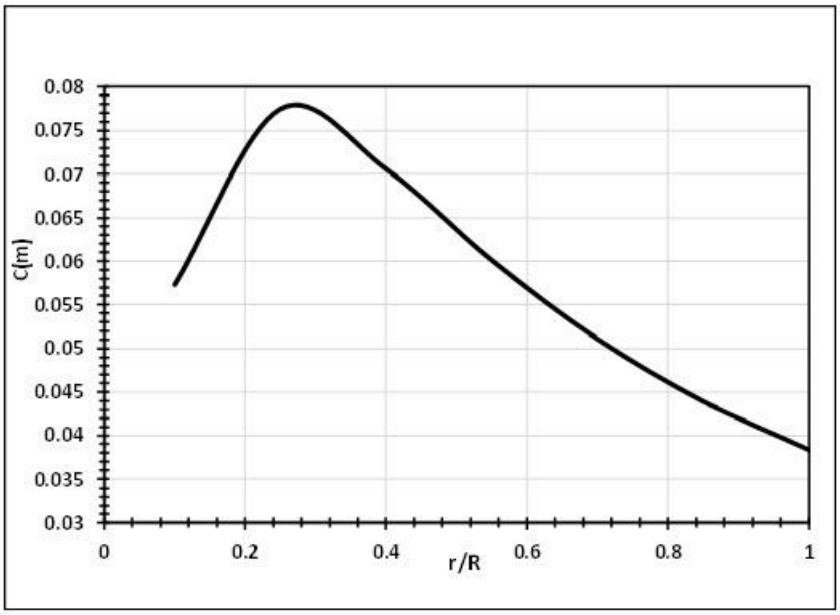
(c)

Figure IV-10: Effect Reynolds number and blade airfoil types on output power at: a) Re=20000, b) Re=40000, c) Re=55000

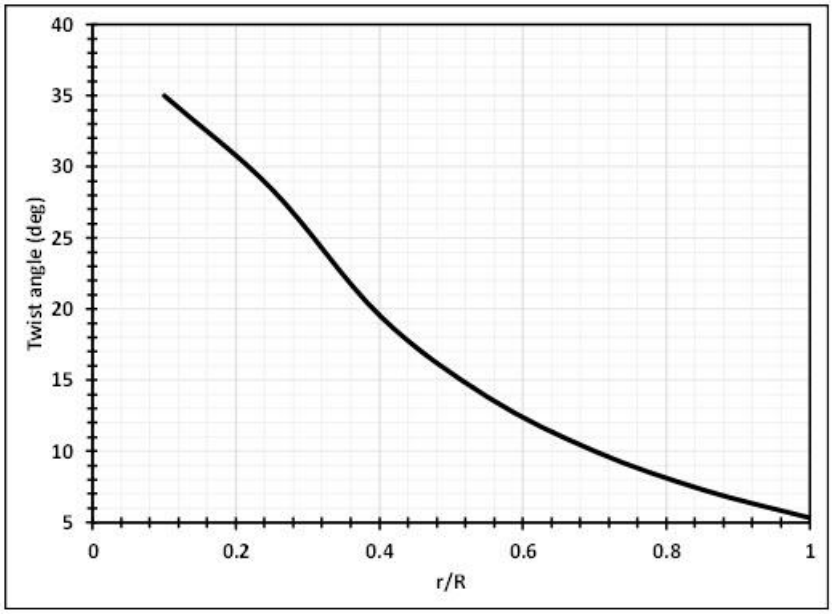
Conversely, the SG 6040 and SG 6041 rotors exhibit poor performance and significant delays in self-starting capability across all Reynolds numbers. However, these models demonstrate improved power output at the design wind speed of 6 m/s under a Reynolds number of 55000. This improvement can be attributed to the increased kinetic energy of the flow, which delays boundary layer separation. As a result, the airfoil glide ratio (CL/CD) improves, enhancing the overall performance of these rotors at this specific condition.

IV.8 BLADE GEOMETRY USING CURVE FITTING

starting from the optimal rotor geometry, figure IV-11, this part discusses the selection of mathematical functions which represent in the best way the geometric form of both chord and twist distribution. To identify the most effective functions for characterizing chord and twist distribution, the coefficient of determination R^2 and the power coefficient are adopted in this selection. In other word, the objective is to achieve accurate fit curves while minimizing the number of input parameters required [60].



(a)



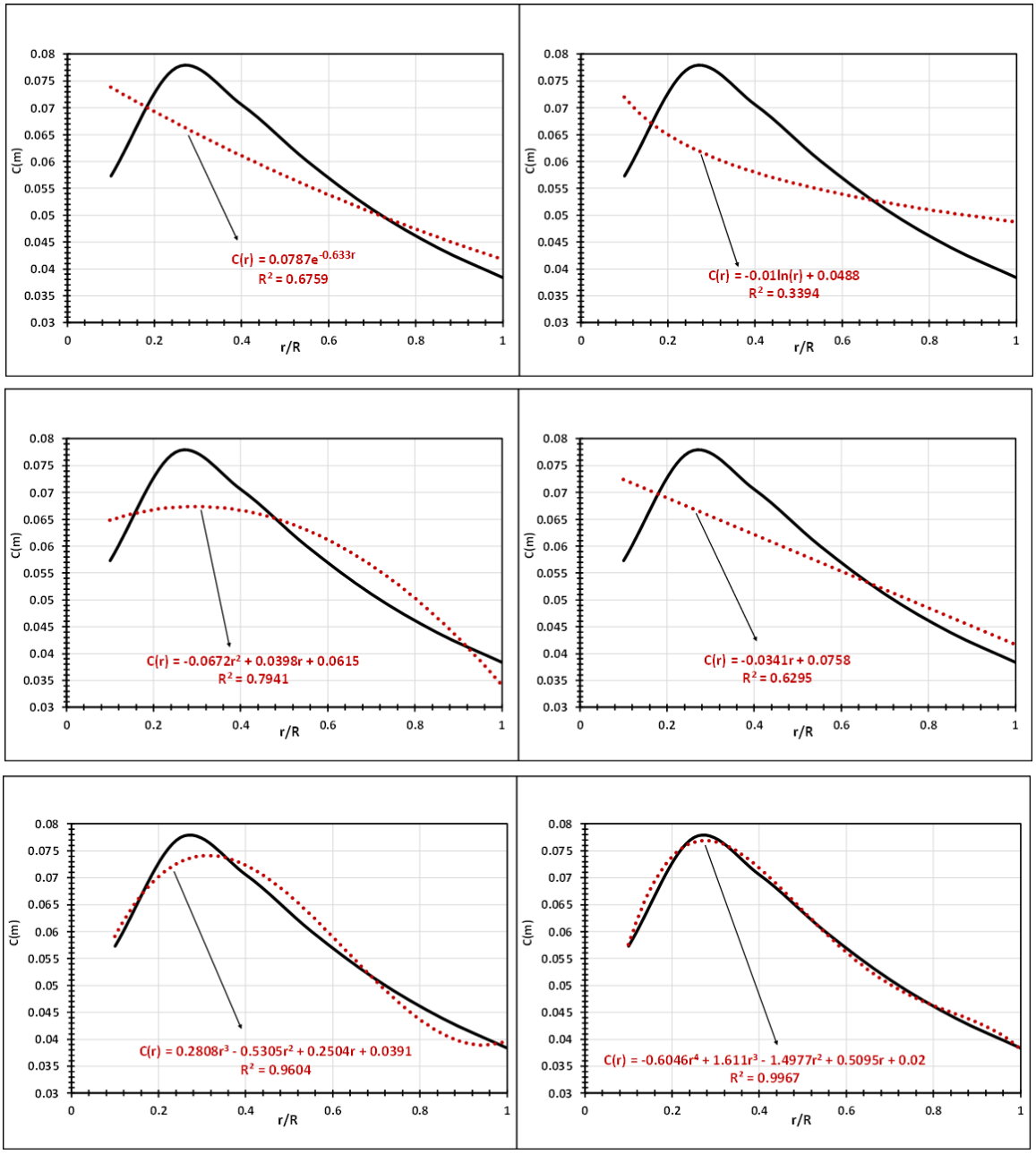
(b)

Figure IV-11: distribution of both: a) chord length, b) twist angle

IV.8.1 Chord Distribution

The chord geometric form was evaluated using eight distinct mathematical functions to identify a distribution that closely resembles the original blade design. Among all fitting curves, the polynomial representation reveals the best. Furthermore, as illustrated in Figure IV-12, an increase in the polynomial degree from four to six significantly enhances the coefficient of determination,

approaching a value of 1. This trend indicates a strong correlation with the initial chord distribution, thereby confirming the effectiveness of higher-degree polynomial functions in accurately modeling the blade geometry characteristics. Here, the four degree is selected in the polynomial representation to describe the original blade.



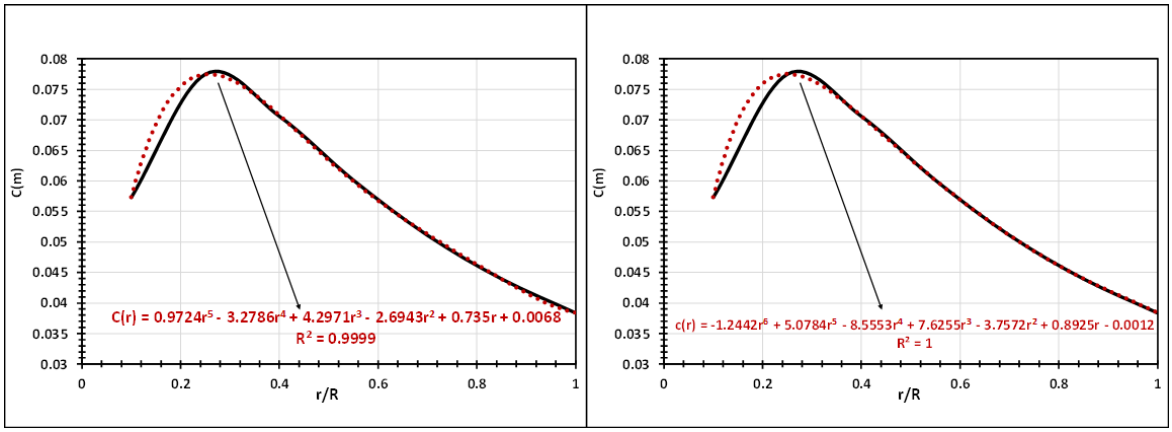
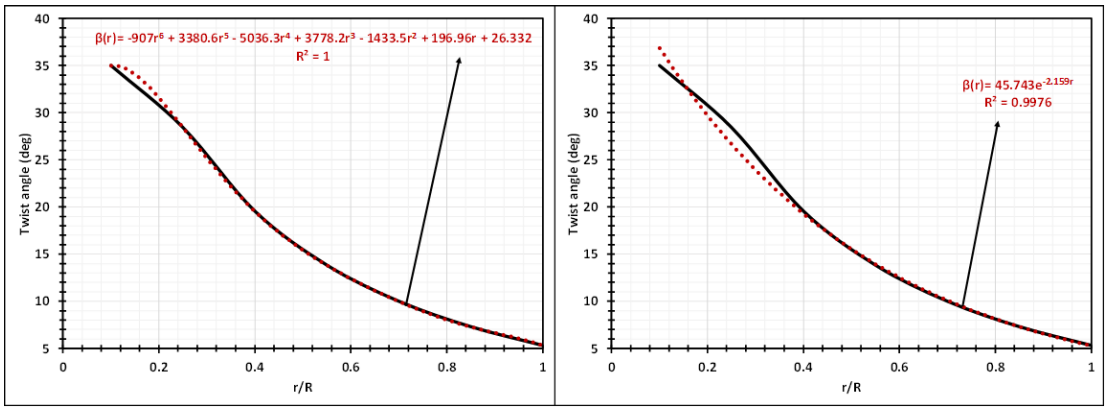


Figure IV-12: Chord length distribution with different fit curve types

IV.8.2 Twist Angle Distribution

Figure IV-13 illustrates various functions employed to characterize the alterations in the distribution of the twist angle. The analysis demonstrates that all patterns exhibit a high degree of accuracy, as indicated by the coefficient of determination (R^2), which exceeds 0.9 in all comparisons with the initial twist distribution. Consequently, the selection of a second-degree polynomial for curve fitting yields a particularly high accuracy achieving an R^2 value of 0.99 which leads to utilize three parameters.



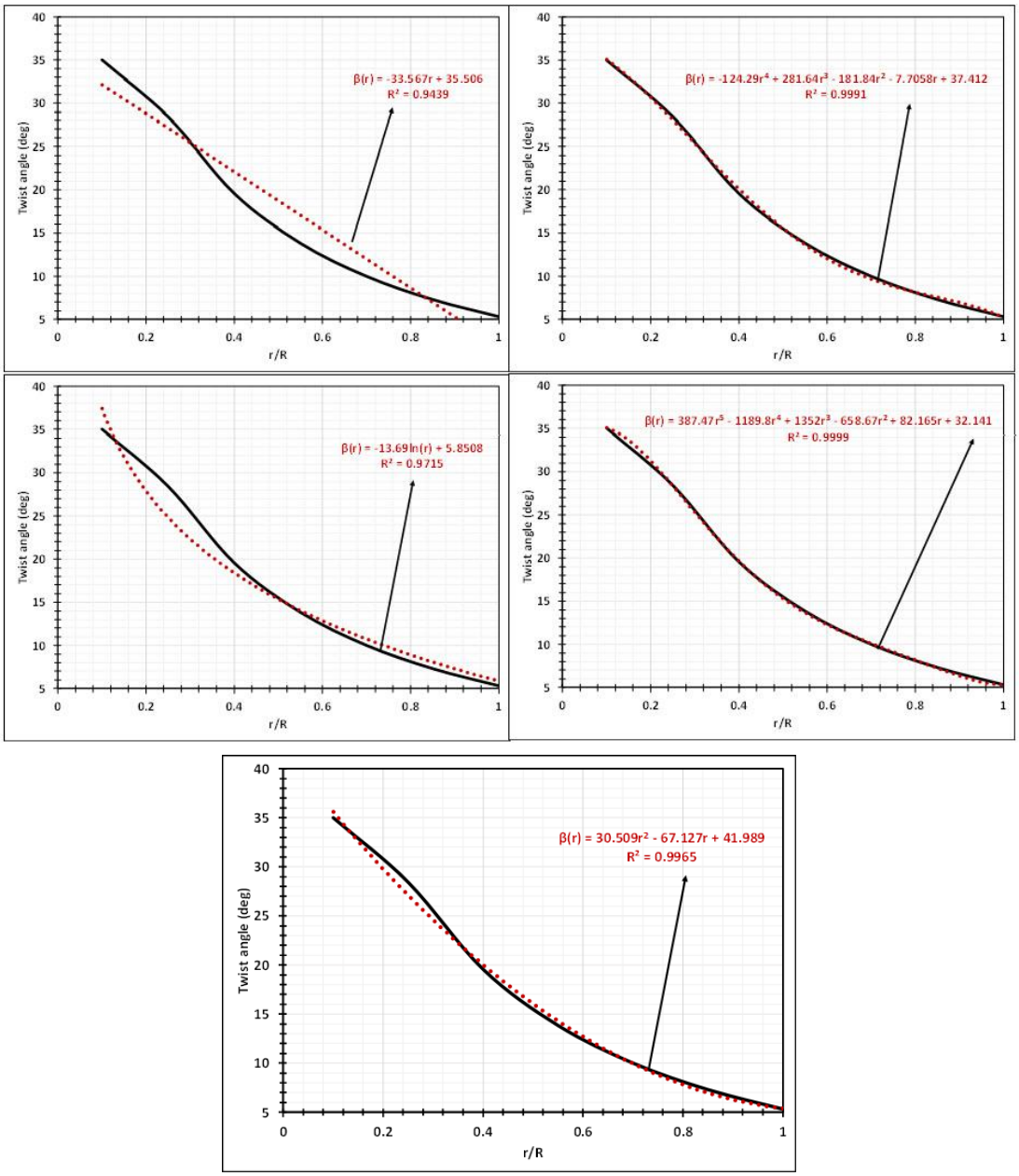


Figure IV-13: Twist Angle Distribution with different fit curve types

IV.8.3 Curves fitting modelling analysis using Qblade:

Different configurations are first built with the extracted chord distributions via specified functions and the fixed second order polynomial twist distribution and then analyzed using Qblade software, figure IV-14. It was observed that Models 6, 7, and 8 align closely with the initial model. This consistency is expected, as indicated by the increased coefficient of determination (R^2) following the application of curve fitting. Furthermore, the utilization of

polynomial functions facilitates the creation of a reliable three-dimensional representation of the rotor geometry compared with initial one. The results presented in Table IV-4 provide a comprehensive evaluation of wind turbine performance through various descriptive functions. As indicated in Table IV-4, the application of polynomial functions, specifically those of fourth degree and higher, demonstrates a significant advantage in performance assessment compared to the others model utilizing exponential and logarithmic functions. In particular, employing a fourth-degree polynomial function for the chord length distribution with a second-degree polynomial for the twist angle distribution, results in a high-performance coefficient. This approach not only enhances the reliability of the performance evaluation but also provides a more balanced representation of parameters relative to the initial configuration results.

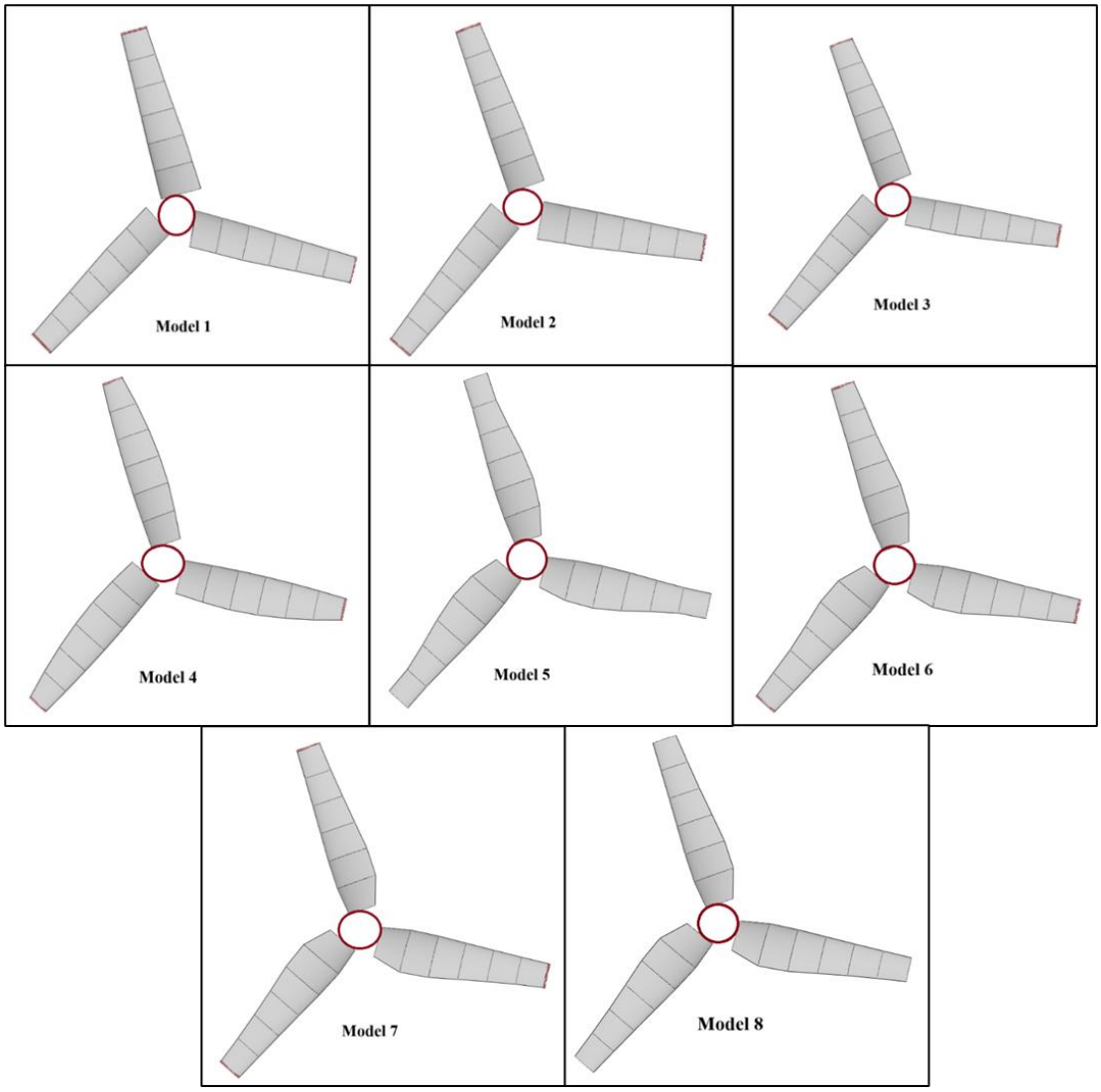


Figure IV-14: Three-Dimensional Rotor Visualization Across All Models Using Qblade"

Tableau IV-4 :Evaluation of turbine performance using various curve fitting techniques

Rotor type	Chord distribution	Twist distribution	Cp
Initial	//	//	0.407
Logarithm	$a_1 \ln(r) + b_1$	//	0.38
exponential	$a_2 e^{b_2 r}$	//	0.39
Polynomial 1est	$a_3 r + b_3$	//	0.4
Polynomial 2nd	$a_4 r^2 + a_5 r + b_4$	//	0.4
Polynomial 3rd	$a_6 r^3 + a_7 r^2 + a_8 r + b_5$	//	0.403
Polynomial 4th	$a_9 r^4 + a_{10} r^3 + a_{11} r^2 + a_{12} r + b_6$	//	0.41
Polynomial 5th	$a_{13} r^5 + a_{14} r^4 + a_{15} r^3 + a_{716} r^2 + a_{17} r + b_7$	//	0.41
Polynomial 6th	$a_{18} r^6 + a_{19} r^5 + a_{20} r^4 + a_{21} r^3 + a_{22} r^2 + a_{23} r + b_8$	//	0.41

CONCLUSION

This chapter presents a comprehensive analysis of the design of a high-efficiency rotor, emphasizing key geometric factors under varying conditions. Utilizing advanced tools within Qblade software, the study shortens calculation time while assessing the influence of geometric parameters on performance for achieve the best configuration. Additionally, the reliability of Shane's corrections for tip and root losses is validated through comparisons with experimental data and give a good agreement.

This parametric investigation facilitates a rapid design and analysis of an initial rotor compared to tedious study performed using CFD appr in-depth examination each. in fact, this later will be used in the subsequent chapter to assess the rotor performance under 3D in-depth examination.

V. Chapter V: CFD analysis and optimization of wind turbine rotor

INTRODUCTION

The present chapter performs 3D numerical investigation of HAWT wind turbine, based on the optimal configuration provided in the preceding parametric study (Ch IV). The realization of the study depends on CFD tools in investigating the performance of the initial rotor using a comprehensive flow visualization - technique. The governing equations are solved using SST K-ω turbulence model. The simulations took place within ANSYS workbench environment, which is a powerful CFD tool for specified problems. Furthermore, the methodology followed in the CFD solver leads into an optimization of the initial rotor performance, as it taken from response surface methodology (RSM) are also discussed.

V.1 NUMERICAL SOLVER

Fluent is a modern commercial computational fluid dynamics (CFD) software designed to solve both 2D and 3D flow configurations. It offers robust multigrid algorithms and provides two main numerical solver frameworks: pressure-based and density-based solvers. The pressure-based solver is typically used for low-speed, incompressible flows, while the density-based solver is optimized for high-speed, compressible cases.

In the present study, the flow through the wind turbine rotor is considered incompressible, and therefore, the pressure-based solver is employed. To enhance convergence and ensure better coupling between pressure and velocity fields, the Coupled algorithm is selected as the solution method. This algorithm solves the momentum and pressure-based continuity equations simultaneously, rather than sequentially, leading to improved stability and convergence behavior, especially in rotating flows.

The governing equations are linearized using an implicit approach, where the unknown variables at each control volume are expressed in terms of both known and neighboring unknown values. The solution is then obtained simultaneously across the entire computational domain.

V.2 SHEAR STRESS TRANSPORT (SST) $k-\omega$ MODEL

The k-ω turbulence model is classified as a two-equation model, comprising one equation for turbulent kinetic energy (k) and a second for the specific rate of turbulent dissipation (ω). Similar to the k-ε model, the k-ω framework encompasses several variations, among which the Wilcox k-ω model is particularly notable [61]. This model demonstrates enhanced numerical stability compared to the k-ε model, particularly within the viscous sublayer adjacent to the wall. However, a significant drawback of the Wilcox model is its pronounced sensitivity to the free-stream value of ω, particularly in free shear layers and boundary layers experiencing adverse pressure gradients. Consequently, the k-ω model may not be optimal for applications within the wake region of boundary layers. Conversely, the k-ε model exhibits superior performance in the outer portions and wake regions. To address these limitations, researchers have sought to integrate the advantageous features of both models. This effort culminated in the development of the Shear Stress Transport (SST) k-ω model [62]. The defining equations for the two transport mechanisms within the SST model are presented below:

$$\frac{\partial}{\partial x_j}\left[(\mu+\sigma_k\mu_t)\frac{\partial k}{\partial x_j}\right]+P_k-\beta^*\rho\omega k \qquad \textbf{(V.1)}$$

And

$$\frac{\partial}{\partial x_j}\left[(\mu+\sigma_k\mu_t)\frac{\partial k}{\partial x_j}\right]+\gamma P_k\frac{\omega}{k}-\beta\rho\omega^2+2(1-F_1)\rho\sigma_{\omega 2}\frac{1}{\omega}\frac{\partial k}{\partial x_j}\frac{\partial \omega}{\partial x_j} \qquad \textbf{(V.2)}$$

The constant β* is set to 0.09. The final term in Equation (V-2) represents cross-diffusion, active only beyond the boundary layer. The blending function F_1 facilitates the transition between the original k-ω model within the boundary layer and the modified k-ε model in free shear and free-stream regions. The constants in Equations (V-1) and (V-2) are presented in a general, compact form.

Where ϕ_1 represents the constants associated with the $k-\omega$ model (when $F_1=1$) and $\phi_2$represents the constants associated with the $k-\varepsilon$ model (when $F_1=0$).

$$\phi = F_1\phi_1-(1-F_1)\phi_2 \qquad \textbf{(V.3)}$$

Now, $\gamma\ \beta, \sigma_k$ and σ_ω defined by blending the coefficients as:

- Inner model constantsγ_1: = 0.5532,β_1=0.075,σ_{k1} =0.5,$\sigma_{\omega 1}$ =0.5
- Outer model constants: γ_2: = 0.4403,β_2=0.0828,σ_{k2} =1,$\sigma_{\omega 2}$ =0.85

The blending function $F_1$is defined by:

$$F_1 = \tanh\left\{min\left[max\left(\left(\frac{\sqrt{k}}{\beta^*\omega d}, \frac{500\nu}{\omega d^2}\right), \frac{4\rho\sigma_{\omega 2}k}{CD_{k\omega}d^2}\right)\right]\right\} \quad \textbf{(V.4)}$$

With:

$$CD_{k\omega} = \max\left(2\rho\sigma_{\omega 2}\frac{1}{\omega}\frac{\partial k}{\partial x_j}\frac{\partial \omega}{\partial x_j}, 1.0e^{-20}\right) \quad \textbf{(V.5)}$$

And d being the distance to the nearest surface.

For the $k-\omega$ model, the boundary condition on the solid wall is as follow:

$$\omega_{wall} = \frac{16\nu}{\beta_1 d^2} \quad \textbf{(V.6)}$$

$$k_{wall} = 0 \quad \textbf{(V.7)}$$

V.3 CFD ANALYSIS OF INITIAL TURBINE ROTOR

The considered model of a horizontal-axis wind turbine used in this thesis was developed based on Blade Element Momentum (BEM) theory, as detailed in Chapter III. The rotor is characterized by both tip radius and hub radius of 300 mm and 30 mm, respectively. This design incorporates three blades with design wind speed of 6 m/s. Figure V-1 illustrates the wind turbine blade profile, which was generated using Design Modeler software to perform Computational Fluid Dynamics (CFD) simulations of the turbine rotor.

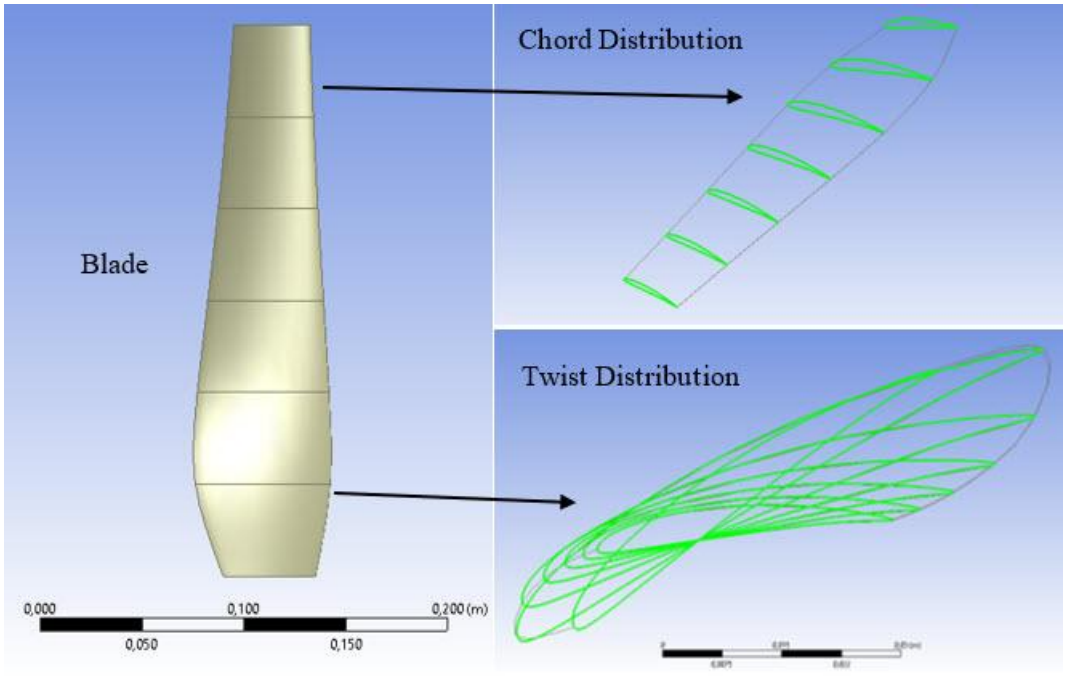


Figure V-1: 3D initial blade formed with both chord and twist distribution

V.4 DOMAIN GEOMETRY

The fluid domain under investigation is modeled as a truncated cone, featuring a small base serving as the inlet and a larger base as the outlet. To optimize computational efficiency and reduce the total number of simulation cells, one-third of the domain including a single blade is analyzed, as depicted in Figure V-2. The blade is strategically positioned within the domain, with upstream and downstream distances set at 10 and 20 times the rotor radius, respectively. The dimensions of this configuration are selected from [63] to capture accurately the relevant phenomena, particularly the wake region.

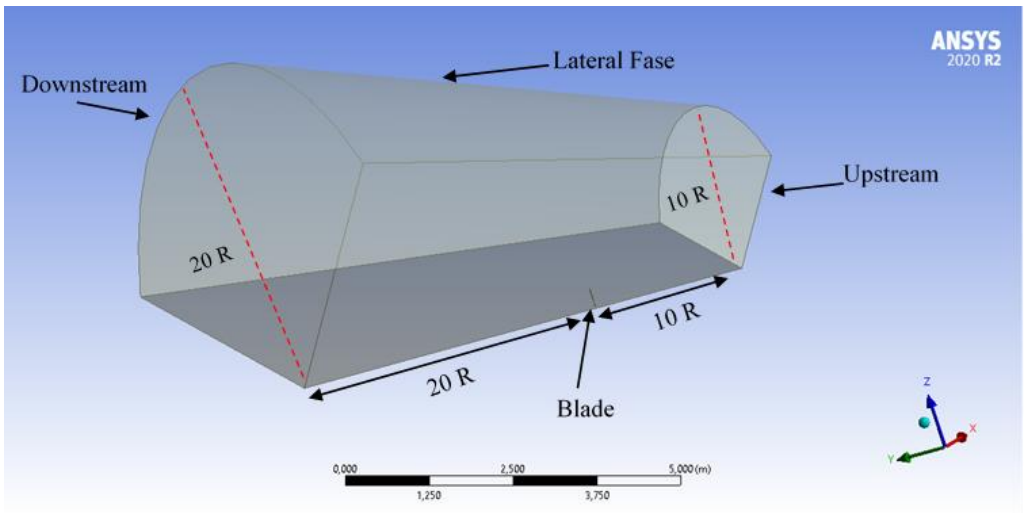


Figure V-2: Illustration of the fluid domain with blade

V.5 COMPUTATIONAL GRID

The choice of a high-resolution mesh in the region of severe gradient significantly influences the precision of computational calculations; thus, it is imperative that all factors are chosen to develop an accurate computational model. Figure V-3 illustrates the effective generation of the boundary layer grid around the blade surface, clearly depicting both the transversal and vertical sections of the blade. Furthermore, the mesh configuration is meticulously monitored at both leading and trailing edges, as these regions are critical for capturing the relevant physical phenomena.

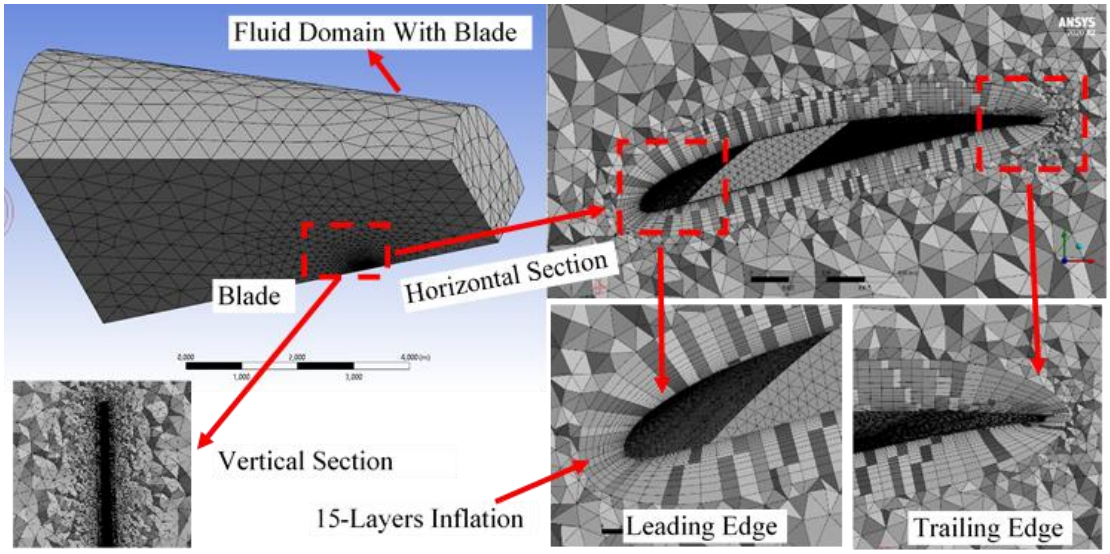


Figure V-3: discretization of the fluid domain with a fifteen -layers inflation

The geometric domain under consideration has been discretized utilizing two distinct types of meshes: polyhedral and tetrahedral, as illustrated in Figures V-3 and V-4. The polyhedral mesh is employed to enhance the accuracy and efficiency of the tetrahedral mesh [64]. To ascertain the most appropriate mesh configuration, a grid independence study was conducted. The results, presented in Table V-1, indicate that the outputs, torque and power coefficient, stabilize at constant values of 0.08 and 0.38 for a mesh with 0.86 million cells. Additionally, a 15 layers inflation region was established approximity to the blade wall, achieving a y+ value on the blade surface, less than 10 [65], calculated using an online y+ calculator with the relevant formula.

$$y+ = w\,\Delta y\,\rho\,/\,\mu$$

Where w, Δy, ρ and μ are relative velocity, the thickness of the first layer, air density and dynamic viscosity, respectively. In fact, this boundary layer zone is built using a growth rate set at 1.2 and the height of the first layer near the wall is approximately 1.41 10^{-5} m.

Tableau V-1: Mesh - Independency

Element size on the blade surface (m)	Number of cells (tetrahedral)	Number of cells (polyhedral)	Torque value (Nm.)	Performance of Turbine
0.0005	4.1 million	2.7 million	0.081	0.38
0.0008	2.8 million	1.1 million	0.08005	0.38
0.001	2.2 million	0.86 million	0.0800	0.38
0.0015	2 million	0.8 million	0.075	0.37

V.6 BOUNDARY CONDITIONS

After modelling the three-dimensional wind turbine rotor flow and its associated computational domain, it becomes imperative to establish the appropriate flow boundary conditions. The accuracy of the simulation results heavily depends on the precise definition of these boundary conditions. The model incorporates the following boundary conditions:

The boundary conditions for the domain are defined as "velocity inlet "at the small base and lateral face of the cone. The "pressure outlet" is defined at the big cone base. The no slip condition is imposed at the blade faces. Whereas the remained faces of the full domain are considered as periodic, as seen in Fig V-4. Moreover, the Moving Reference Frame Model (MRF) was employed to provide blade rotation by selecting angular velocity 60 rad/s.

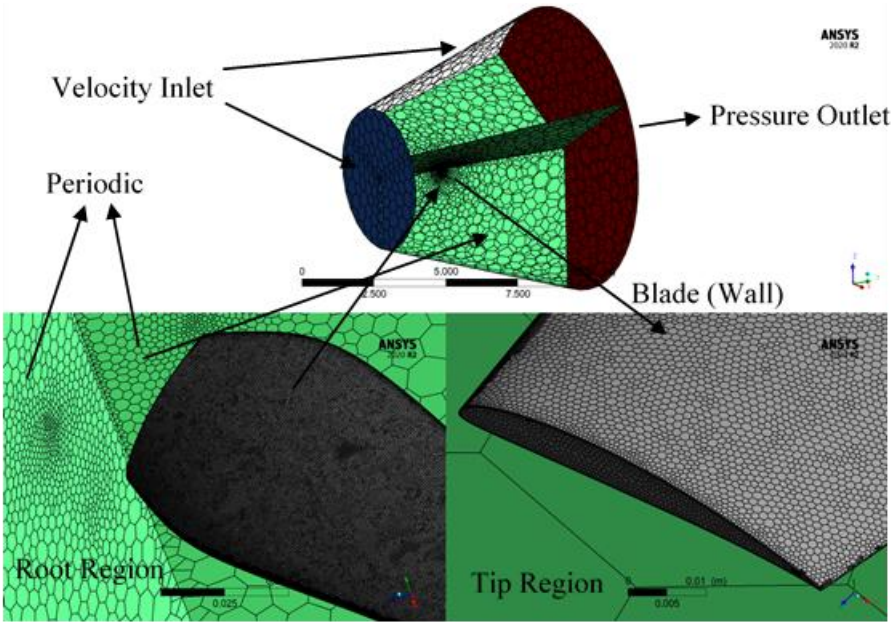


Figure V-4: discretization of the blade domain using polyhedral mesh with boundary condition

V.7 Y+ DISTRIBUTION AND NUMERICAL MODEL

After selecting the Shear-Stress Transport (SST) k-ω turbulence model for solving the Reynolds-Averaged Navier-Stokes (RANS) equations, the Y+ values on the blade surface were thoroughly analyzed to ensure the precision of the simulation results. Furthermore, a second-order upwind discretization scheme was employed for spatial discretization. Throughout the iterative solution process, convergence was monitored by tracking the residuals of the dependent variables in the governing differential equations, achieving a convergence criterion of 10^{-5}. Figure V-5 illustrates the Y+ distribution over the blade surface for the chosen

mesh. The maximum Y+ value was found to be 1.45 at the tip region, while both the leading and trailing edges of the blade consistently maintained Y+ values near 1.

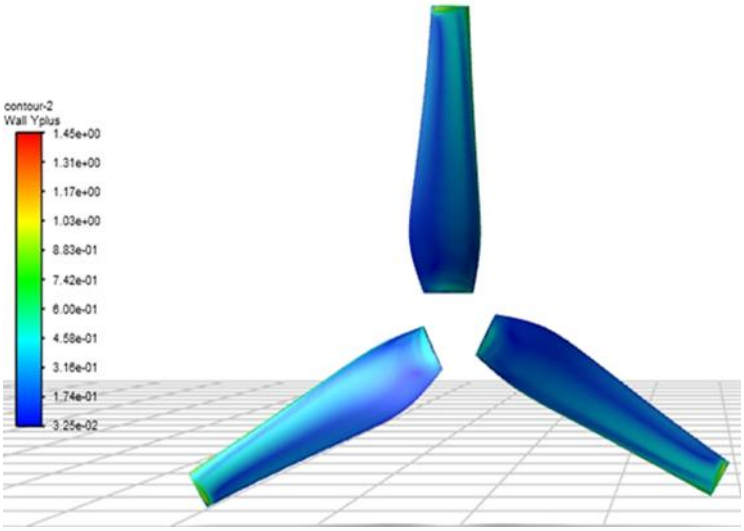


Figure V-5: y+ distribution around the blades

V.8 NUMERICAL APPROACH VALIDATION

To validate the numerical model against experimental data, the results presented in [59] are utilized. This validation involved a wind turbine rotor with a diameter of 0.7 m, designed to operate at a wind speed of 6 m/s. The rotor configuration included three blades and a hub-to-tip ratio of 10%. The aerodynamic blade geometry was defined by the NACA 4412 airfoil section, with the chord length and twist angle varying from 0.003 m and 1.7° at the blade tip to 0.068 m and 36.44° at the blade root, respectively. The rotor was tested in a low-speed wind tunnel at Ain Shams University, Egypt. For the validation, the same flow domain and mesh characteristics were maintained, with a skewness factor of less than 0.85 and the k-ω SST turbulence model. A comparison between the numerical and experimental results demonstrated good agreement, confirming the reliability of the numerical approach. As shown in Figure V-6, the peak power coefficient was predicted numerically at a tip-speed ratio (TSR) of 5, yielding a value of 0.435, which closely matches the experimental value of 0.432.

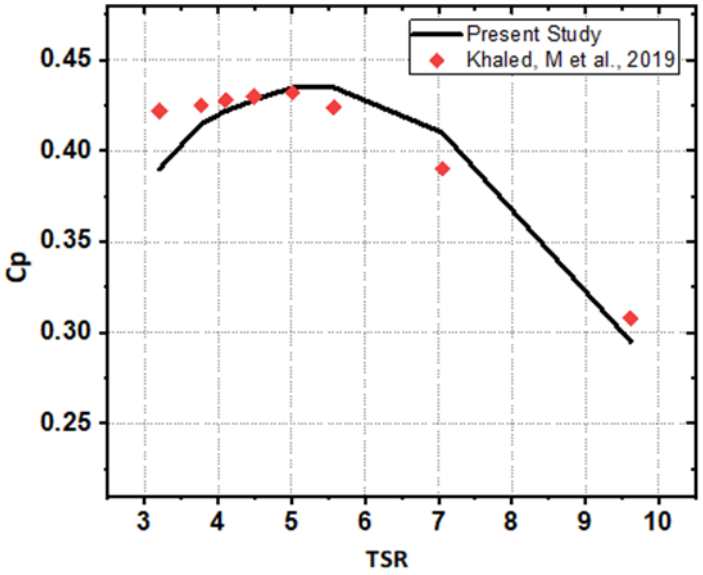


Figure V-6: Validation with the literature review at the wind speed of V=6 m/s

To assess the accuracy of the numerical results, the determination coefficient (R^2) was computed using the statistical equations outlined in [66]. This approach provides a quantitative measure of the goodness of fit between the numerical data and the reference values.

$$R^2 = 1 - \frac{\sum(\varphi_{exp} - \varphi_{pred})^2}{\sum(\varphi_{exp} - \varphi_{exp}^{avg})^2} \quad \textbf{(V.8)}$$

Where:

$$\varphi_{exp}^{avg} = (\sum_{i=1}^{n} \varphi_{exp})/n \quad \textbf{(V.9)}$$

The attainment of a correlation coefficient (R^2) of 0.85, using the same computational fluid dynamics (CFD) parameters employed in this study, demonstrates a strong agreement between the results of the two approaches. This suggests that the numerical methodology applied in the present study can be reliably utilized for subsequent simulations, ensuring high accuracy in predictive results.

V.9 NUMERICAL STUDY OF OPTIMIZED TURBINE ROTOR

In this section, the optimal rotor design is derived from initial rotor geometry, while maintaining the same model conditions; including turbulence model, mesh configuration, domain dimensions, and rotor diameter, etc.) using the goal-driven optimization methodology.

V.9.1 Goal-Driven Optimization

The process of design optimization is structured around four fundamental steps,

V.9.1.1 Geometry parametrization

After determining the optimal tip speed ratio (TSR) of 3 and a wind speed of 6 m/s, the corresponding distributions for chord length and twist angle for the initial blade design were derived. To model the variations in chord length and twist angle, a highly efficient fitting curve was applied to accurately represent the initial design parameters (see chapter IV). Consequently, the distributions of chord length and twist angle were approximated using a fourth-degree polynomial for the chord length and a parabolic distribution for the twist angle, as expressed in the following equations:

$$C(r) = a_1.r^4 + a_2.r^3 + a_3.r^2 + a_4.r + a_5 \quad \textbf{(V.10)}$$

$$\beta(r) = b_1.r^2 + b_2.r + b_3 \quad \textbf{(V.11)}$$

In this context, r denotes the radial position along the blade, while the coefficients a1, a2, a3, a4 and a5 characterize the variation in chord length as a function of radial position. Similarly, the coefficients b1, b2 and b3 describe the changes in the twist angle in the spanwise direction of the blade. Figures V-7 and V-8 illustrate the distributions of chord length and twist angle following the fitting procedure.

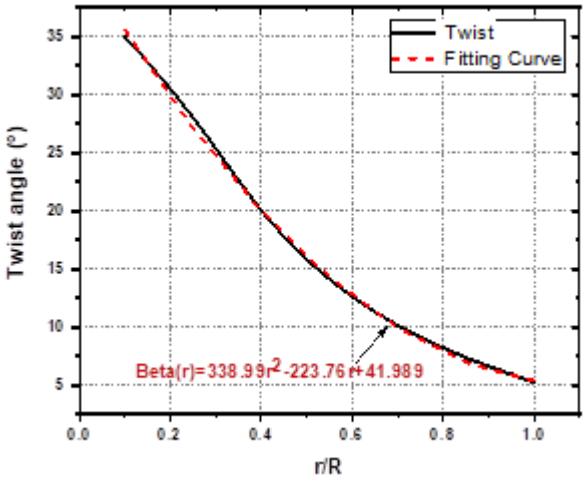


Figure V-7: Twist angle distribution with fitting curve

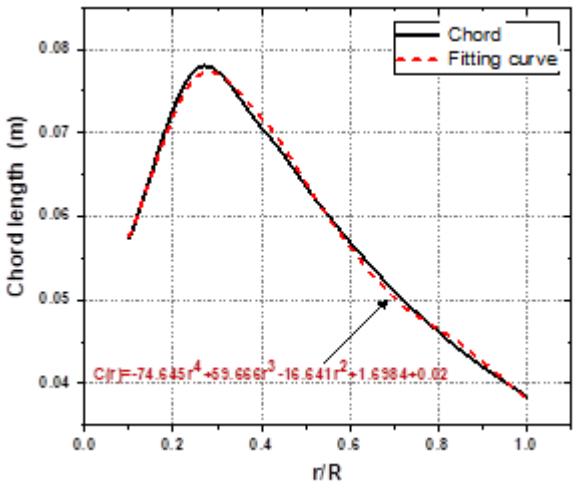


Figure V-8: Chord length distribution with fitting curve

V.9.1.2Design of Experiment (DOE)

In this step, a representative sample of input parameters (chord and twist) is systematically generated over the entire range of the input variables using a minimal number of design points. This statistic approach allows the identification of the relationship between input and output variables, ensuring that the test samples are selected with maximum efficiency. Additionally, the range of each input variable is expanded by 20% in both upper and lower bounds, as shown in Tables V-2. The primary objective of the DOE method is to strategically identify sampling locations within the design space, thereby enabling an optimal exploration of the input parameter space. This ensures that the desired response is obtained with the least number of sampling points, as described in the Design [67].

Tableau V-2: Constraints used in the optimization process

Input parameters constraints	Chord constraints (m)	Twist constraints (°)
-89.57≤a1≤-59.71	/	/
47.7≤a2≤71.6	0.03≤C1≤0.08	20≤ β1≤44
-19.97≤a3≤-13.3	0.042≤C2≤0.115	17≤ β2≤35
3.057≤a4≤1.358	0.04≤C3≤0.115	10≤ β3≤32
0.016≤a5≤0.024	0.035≤C4≤0.11	5≤ β4≤25
271.192≤b1≤406.788	0.025≤C5≤0.096	3≤ β5≤20
-265.5≤b2≤-179	0.02≤C6≤0.095	1≤ β6≤13

The creation of the test sample within the Design of Experiment (DOE) framework is performed using the Central Composite Design (CCD) scheme with four-level sampling strategy. The Central Composite Design (CCD) systematically arranges design points in relation to the central point of the design space, ensuring

a well-structured experimental setup. Often referred to as Box-Wilson Designs, CCDs are a class of multi-level fractional factorial designs that can be categorized into three primary variations: face-centred, inscribed, and circumscribed. For the purposes of this study, the face-centred CCD is the chosen approach Figure V-9. The optimization process then iteratively replicates all operations from the initial design phase, including drawing, meshing, solving the governing equations, and estimating output parameters, for each design point specified in the DOE table. This research has established a preliminary design, which includes a comprehensive chart of parameters corresponding to 38 sample points, detailing the input parameters as shown in Figure V-10.

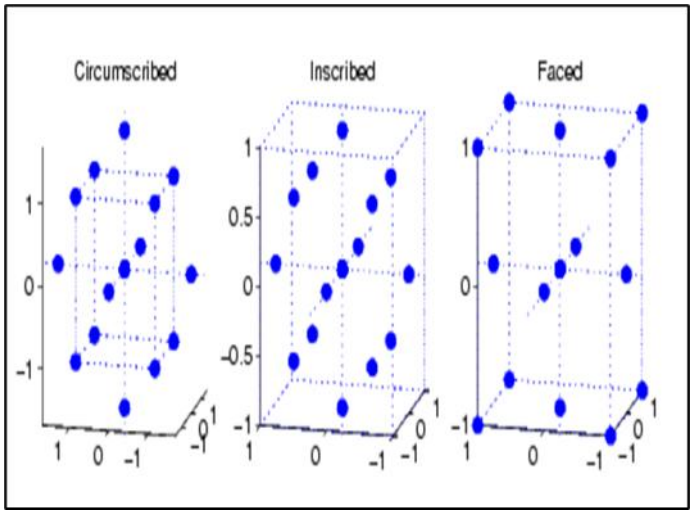


Figure V-9: The Central Composite Design (CCD) types

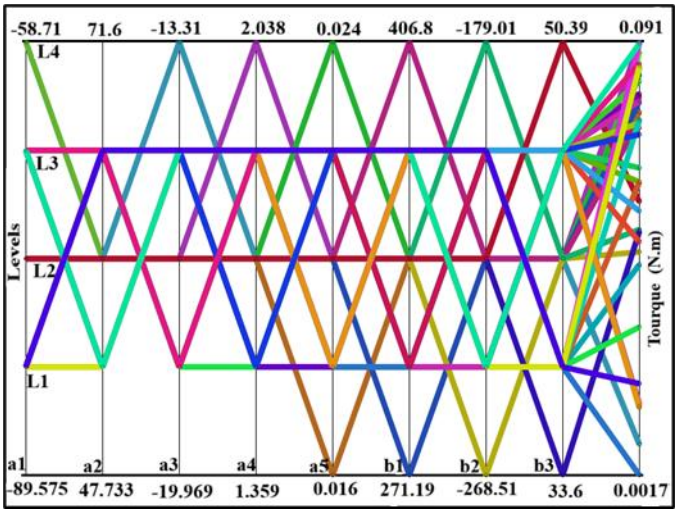


Figure V-10: The parallel diagram

V.9.1.3Response Surface

In this stage, the results derived from the DOE table are utilized to construct a multidimensional correlation model, which serves to predict the system response to variations in the input parameters. To develop the response surface, a metamodel based on non-parametric regression is employed, as outlined in the [67]. This approach enhances the model capacity to capture complex relationships between inputs and outputs, thereby improving the accuracy and reliability of the system's response predictions.

The response surface model significantly enhances the accuracy of the system output predictions, effectively capturing the nonlinear behavior of the objective functions in relation to the design parameters. To assess the quality of the response surface, a goodness-of-fit test was conducted, comparing the model predictions to the simulated values. The results demonstrated that the response surface was generated with high precision, as evidenced by the excellent fit of the design points, which correspond to a coefficient of determination (R^2) value of 0.998, as shown in Figure V-11. Furthermore, the influence of each design parameter on the objective function was analyzed using a local sensitivity chart. As depicted in Figure V-12, the effect of each input parameter on the output torque varies, with the most influential parameters being a2, a3, b2, and b3 in both the chord and twist expressions, respectively.

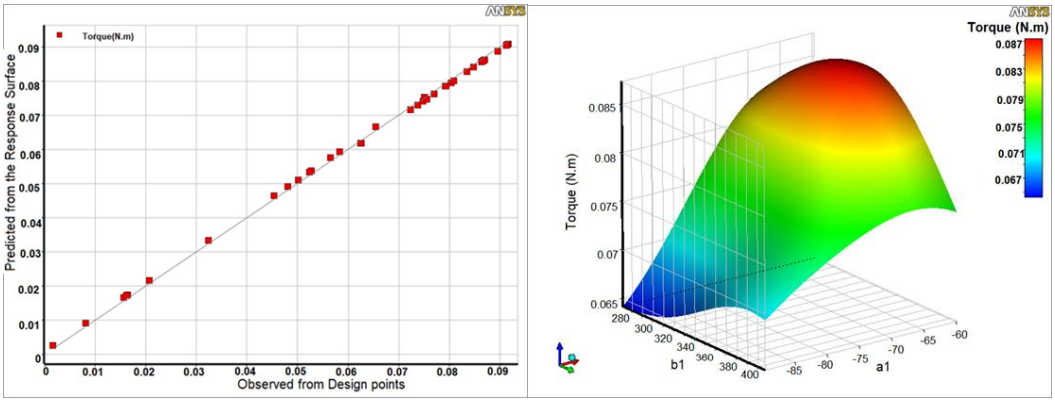


Figure V-9: goodness-of-fit of the response surface using non-parametric regression and the response surface of (a1), (b1) on the torque value.

V.9.1.3.1 Optimization

Optimization refers to the process of finding the most effective solution among a set of feasible alternatives, often by minimizing or maximizing one or more objective functions under given constraints. In complex real-world problems, multiple objectives often conflict, necessitating advanced optimization techniques.

V.9.1.3.1.1 Multi-Objective Genetic Algorithm (MOGA)

The Multi-Objective Genetic Algorithm (MOGA) is an evolutionary optimization technique designed to solve problems involving multiple conflicting objectives. It extends the traditional genetic algorithm by maintaining a population of solutions and using mechanisms such as fitness sharing, Pareto dominance, and diversity preservation to guide the search toward a set of optimal trade-offs, known as the Pareto front. MOGA is widely used in engineering, economics, and machine learning, where it is crucial to balance competing performance criteria simultaneously [68].

V.9.1.3.1.2 Wind Turbine Optimization Using MOGA

To determine the maximum torque value from the generated response surface, a new set of 8,000 data points is created through a goal-oriented optimization approach utilizing the Multi-Objective Genetic Algorithm (MOGA). From this set, the point corresponding to the highest torque is selected, which is then used to identify the optimal distributions of chord length and twist angle, based on the best-performing input parameters (as outlined in Table VI-1). The selected optimal design is subsequently validated through Computational Fluid Dynamics (CFD) analysis using ANSYS FLUENT tool. A comprehensive overview of the optimization process is presented in Figure V-11.

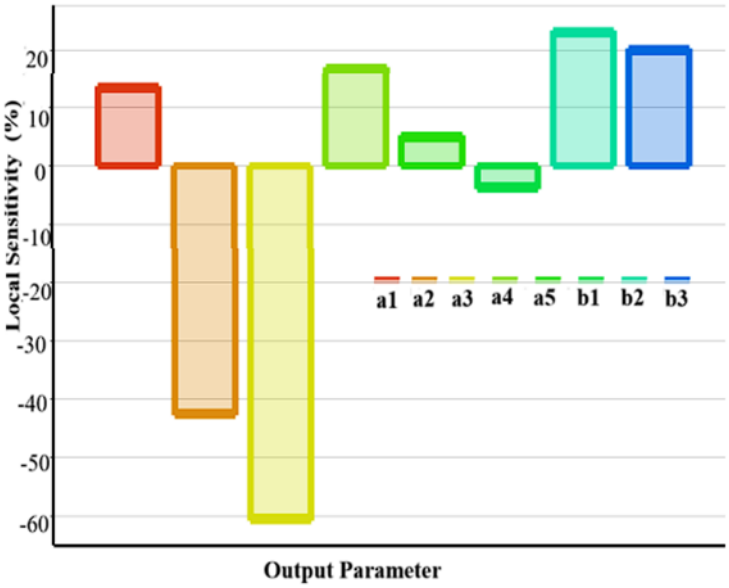


Figure V-10: Local sensitivity of the design parameters for the torque

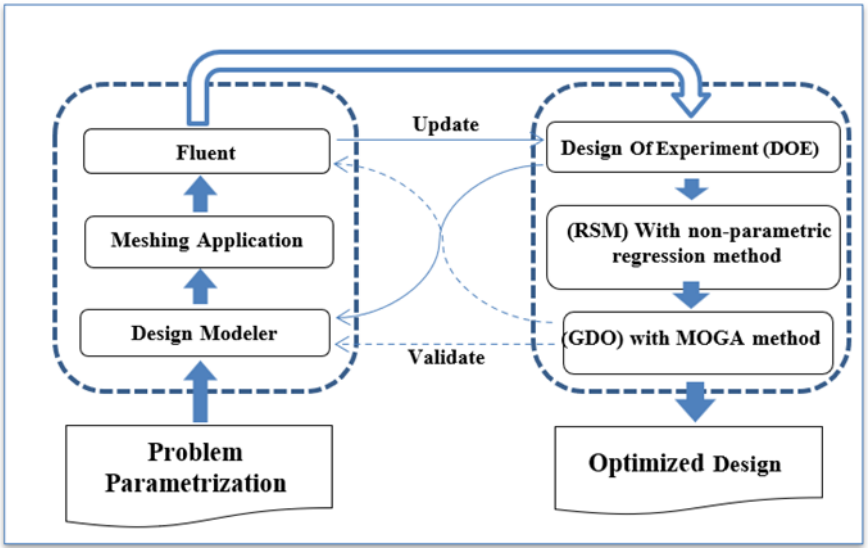


Figure V-11: Design Exploration Algorithm

CONCLUSION

This chapter presents the design and performance assessment of both the initial and optimized rotor, with an emphasis on Computational Fluid Dynamics (CFD) analysis. A polyhedral mesh is utilized for the simulations, and the resulting numerical data is compared to experimental measurements to verify the reliability and precision of the computational model. A good agreement between the numerical predictions and experimental results is observed, confirming the robustness of the approach. Furthermore, the chapter outlines the optimization strategy using NPR meta model, which employs the response surface methodology applied to the geometry of the initial rotor design.

The subsequent chapter will explore the impact of the optimization process on the initial rotor performance, offering a comprehensive analysis of the flow characteristics across the turbine rotor in both original and optimized configuration, and highlighting the improvements achieved

VI. Chapter 6 RUSALT AND DISCUSSIONS

INTRODUCTION

This chapter investigates the performance enhancement of the optimized rotor design in comparison to the initial configuration, through a comprehensive flow visualization analysis based on computational fluid dynamics (CFD). The process begins with an in-depth examination of the optimization mechanism, illustrated by an improved response surface following the optimization procedure. Key performance improvements are then highlighted, including an increase in lift production and a decrease in the area affected by separated limiting streamlines for the optimized blade relative to the initial design. Additionally, this chapter explores the extent of these improvements in terms of enhancing the turbine's starting capability. Finally, the results obtained from both QBlade simulations and CFD analyzes are compared to further validate and strengthen the reliability of the findings. Furthermore, the structural integrity of the optimized rotor during operation, compared to the initial design, can be evaluated by analyzing and comparing the contributions of the thrust coefficient and the power coefficient between two approaches.

VI.1 OPTIMIZING RESPONSE SURFACES USING THE MOGA ALGORITHM

In this section, a comparison is made between the initial and optimal response surfaces after applying the best candidate input variables, determined through the MOGA algorithm. The analysis centers on the input variables a2, a3, a4, b1, and, b2 which exhibit the most significant influence on the response, in contrast to other variables. Figure VI-1 illustrates the interactions between each of the chord distribution variables and their effects on the response. The improved surface demonstrates an 8.33% increase in the effective area performance compared to the initial surface, with a notable enhancement in the maximum performance value. However, an exception is observed in the simultaneous interaction of a2 and a4, where no performance improvement is noted despite a change in the position of the effective area.

Figure VI-2 presents the response surface maps illustrating the effect of the twist angle distribution, represented by variable b1, on the interactions between variables a3, a4, and b2. The data reveals a notable performance improvement of 20% when the twist angle is influenced by changes in the chord length. In contrast, when the twist distribution variables b1 and b2 interact, the performance increases

by 40%. Additionally, the optimized response surface effectively enhances the effective area, demonstrating high operational efficiency. These results prove the efficiency of the advanced optimization algorithms MOGA in achieving a highly efficient rotor design by leveraging precise adjustments to key variables.

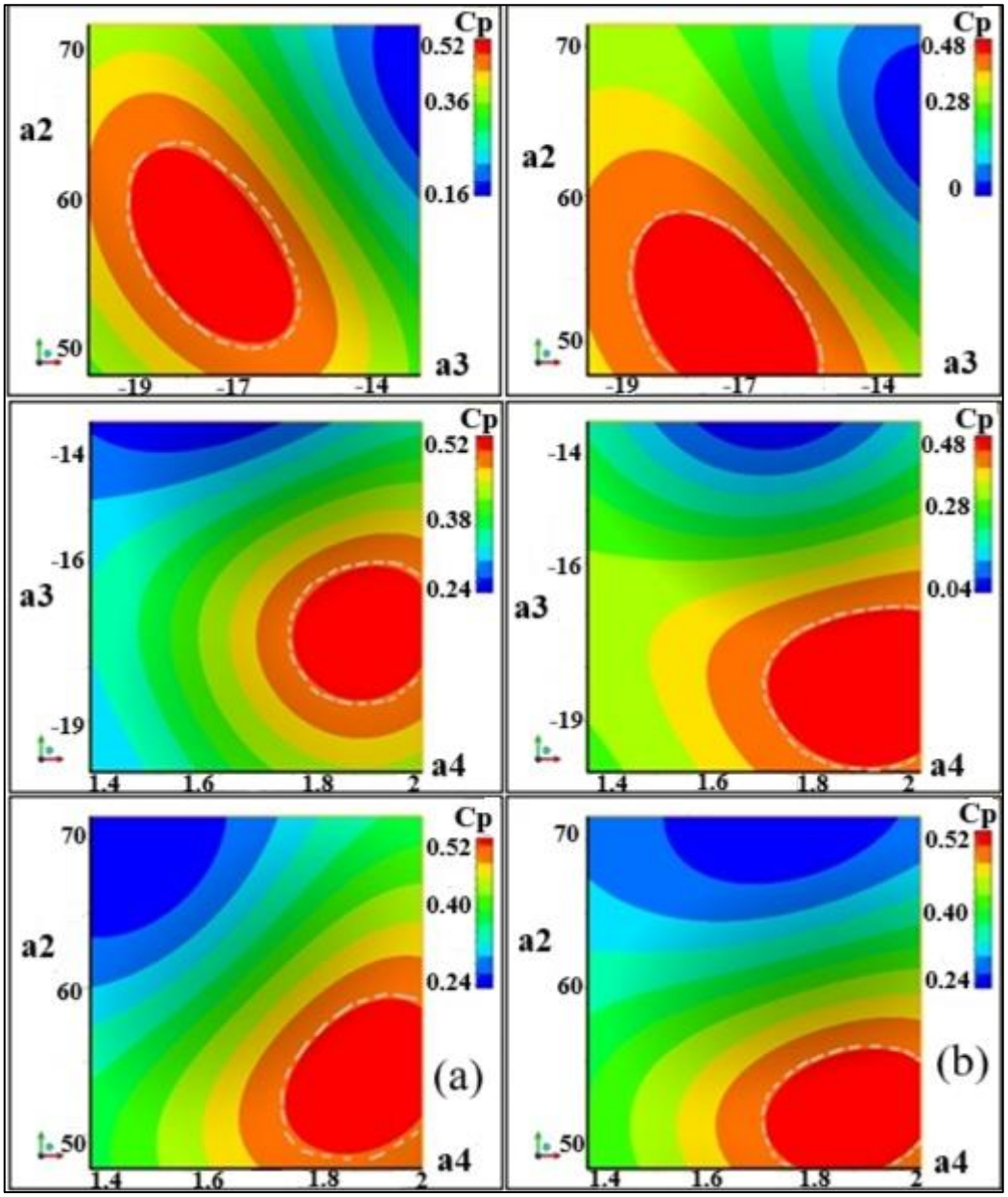


Figure VI-1: Comparison between (a) Optimal and (b) Original Response surface maps showing the interaction of chord parameters.

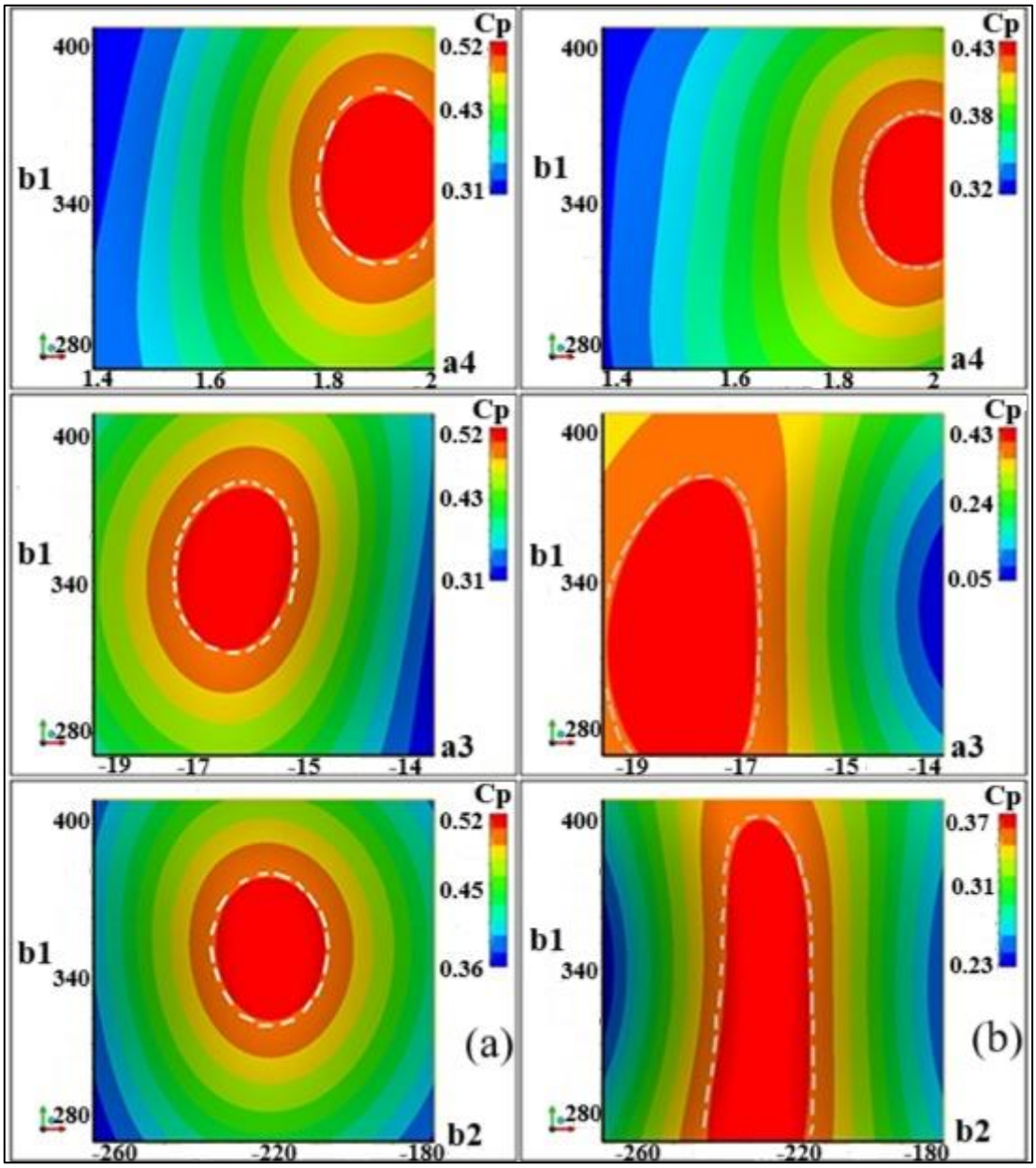


Figure VI-2: Comparison between (a) Optimal and (b) Original Response surface maps showing the interaction between chord and twist parameters.

VI.2 BLADE OPTIMIZATION TARGETS

Based on the results presented in Tables VI-1 and VI-2, the optimal chord length and twist angle for the new blade design are derived from the selected input parameters. Figures VI-3 illustrate the distribution of chord length and twist angle along the blade span, offering a comparative analysis between the optimal and initial designs of horizontal axis wind turbines (HAWTs). Qualitatively, both the initial and optimized blades exhibit similar geometries, with the chord being wider at the root and tapering toward the tip, and the twist angle maintaining a relatively

the same profile from root to tip. However, from a quantitative perspective, the optimized blade features a longer chord length compared to the initial design, while the difference in twist angle between the two configurations is minimal.

Tableau VI-1: Optimum input parameters.

Input parameters	Optimum input parameters
a_1	-65.562
a_2	54.498
a_3	-16.605
a_4	1.9704
a_5	0.0208
b_1	331.69
b_2	225.07
b_3	39.812

Tableau VI-2: Optimum distribution for both chord and twist.

Position (m)	Chord Length (m)	Twist Angle (°)
0.03	0.0663	33.35
0.075	0.096	24.79
0.12	0.098	17.57
0.165	0.090	11.7
0.21	0.079	7.17
0.255	0.0699	3.98
0.3	0.057	2.14

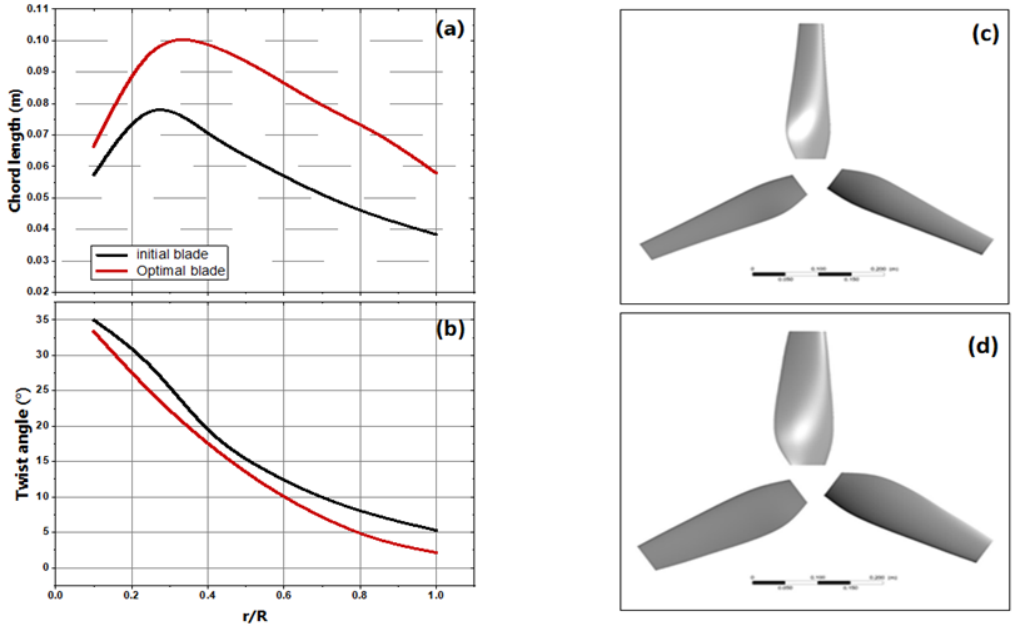


Figure VI-3: Chord and twist distributions:(a) chord length, (b) twist angle and 3D views of (c)initial and optimized rotors at TSR=3.

VI.3 PRESSURE DISTRIBUTION

In this study, the relative chord length of the initial blade is used as a baseline for evaluating the evolution of the optimized blade chord length distribution, as shown in Figure VI-4. The static pressure distribution along the blade reveals a significant increase in lift production on the optimized blade, particularly near the root region (r/R = 0.20), where the improvement is evident across the entire blade profile. Beyond 20% of the relative chord length, at stations r/R = 0.50 and r/R = 0.75, the lift enhancement is still present, although a slight reduction in lift is observed at the leading edge. At the tip region (r/R = 0.90), the increase in lift production begins approximately at 45% of the chord length. Notably, the enhanced lift on the optimized blade can be attributed to the improved pressure distribution on the suction side, which also contributes to a delay in flow separation due to the increased chord length at all stations compared to the reference blade. These findings align with the earlier analysis in Figure VI-3, where it was observed that the increase in chord length on the optimized blade results in higher lift production.

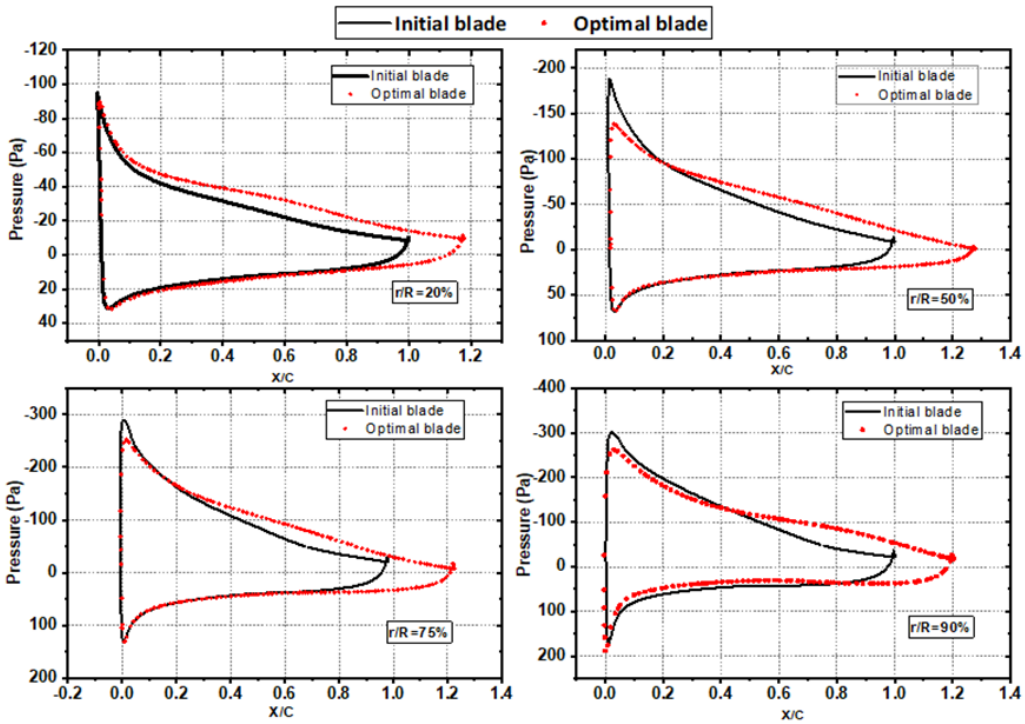


Figure VI-4: Pressure distribution comparison between the initial and optimal blade at TSR=3.

VI.4 FLOW VISUALIZATION

Figure VI- 5 presents a comparison of velocity contours and streamlines for both initial and optimized blades at different radial stations (r/R = 20%, 50%, 75%, and 90%) along the blade span, under a tip-speed ratio (TSR) of 3 and a wind speed of 6 m/s. Flow separation is observed near the trailing edge when the angle of attack approaches 10°, a configuration corresponding to the design parameters of the SG 6043 airfoil with an optimal glide ratio at a Reynolds number of 40,000, based on the maximum chord length. The aerodynamic optimization process leads to reduce boundary layer separation zone on the suction side near the trailing edge by reducing twist angle and increasing chord length. In fact, the case of the initial blade uses the SST turbulence model which overestimates the boundary layer separation at the trailing edge. To mitigate this detachment, the design angle of attack (α_D) must be reduced, thereby shifting the lift-to-drag characteristic curve (Cl/Cd vs. AoA) to the left. This adjustment corresponds to an increase in the Reynolds number through a larger chord length. Based on the velocity triangle analysis, it is evident that the design angle of attack (α_D) decreases as the chord length increases. This outcome further validates the optimization process, as the power coefficient improves with a larger chord length and a decrease in the twist angle. Additionally, it is observed that the local velocity increases from the hub to the tip region for both blades, which aligns with expected aerodynamic behavior.

Figure VI-6 illustrates the evolution of limiting streamlines and static pressure contours for both sides of the blade, highlighting the differences between the initial and optimized blade configurations, particularly in the boundary layer separation zone on the suction side. For the initial blade for TSR=2.5, the separation zone extends across almost the entire suction surface, with only a small region near the blade tip remaining unaffected. In contrast, the optimized blade shows a significant decreasing in boundary layer separation zone by approximately 75%. As the tip-speed ratio (TSR) increases from 2.5 to a value of 4, the optimized blade exhibits nearly complete flow attachment on the suction side, with a small separation area occurring at the root and trailing edge.

The boundary layer separation on the rotating blade is influenced by two primary forces. The centrifugal force, which induces a spanwise pumping effect, causes a deviation of the streamlines towards the blade tip. Conversely, Coriolis forces act in the chordwise direction, creating a favorable pressure gradient that helps delay separation. Furthermore, at all TSR values, the highest static pressure levels are observed along the leading edge of the pressure side, specifically between r = 0.15 m and r = 0.3 m. On the suction side, the lowest pressure distribution is found near the leading edge, between r = 0.2 m and r = 0.3 m. Consequently, the

pressure difference between the suction and pressure surfaces in the tip region is primarily responsible for generating the torque in the wind turbine, ultimately contributing to the majority of the power production in this area, this confirmed by the high and low levels illustrated in Figure VI-5 for the static pressure curves at different radial stations.

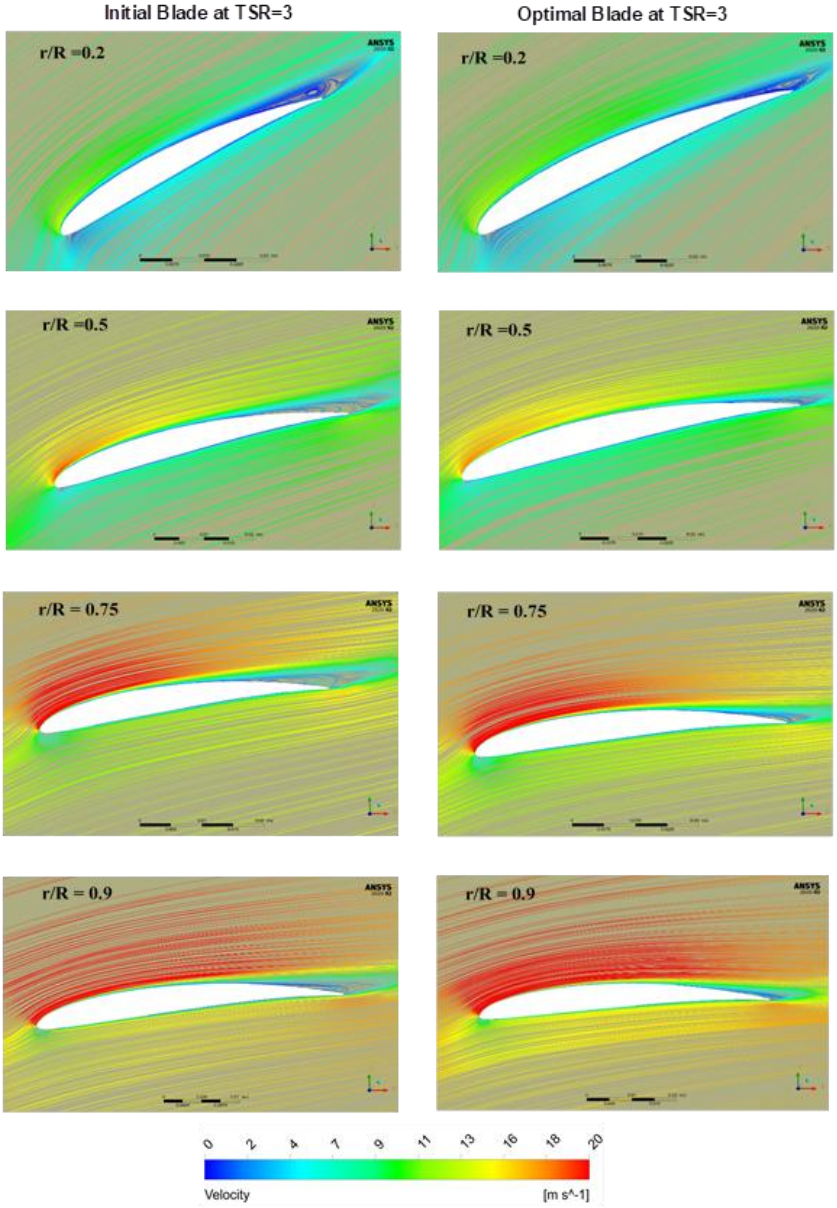
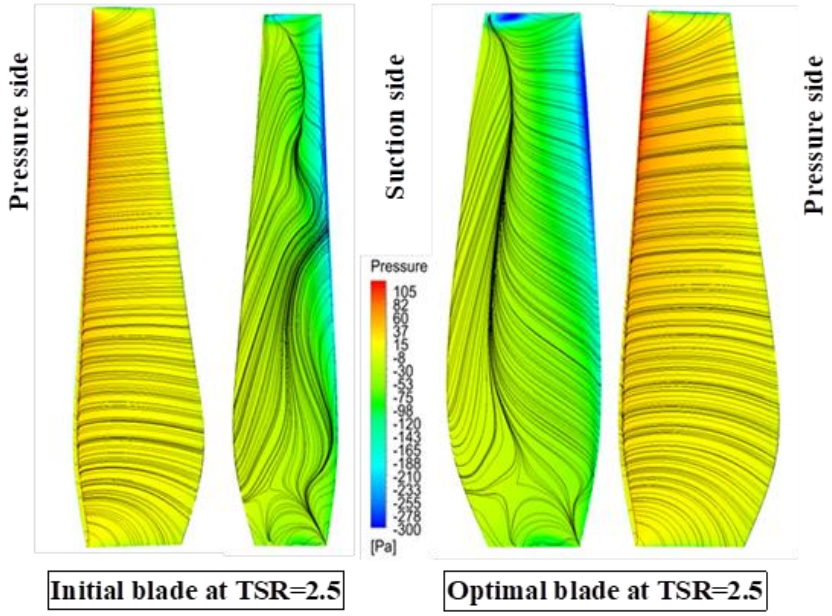
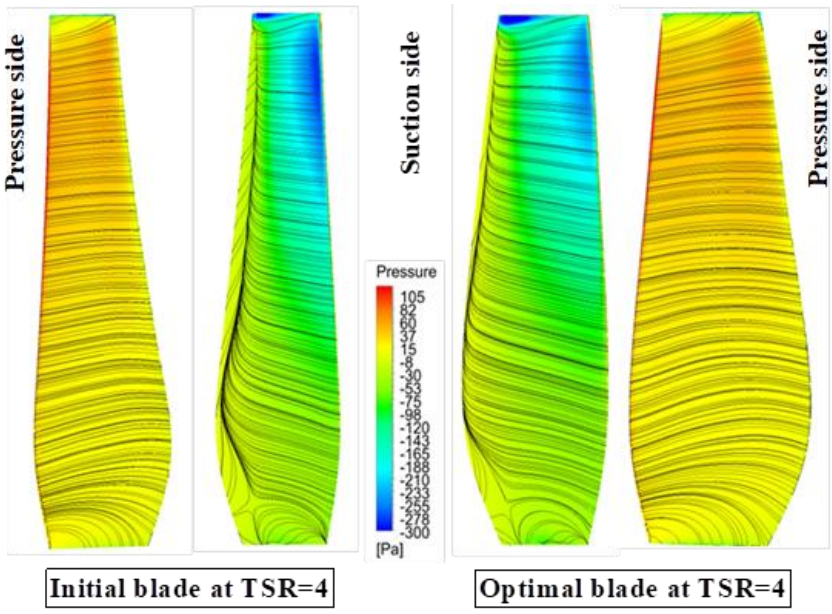


Figure VI-5: Comparison the velocity streamlines between the initial and optimal blade at design TSR.


Pressure side
Suction side
Pressure side
Pressure
105
82
60
37
15
-8
-30
-53
-75
-98
-120
-143
-165
-188
-210
-233
-255
-278
-300
[Pa]
Initial blade at TSR=2.5
Optimal blade at TSR=2.5


Pressure side
Suction side
Pressure side
Pressure
105
82
60
37
15
-8
-30
-53
-75
-98
-120
-143
-165
-188
-210
-233
-255
-278
-300
[Pa]
Initial blade at TSR=4
Optimal blade at TSR=4

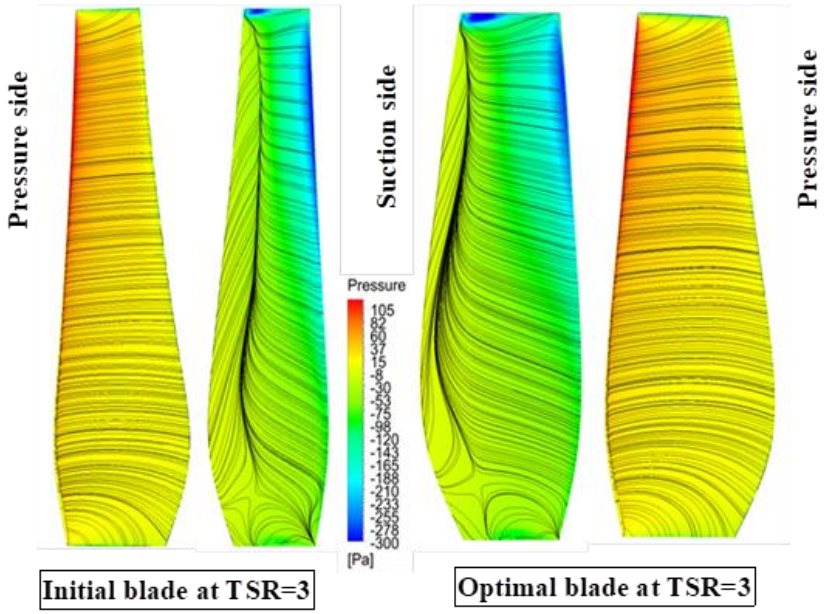


Figure VI-6: limiting streamlines with static pressure contour of optimal and initial rotor at different tip speed ratio.

VI.5 STATIC TORQUE COMPARISON

This section presents a comparative analysis of static torque, where the design with a tip speed ratio (TSR) of 3 was selected and evaluated at five different wind speeds (v = 3, 4, 5, 6, 7, and 8 m/s). The static torque for both initial and optimized rotors was analyzed using computational fluid dynamics (CFD) simulations, as illustrated in Figure VI- 7. The results demonstrate that static torque increases with rising wind speed for both rotor configurations, with higher torque values across all wind speeds with the optimized rotor. Notably, at the lowest wind speed (v = 3 m/s), the optimized rotor exhibited an increasing of 37% in static torque compared to the initial rotor. This result is indicative of an enhancement in starting ability and contributes to an optimized turbine with superior operational efficiency at lower wind speeds.

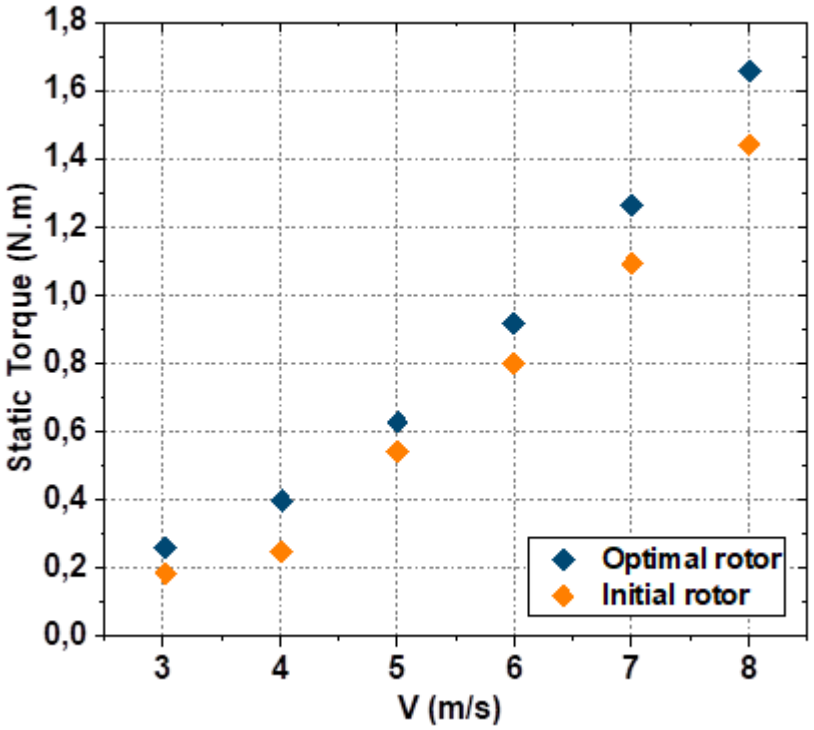
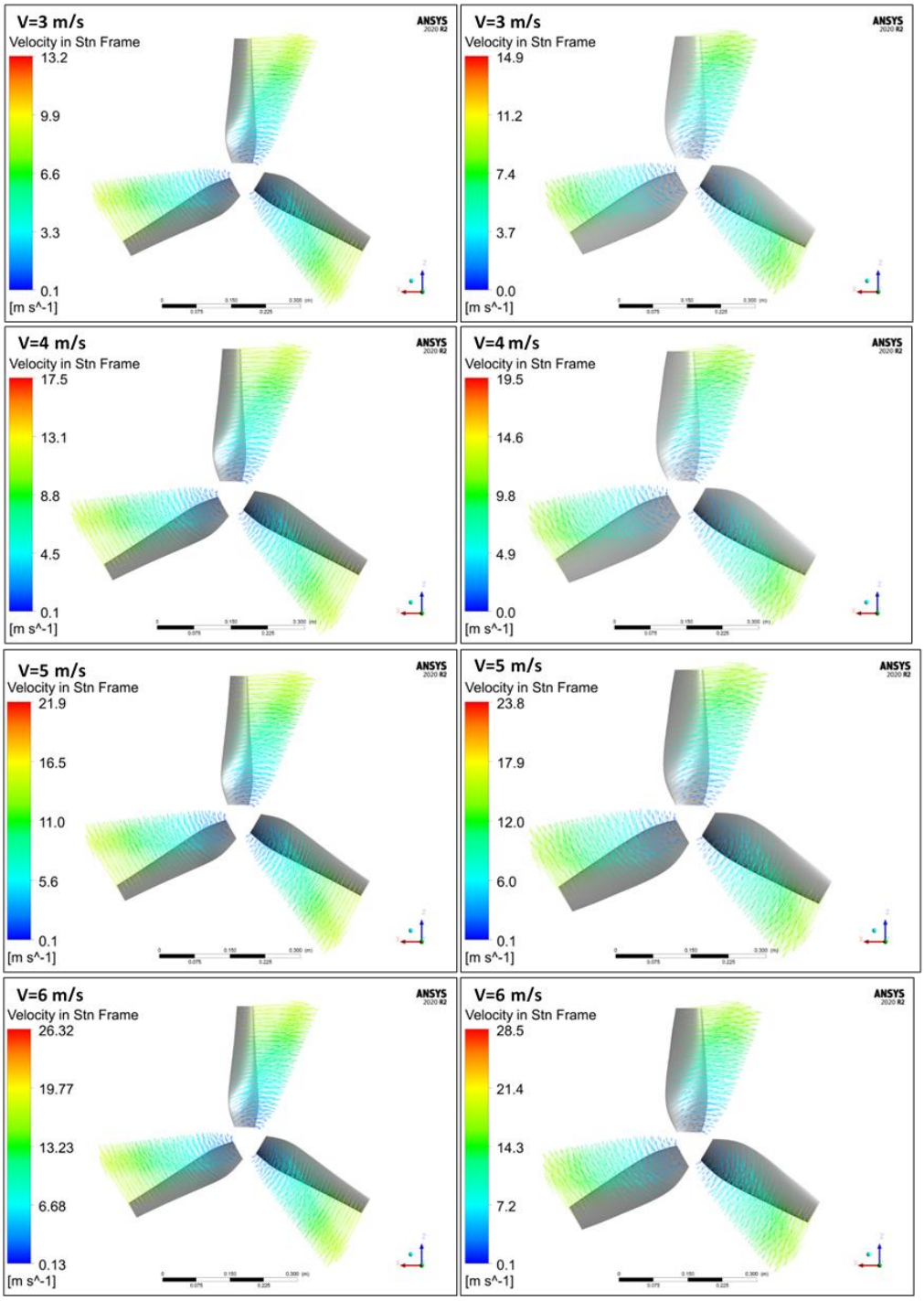


Figure VI-7: Static torque at different wind speed for both rotors.

VI.6 INFLUENCE OF THE NEW OPTIMIZED ROTOR GEOMETRY ON BLADE VELOCITY DISTRIBUTION

This section depicts the results of the local referential blade velocities in the standard frame, which vary along the blade length for both the initial and optimized rotors at wind speeds of v = 3 m/s, v = 4 m/s, v = 5 m/s, v = 6 m/s, v = 7 m/s, and v = 8 m/s. As shown in Figure VI-8, the velocity profile of the blade exhibits the same behavior with linear distribution for both initial and optimized rotors, besides an increment in velocity increasing from the root region and reaching a maximum value at the blade tip across all wind speeds.

The maximum speed of the optimal blade exhibits a significant increase compared to the initial blade for each given wind speed. Specifically, speed improvements of 12.87%, 11.42%, 8.67%, 7.46%, and 5.9% are observed at wind speeds of 3 m/s, 4 m/s, 5 m/s, 6 m/s, 7 m/s, and 8 m/s, respectively. These results not only highlight the enhanced performance of the optimized rotor relative to the initial rotor but also demonstrate a maximum increase of 12.87% in blade speed at the lowest wind speed of 3 m/s. This verifies the hypothesis presented in the previous section, suggesting that the optimized rotor exhibits improved startup capabilities compared to the initial rotor.


V=3 m/s
Velocity in Stn Frame
13.2
9.9
6.6
3.3
0.1
[m s^-1]
ANSYS
V=3 m/s
Velocity in Stn Frame
14.9
11.2
7.4
3.7
0.0
[m s^-1]
ANSYS
V=4 m/s
Velocity in Stn Frame
17.5
13.1
8.8
4.5
0.1
[m s^-1]
ANSYS
V=4 m/s
Velocity in Stn Frame
19.5
14.6
9.8
4.9
0.0
[m s^-1]
ANSYS
V=5 m/s
Velocity in Stn Frame
21.9
16.5
11.0
5.6
0.1
[m s^-1]
ANSYS
V=5 m/s
Velocity in Stn Frame
23.8
17.9
12.0
6.0
0.1
[m s^-1]
ANSYS
V=6 m/s
Velocity in Stn Frame
26.32
19.77
13.23
6.68
0.13
[m s^-1]
ANSYS
V=6 m/s
Velocity in Stn Frame
28.5
21.4
14.3
7.2
0.1
[m s^-1]
ANSYS

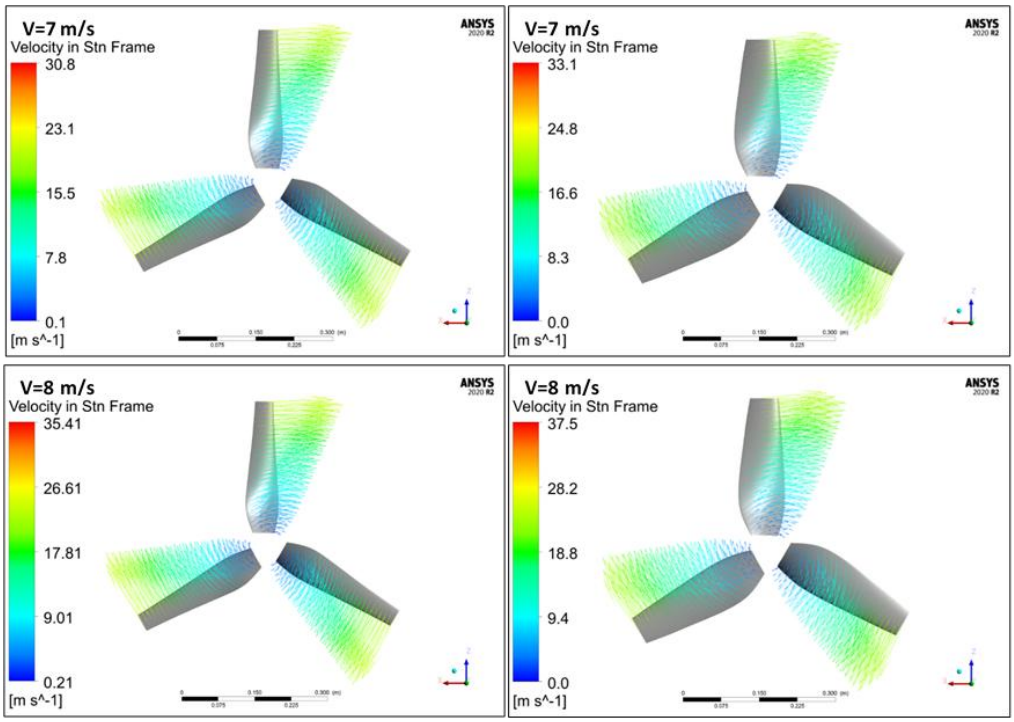


Figure VI-8: Blade velocity distribution on the initial rotor(left)and the optimized rotor(right).

VI.7 3D Flow Visualization of the Optimized Blade Design

Figure VI-9 presents the 3D streamlines at the root, middle, and tip regions of the optimized blade under design conditions, with a Tip Speed Ratio (TSR) of 3 and a wind speed of 6 m/s. The visualization aims to examine the boundary layer separation phenomena. The results clearly indicate that, despite the optimized rotor exhibiting enhanced performance and blade velocity compared to the initial design, the optimization does not entirely eliminate separation flow in particular at the root and tip regions. Specifically, while the middle section of the blade demonstrates a more stable flow attachment, both the root and tip regions experience boundary layer separation. Furthermore, the highest flow velocity is observed near the leading edge of the blade. These findings highlight the limitations of the optimization potential to control the vortex structures near the blade ends.

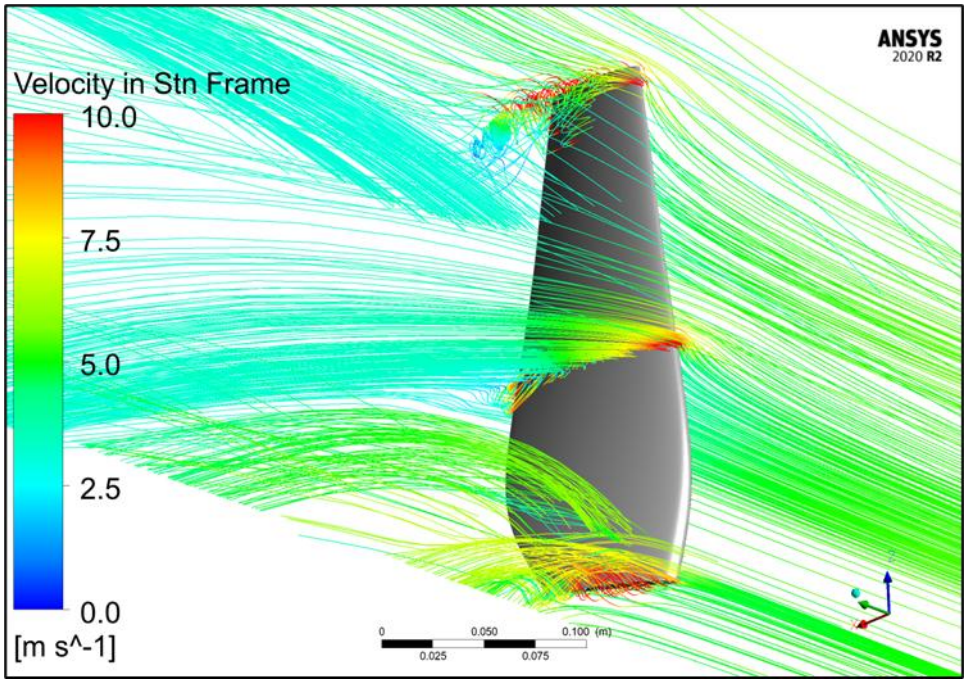


Figure VI-9: 3D flow visualization on the optimal blade at design TSR.

VI.8 COMPARISON RESULTS BETWEEN QBLADE AND CFD

VI.8.1 Introduction

This section enhances the reliability of the performance evaluation results for both the initial and optimized rotors derived from Computational Fluid Dynamics (CFD) simulations by performing a comparative analysis with the outcomes obtained from the open-source QBlade software. Specifically, torque, thrust, and power extracted by the rotors are assessed across a wind speed range of 3 to 8 m/s, which corresponds to the typical low wind speeds encountered in small wind turbine operation. In addition, a detailed comparison of the torque, thrust, and power coefficients is conducted as a function of the Tip Speed Ratio (TSR). This comprehensive evaluation provides a robust understanding of the performance characteristics of both the initial and optimized rotors, integrating the two methodological approaches employed in this study.

VI.8.2 Comparison the torque and power between CFD and Qblade

The analysis presented in Figures VI-10 clearly demonstrates that both the torque and power outputs of the optimized rotor exceed those of the initial rotor across all wind speeds. Notably, there is a strong correlation between the results obtained from both CFD simulations and QBlade, with a particularly good agreement observed in the wind speed range of 4 to 6 m/s, which encompasses the design wind speed. Moreover, the increases in torque and power are found to be directly proportional to the wind speed. Specifically, CFD results indicate a 15% increase in power at a wind speed of 8 m/s and a 4% increase at 3 m/s. Conversely, the QBlade simulations tend to overestimate both power and torque in the wind speed range of 7 to 8 m/s, with power increases of 18% at 8 m/s and 8% at 3 m/s. Additionally, both computational approaches confirm an enhanced starting performance of the improved rotor compared to the baseline rotor, further highlighting the benefits of the rotor optimization.

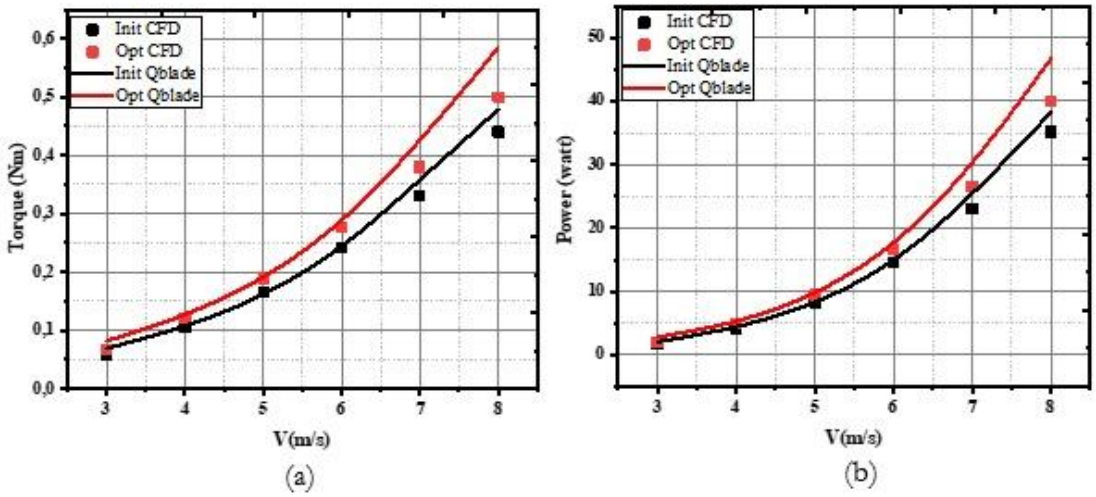


Figure VI-10: Comparison(a) the torque and(b) power between CFD and Qblade.

VI.8.3 Comparison the thrust force between CFD and Qblade

Figure VI-11 illustrates the variation of thrust force as a function of wind speed. The data reveals a high degree of consistency between the CFD and Qblade results for both the initial and optimized rotor configurations across the entire range of wind speeds, with the exception of the highest wind speed, where a minor discrepancy between the two methods is noted. Additionally, it is evident that the thrust force values for the optimized rotor consistently exceed those of the initial rotor across all wind speeds. Notably, the most significant increase in thrust force

is observed at a wind speed of 8 m/s, with a 15% increase in CFD results and a 12% increase in Qblade evaluations. Conversely, the smallest increase is recorded at a wind speed of performance 3 m/s with a 10%, where the difference between the two approaches remains minimal. These findings underscore the importance of thrust force as a key parameter in enhancing rotor performance.

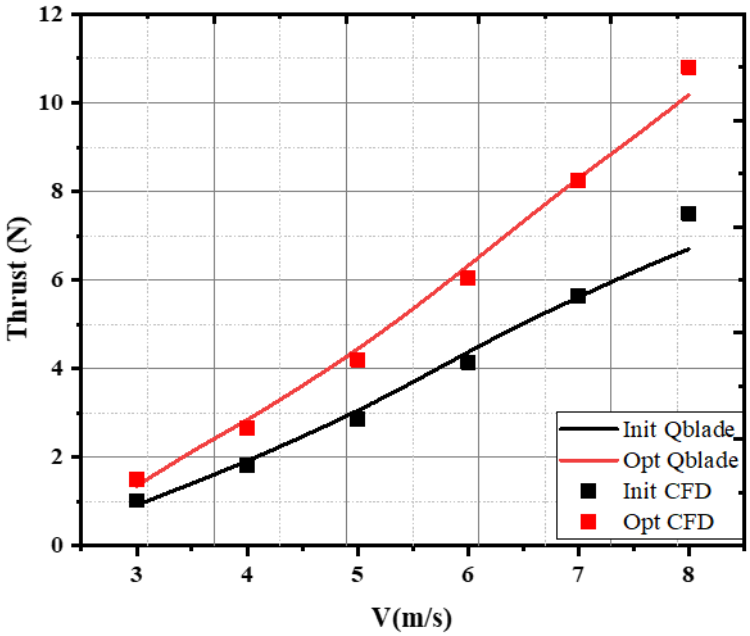


Figure VI-11: Comparison the thrust force Using CFD and Qblade Approaches.

VI.8.4 Torque coefficient compression

Figure VI-12 presents a comparative analysis of the torque coefficient for both the initial and optimized rotors at a wind velocity of 6 m/s. The data indicates that the optimized rotor significantly outperforms the initial rotor in terms of torque coefficient, as evidenced by results from both QBlade and Computational Fluid Dynamics (CFD) simulations. Furthermore, the results from QBlade and CFD show strong agreement across the entire range of tip speed ratios (TSRs) from 2.5 to 4, with the exception of TSR = 2, where a noticeable discrepancy is observed. The observed variation in torque coefficient between the two simulation methods is approximately 17.3 % for the initial rotor and 22.22 % for the optimized rotor, suggesting slight differences in the predictions of the two approaches. Additionally, the highest torque coefficients are recorded at TSR = 2.5 and TSR = 3, with values of 0.164 and 0.133 for the optimized and initial rotor, respectively.

At TSR values of 2 and 4, both the initial and optimized rotors exhibit a reduction in torque coefficient, as appeared in both QBlade and CFD results. These findings substantiate the effectiveness of the optimization method,

demonstrating an improvement in torque coefficient over the entire range generally and at the design TSR, in particular, it marked an enhancement of approximately 11.5%, as confirmed by both QBlade and CFD simulations.

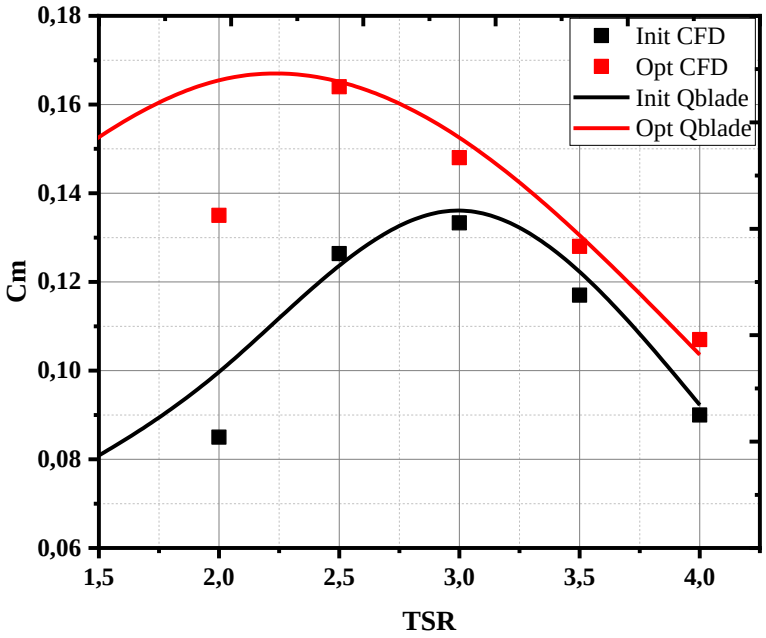


Figure VI-12: Comparison Cm between BEM and CFD.

VI.8.5 Power coefficient compression

This section provides a comparative analysis of the performance of a micro wind turbine across various tip speed ratio (TSR) values. The optimized power coefficient curves for both methods demonstrate significantly improved performance compared to the baseline configuration across the entire TSR range. Notably, the results from Computational Fluid Dynamics (CFD) and QBlade exhibit strong agreement over the operational range, particularly at TSR = 2.5. However, a notable discrepancy of approximately 20% and 15% is observed at TSR = 2 for the optimal and baseline blade configurations, respectively, which confirmed a divergence in the performance predictions between the two methods.

Table VI-3 highlights that the largest performance improvement occurs at TSR = 2, with increasing of 66.33% and 58.52% for QBlade and CFD, respectively. In contrast, the lowest performance enhancement of approximately 9.5% is recorded at TSR = 3.5 for both methods. The highest performance values are achieved at TSR = 3.5 for the CFD analysis, yielding power coefficients of 0.46 and 0.40 for the optimized and baseline rotors, respectively. For QBlade, the maximum performance is observed at TSR = 3, with power coefficients of 0.457 and 0.407 for the optimized and baseline rotors, respectively.

The decrease in rotor performance at both high and low TSR values can be attributed to boundary layer separation phenomena. At high TSR, the rotational speed increases, leading to a sharp decrease in the angle of attack and subsequent boundary layer separation on the pressure side. Conversely, low TSR values result in an increased angle of attack and boundary layer separation on the suction side. Additionally, performance reductions at TSR = 2 and TSR = 4 are primarily due to severe boundary layer separation. The superior performance of QBlade at TSR = 2, compared to CFD, can be explained by the inherent limitations of QBlade in accounting for separation and friction phenomena, as it relies on the Blade Element Momentum (BEM) theory. On the other hand, CFD, which is based on turbulent Navier-Stokes equations, incorporates these effects with greater accuracy. At TSR = 4, CFD outperforms QBlade, likely due to its capability to account for higher rotational speeds more effectively (pumping phenomena). These differences underline the unique strengths and limitations of each method in evaluating micro wind turbine performance across varying TSR values Figure VI-13.

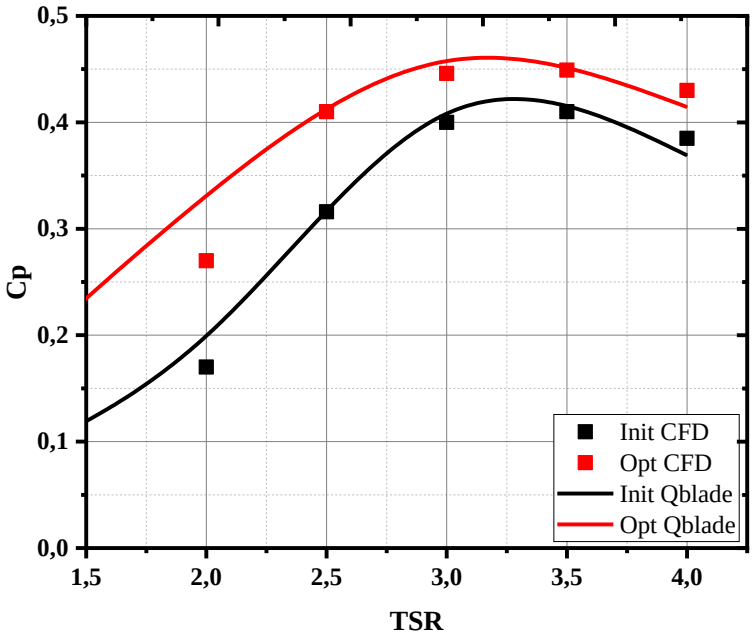


Figure VI-13: Comparison Cp between BEM and CFD.

Tableau VI-3: performance benefits of all TSR values.

Tip speed ratio	Diff Cp in CFD between initial and optimal rotor	Diff Cp in Qblade between initial and optimal rotor
2	**58.82 %**	**66.33 %**
2.5	**29.74 %**	**30 %**
3	**15 %**	**12.53 %**
3.5	**9.5 %**	**9.8 %**
4	**11.68 %**	**12.19 %**

Tableau VI-4: Comparison between CFD and Qblade results.

Tip speed ratio	Diff Cp between CFD and Qblade for initial rotor	Diff Cp between CFD and Qblade for optimal rotor
2	**14.2%**	**18.4%**
2.5	**0.5%**	**0.5%**
3	**1.7%**	**2.6%**
3.5	**1.2%**	**0.9%**
4	**4.3%**	**3.86%**

VI.8.6 Thrust force coefficient compression

In this section, the variation of the thrust coefficient (CT) with respect to the tip speed ratio (TSR) is analyzed. Figure VI-14 illustrates a strong agreement between the results obtained from CFD simulations and those from QBlade, particularly within the TSR range of 2.5 to 3.5. However, discrepancies are observed at TSR values of 2 and 4, which can be attributed to the same factors discussed in the previous section. The maximum and minimum values of the torque coefficient are observed at TSR = 4 and TSR = 2, respectively, highlighting a direct relationship between CT and the increase in rotational speed. Additionally, the structural integrity and aerodynamic performance of the redesigned blade can be further assessed by examining the percentage increase in power coefficient (Cp) in comparison to the corresponding increase in thrust coefficient (Ct). This approach provides insights into the trade-offs between performance enhancement and structural demands.

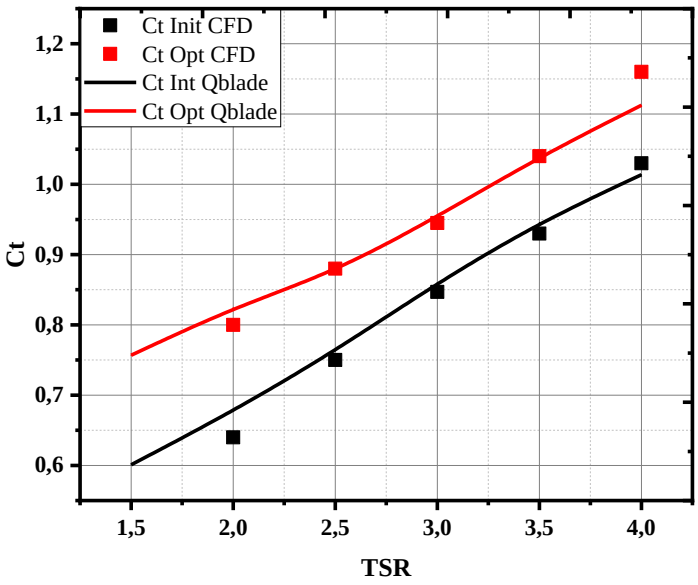


Figure VI-14: Comparison Ct between BEM and CFD.

VI.8.7 Structural Safety Analysis of the Optimized Rotor

The structural safety analysis of the optimized rotor evaluates its integrity and reliability under varying operational conditions, ensuring a balance between performance and durability. The assessment reveals two operational ranges based on the relationship between the performance coefficient (ΔCp%) and thrust coefficient (ΔCt%).

$$\Delta C_P\% = \frac{CPopt - CPinit}{CPinit} \quad \textbf{(VI.1)}$$

$$\Delta C_T\% = \frac{CTopt - CTinit}{CTinit} \quad \textbf{(VI.2)}$$

Where:

CT opt and CT init represent the optimal and initial thrust force coefficients, respectively. However, CP opt and CP init represent the optimal and initial power coefficients, respectively

In the first range (TSR = 1 to 3), ΔCp is greater than or equal to ΔCt, signifying high structural safety with notable performance gains, particularly at TSR = 2, where ΔCp increases by 60% and 50% in QBlade and CFD results, respectively. At the design TSR, ΔCp almost equals ΔCt, ensuring optimal performance and structural preservation. Beyond the design TSR, however, ΔCt surpasses ΔCp, subjecting the rotor to higher structural loads and potential damage due to increased rotational speeds. While the enhanced rotor design performs effectively over a broad range, maintaining safe operating conditions is crucial to prevent structural compromises, emphasizing the need to limit thrust force beyond design threshold, Figure VI-15.

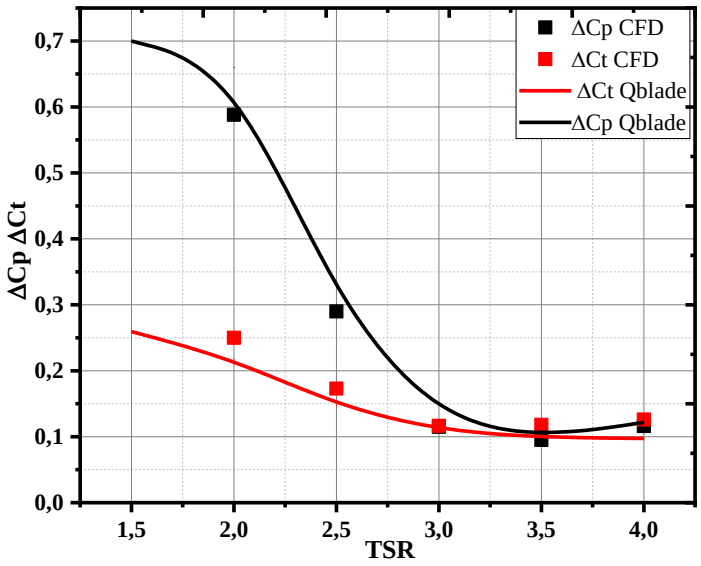


Figure VI-15: Comparison Structural Safety Analysis of the Optimized Rotor between BEM and CFD.

CONCLUSION

This section of the thesis demonstrates that using QBlade as a preliminary design tool is both practical and reliable before transitioning to detailed CFD analysis. The optimized blade achieved a 15% increase in Cp with CFD and 12.53% with QBlade at TSR = 3. The difference between the two methods remained within 1.7% for the baseline and 2.6% for the optimized rotor, confirming the consistency of results.

Relying initially on QBlade, followed by a more in-depth analysis using CFD, provides a robust and trustworthy framework for evaluating aerodynamic performance. Moreover, the integration of MOGA with a surrogate NPR model led to enhanced optimization outcomes and ensured an efficient search for high-performance solutions. This was further reinforced by the use of smooth parametric distributions for chord and twist, which contributed to a more refined and aerodynamically effective blade design

KEY RESULTS

The contributions of this research can be outlined as follows, reflecting significant advancements in aerodynamic performance, structural reliability, and optimization techniques:

- **Validation of Improved Blade Design**

Demonstrated the effectiveness of the adopted improvements, achieving a performance enhancement of 15% in CFD simulations and 12.53% in QBlade results at the design tip-speed ratio (TSR).

Showcased consistent performance gains across all TSR values, indicating broad applicability of the proposed design approach.

- **Aerodynamic Enhancements**

Achieved increased lift generation while effectively delaying boundary layer separation on the suction side of the improved blade compared to the baseline design.

- **Startup Performance Improvement**

Enhanced the starting capability of the optimized rotor, increasing static torque at a wind speed of 3 m/s by 37%.

Improved blade tip speed under identical conditions, achieving a 12.87% increase.

- **Cross-Validation and Reliability**

Increased the reliability of CFD results through comparison with QBlade outcomes, revealing strong agreement across diverse operating scenarios.

Validated the adopted optimization approach by comparing simulation data with experimental results, further strengthening confidence in the methodology.

- **Structural Integrity and Operational Range**

Verified that the improved rotor design maintains structural integrity across a wide range of operating conditions, particularly near design TSRs.

- **Optimization for Small Wind Turbines**

Highlighted the potential of the proposed optimization method for redesigning small, high-efficiency rotors based on existing prototypes.

Provided a foundation for developing experimental rotors tailored for small wind applications.

- **Implications for Future Wind Turbine Design**

Demonstrated the capability of advanced optimization techniques to enable the development of next-generation wind turbines, maximizing the utilization of wind energy resources.

These contributions underscore the significance of the research in advancing the design and optimization of wind turbine rotors, offering practical insights for improving energy efficiency and fostering innovation in renewable energy technologies.

RECOMMENDATIONS

While the results demonstrated the reliability of the optimization method employed in this research, several recommendations can be proposed to enhance the overall efficiency and performance of future studies. These recommendations are as follows:

- **Reducing Computational Time**

The use of eight input variables to represent the chord length and twist distribution significantly increases the computational time required to achieve an optimized model. This limitation also constrains the ability to explore alternative design of experiments (DOE) approaches. To address this, it is recommended to adopt more efficient parameterization techniques, such as four-parameter exponential functions, to describe the chord length and twist distribution. This adjustment is expected to reduce the computational time by approximately 50%, enabling the integration of more advanced optimization strategies, such as central composite design (CCD) with rotatable enhancement, which could further improve efficiency and design accuracy.

- **Mitigating Tip Vortex Formation**

Although the optimized blade design effectively delays flow separation along the blade compared to the initial configuration, the tip region remains prone to vortex formation. To mitigate this issue, it is recommended to integrate winglet devices at the blade tips. Winglets can help control and reduce the adverse effects of tip vortices, thereby improving aerodynamic efficiency and overall turbine performance.

- **Structural Analysis and Starting Ability Improvement**

To ensure the structural safety of the rotor under varying operational conditions, it is recommended to incorporate a balanced objective function that considers both performance gains, such as power coefficient (Cp), and thrust coefficient (Ct). This balance ensures the safe operation of the turbine across all conditions. Additionally, adopting mixed airfoil configurations along the blade span can enhance structural integrity while simultaneously improving the rotor starting capability.

By implementing these recommendations, future research can achieve higher levels of efficiency, reliability, and operational safety for optimized turbine designs.

- **Integration of Artificial Neural Networks (ANN)**

To improve the optimization efficiency of wind turbine blades, it is recommended to use Artificial Neural Networks (ANN) as a surrogate model based on input parameters defining chord length and twist distribution. A well-trained ANN can predict performance outcomes with minimal computational cost, enabling faster evaluations and supporting more advanced optimization strategies.

- **Implementation of a Refinement Strategy**

it is recommended to implement a refinement strategy, in which the optimal parameters identified by the optimizer are reintegrated into the Design of Experiments (DOE) table. This process would help create a more interactive and efficient optimization environment, leading to improved rotor performance and a more robust optimization outcome. Moreover, reinserting the refined points into the DOE would contribute to reducing the discrepancy between the Response Surface Methodology (RSM) predictions and the high-fidelity Computational Fluid Dynamics (CFD) results.

REFERENCES

[1] N. J. Sheikh, D. F. Kocaoglu, and L. Lutzenhiser, “Social and political impacts of renewable energy: Literature review,” Technol. Forecast. Soc. Change, vol. 108, pp. 102–110, Jul. 2016, doi: 10.1016/j.techfore.2016.04.022.

[2] International Energy Agency, World Energy Outlook - Executive Summary. Paris, France: IEA, 2018. [Online]. Available: https://www.iea.org/weo/weo2018/secure/. [Accessed: Feb. 5, 2025].

[3] Vaisala Inc., Vaisala Global Wind Speed Map. 2015. [Online]. Available: https://www.vaisala.com. [Accessed: Feb. 5, 2025].

[4] Y. A. Katsigiannis and G. S. Stavrakakis, “Estimation of wind energy production in various sites in Australia for different wind turbine classes: A comparative technical and economic assessment,” Renewable Energy, vol. 67, pp. 230–236, 2014. [Online]. Available: https://doi.org/10.1016/j.renene.2013.11.051

[5] Vaisala Inc., Vaisala Global Wind Speed Map. [Online]. Available: www.vaisala.com. [Accessed: Jun. 9, 2022].

[6] Wind turbine schematic [Online]. Available:

https://commons.wikimedia.org/wiki/File:Wind_turbine_schematic.svg. [Accessed: Feb. 10, 2025].

[7] D. Wood, “Small wind turbines,” in Advances in Wind Energy Conversion Technology, Berlin, Heidelberg: Springer Berlin Heidelberg, 2011, pp. 195–211.

[8] M. K. M. M. Hasanin, The Effect of Blade Geometry and Configuration on Horizontal Axis Wind Turbine Performance, M.S. thesis, Zagazig Univ., 2017.

[9] Kickstarter, Shine 2.0: Fast Charge Your Devices with Wind Power. [Online]. Available: https://www.kickstarter.com. [Accessed: Feb. 10, 2025].

[10] S. Gsånger and J. Pitteloud, World Wind Energy Report 2010. Bonn, Germany: World Wind Energy Association, 2011.

[11] Smock mill. [Online]. Available: http://en.wikipedia.org/wiki/Smock_mill. [Accessed: Feb. 10, 2025].

[12] J. F. Manwell, J. G. McGowan, and A. L. Rogers, Wind Energy Explained: Theory, Design and Application, 3rd ed. Hoboken, NJ, USA: John Wiley & Sons, 2019.

[13] H. Glauert, “Airplane propellers,” in Division L of Aerodynamic Theory, Berlin, Germany: Springer, 1976.

[14] O. Ceyhan, N. Sezer-Uzol, and I. Tuncer, “Optimization of horizontal axis wind turbines by using BEM theory and genetic algorithm,” in Proc. 5th Ankara Int. Aerospace Conf., Ankara, Turkey, 2009, pp. 17–19.

[15] B. S. Kim, W. J. Kim, S. Y. Bae, J. H. Park, and M. E. Kim, “Aerodynamic design and performance analysis of multi-MW class wind turbine blade,” J. Mech. Sci. Technol., vol. 25, pp. 1995–2001, 2011.

[16] B. S. Kim, W. J. Kim, S. L. Lee, S. Y. Bae, and Y. H. Lee, “Development and verification of a performance based optimal design software for wind turbine blades,” Renew. Energy, vol. 54, pp. 166–172, 2013.

[17] R. R. Sohail, G. S. Dulikravich, H. Sobieczky, and M. Gonzalez, “Bladelets-winglets on blades of wind turbines: A multiobjective design optimization study,” J. Solar Energy Eng., vol. 141, pp. 175–180, 2019.

[18] S. Matias, J. Feng, N. Ramos-García, and S. G. Horcas, “Design optimization of a curved wind turbine blade using neural networks and an aero-elastic vortex method under turbulent inflow,” Renew. Energy, vol. 146, pp. 1524–1535, 2020.

[19] M. Tahani and M. Moradi, “Aerodynamic investigation of a wind turbine using CFD and modified BEM methods,” J. Appl. Fluid Mech., vol. 9, no. 1, pp. 107–111, 2016.

[20] A. L. Pape and J. Lecanu, “3D Navier-Stokes computations of a stall-regulated wind turbine,” Wind Energy: An International Journal for Progress and Applications in Wind Power Conversion Technology, vol. 7, no. 4, pp. 309–324, 2004.

[21] R. Lanzafame, S. Mauro, and M. Messina, “Wind turbine CFD modeling using a correlation-based transitional model,” Renewable Energy, vol. 52, pp. 31–39, 2013.

[22] C. J. Bai, P. W. Chen, and W. C. Wang, “Aerodynamic design and analysis of a 10-kW horizontal-axis wind turbine for Tainan, Taiwan,” Clean Technologies and Environmental Policy, vol. 18, pp. 1151–1166, 2016.

[23] L. R. K. Monda, R. Gayathri, and R. M. Shanthi, “Performance exploration of mixed airfoil small scale horizontal axis wind turbine blade by QBLADE and CFD,” Int. J. Recent Technology and Engineering, vol. 8, no. 1S4, Jun. 2019.

[24] C. Casillas Farfán et al., “Novel induction blade design for horizontal axis wind turbines to improve starting phase: CFD and testing analysis,” J. Appl. Fluid Mech., vol. 15, no. 6, pp. 1635–1648, 2022.

[25] O. Polat and I. H. Tuncer, “Aerodynamic shape optimization of wind turbine blades using a parallel genetic algorithm,” Procedia Eng., vol. 61, pp. 28–31, 2013.

[26] J. Z. Wei, Z. S. Wen, and N. S. Jens, “Integrated airfoil and blade design method for large wind turbines,” Renew. Energy, vol. 70, pp. 172–183, 2014.

[27] K. R. Ram, S. P. Lal, and M. R. Ahmed, “Design and optimization of airfoils and a 20-kW wind turbine using multi-objective genetic algorithm and HARP_Opt code,” Renew. Energy, vol. 144, pp. 56–67, 2019.

[28] R. Mostafa, M. R. Ahmed, and K. Y. Maalawi, “Shape optimization of cavities embedded in airfoils for maximum lift-to-drag ratio,” Aerospace Sci. Technol., vol. 70, pp. 499–510, 2017.

[29] D. Kumar and C. E. S. Cesnik, “New optimization strategy for design of active twist rotor,” AIAA J., vol. 53, no. 2, pp. 436–448, 2015.

[30] M. K. Sekula and M. L. Wilbur, “Optimization of an active twist rotor blade planform for improved active response and forward flight performance,” J. Amer. Helicopter Soc., vol. 62, no. 3, pp. 1–12, 2017.

[31] G. E. P. Box, “Statistics as a catalyst to learning by scientific method Part II—A discussion,” J. Qual. Technol., vol. A, p. 4065, 2018.

[32] J. Y. Li, R. Li, Y. Gao, and J. Huang, “Aerodynamic optimization of wind turbine airfoils using response surface techniques,” Proc. Inst. Mech. Eng., Part A: J. Power Energy, vol. 224, no. 6, pp. 827–838, 2010.

[33] C. B. Ali, D. Michael, and P. Bjorn, “Aerodynamic optimization of airfoil profiles for small horizontal axis wind turbines,” Computation, vol. 6, p. 34, 2018.

[34] B. Huang, Y. Usui, K. Takaki, and T. Kanemoto, “Optimization of blade setting angles of a counter-rotating type horizontal-axis tidal turbine using response surface methodology and experimental validation,” Int. J. Energy Res., vol. 40, pp. 610–617, 2016.

[35] S. Tabatabaeikia, N. N. B. N. Ghazali, W. T. Chong, B. Shahizare, N. Izadyar, A. Esmaeilzadeh, and A. Fazlizan, “Computational and experimental optimization of the exhaust air energy recovery wind turbine generator,” Energy Convers. Manag., vol. 126, pp. 862–874, 2016.

[36] M. Akhlaghi, M. Asadbeigi, and F. Ghafoorian, “Novel CFD and DMST dual method parametric study and optimization of a Darrieus vertical axis wind turbine,” J. Appl. Fluid Mech., vol. 17, no. 1, pp. 205–218, 2023.

[37] S. L. Lee and S. Shin, “Wind turbine blade optimal design considering multi-parameters and response surface method,” Energies, vol. 13, no. 7, p. 1639, 2020.

[38] J. Taghinezhad, R. Alimardani, M. Masdari, and E. Mahmoodi, “Performance optimization of a dual-rotor ducted wind turbine by using response surface method,” Energy Convers. Manag.: X, vol. 12, p. 100120, 2021.

[39] A. S. Abdelhamed, Y. El-S. Yassen, and M. M. ElSakka, “Design optimization of three-dimensional geometry of wind tunnel contraction,” Ain Shams Eng. J., vol. 6, no. 1, pp. 281–288, 2015.

[40] O. F. Atac, J.-E. Yun, and T. Noh, “Aerodynamic design optimization of a micro radial compressor of a turbocharger,” Energies, vol. 11, no. 7, p. 1827, 2018.

[41] L. Zhou, Z. Wang, and J. Shi, “Optimization design of the integral inertial particle separator based on response surface method,” J. Appl. Fluid Mech., vol. 13, no. 1, pp. 133–145, 2020.

[42] M. M. Elsakka et al., “Response surface optimisation of vertical axis wind turbine at low wind speeds,” Energy Rep., vol. 8, pp. 10868–10880, 2022.

[43] Y. Yang, W. Zhao, Y. Xue, H. Yang, and C. Wu, “Improved automatic kernel construction for Gaussian process regression in small sample learning for predicting lift body aerodynamic performance,” Phys. Fluids, vol. 35, no. 6, 2023.

[44] Y. Yang, Y. Xue, W. Zhao, H. Yang, and C. Wu, “Aerodynamic shape optimization based on proper orthogonal decomposition reparameterization under small training sets,” Aerosp. Sci. Technol., vol. 147, p. 109072, 2024.

[45] Y. Yang, Y. Xue, W. Zhao, S. Yao, C. Li, and C. Wu, “Fast flow field prediction of three-dimensional hypersonic vehicles using an improved Gaussian process regression algorithm,” Phys. Fluids, vol. 36, no. 1, 2024.

[46] R. Bekkai, R. Laouar, and R. Mdouki, “Design optimization of three-dimensional geometry of a micro horizontal axis wind turbine blade using the response surface method,” PAMM, vol. e202300248, 2024.

[47] J. F. Manwell, J. G. McGowan, and A. L. Rogers, Wind Energy Explained: Theory, Design and Application. Hoboken, NJ, USA: John Wiley & Sons, 2019.

[48] P. Shin and K. Kim, “Aerodynamic performance prediction of SG6043 airfoil for a horizontal-axis small wind turbine,” in J. Phys.: Conf. Ser., vol. 1452, no. 1, IOP Publishing, 2020.

[49] T. Burton et al., Wind Energy Handbook. Hoboken, NJ, USA: John Wiley & Sons, 2011.

[50] D. M. Eggleston, Wind Turbine Engineering Design. New York, NY, USA: Van Nostrand Reinhold, 1987, p. 15.

[51] M. Drela and H. Youngren, XFOIL 6.94 User Guide, 2001.

[52] M. Hansen, Aerodynamics of Wind Turbines. Abingdon, UK: Routledge, 2015.

[53] L. A. Viterna and R. D. Corrigan, “Fixed pitch rotor performance of large horizontal axis wind turbines,” Large Horizontal-Axis Wind Turbines, 1982.

[54] W. F. Durand and H. Glauert, “Airplane propellers,” in Aerodynamic Theory: A General Review of Progress Under a Grant of the Guggenheim Fund for the Promotion of Aeronautics, 1935, pp. 169–360.

[55] W. Z. Shen et al., “Tip loss corrections for wind turbine computations,” Wind Energy: An Int. J. for Progress and Applications in Wind Power Conversion Technology, vol. 8, no. 4, pp. 457–475, 2005.

[56] H. Snel, J. Montgomerie, and A. G. N. Larsen, “Sectional prediction of 3D effects for stalled flow on rotating blades and comparison with measurements,” in Proceedings of the European Wind Energy Conference (EWEC), Lübeck, Germany, 1993, pp. 395–399.

[57] J. Hernandez and A. Crespo, “Aerodynamic calculation of the performance of horizontal axis wind turbines and comparison with experimental results,” Wind Engineering, pp. 177–187, 1987.

[58] D. Marten and J. Wendler, QBlade Guidelines, ver. 0.6, Technical University of Berlin (TU Berlin), Berlin, Germany, 2013.

[59] M. Khaled et al., “Investigation of a small horizontal-axis wind turbine performance with and without winglet,” Energy, vol. 187, p. 115921, 2019.

[60] S. Walsh and D. Diamond, “Non-linear curve fitting using Microsoft Excel Solver,” Talanta, vol. 42, no. 4, pp. 561–572, 1995.

[61] H. K. Versteeg, An Introduction to Computational Fluid Dynamics: The Finite Volume Method, 2nd ed. New Delhi, India: Pearson Education India, 2007.

[62] F. R. Menter, M. Kunz, and R. Langtry, “Ten years of industrial experience with the SST turbulence model,” in Turbulence, Heat and Mass Transfer 4, K. Hanjalić, Y. Nagano, and M. Tummers, Eds. New York, NY, USA: Begell House, 2003.

[63] M. M. Hasan, A. El-Shahat, and M. Rahman, “Performance investigation of three combined airfoils bladed small scale horizontal axis wind turbine by BEM and CFD analysis,” J. Power Energy Eng., vol. 5, no. 5, pp. 1–13, 2017.

[64] S. Mauro, R. Lanzafame, and M. Messina, “An insight into the rotational augmentation on HAWTs by means of CFD simulations—Part II: Post-processing and force analysis,” Int. J. Appl. Eng. Res., vol. 12, no. 21, pp. 10505–10529, 2017.

[65] E. Koç, O. Gunel, and T. Yavuz, “Mini-scaled horizontal axis wind turbine analysis by QBlade and CFD,” Int. J. Energy Appl. Technol., vol. 3, no. 2, pp. 87–92, 2016.

[66] J. Maindonald and W. J. Braun, Data Analysis and Graphics Using R: An Example-Based Approach, vol. 10. Cambridge, U.K.: Cambridge Univ. Press, 2010.

[67] ANSYS Inc., ANSYS DesignXplorer User’s Guide. Canonsburg, PA, USA: ANSYS Inc., 2011.

[68] W. Abdou, C. Bloch, D. Charlet, and F. Spies, “Multi-Pareto-Ranking Evolutionary Algorithm,” in Proc. 12th European Conf. on Evolutionary Computation in Combinatorial Optimization (EvoCOP 2012), Spain, Jan. 2012, pp. 194–205. [Online]. Available: